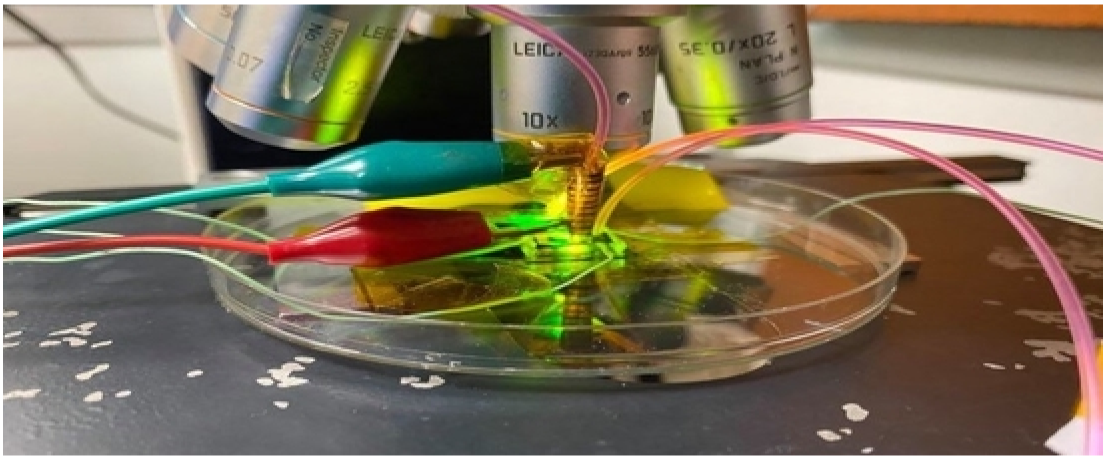

Noninvasive evaluation of heat transfer mechanisms in microfluidic channels using Light Induced Fluorescence

Miguel Filipe Azevedo Figueira

Thesis to obtain the Master of Science Degree in

Mechanical Engineering

Supervisors: Prof. Vânia Cristina Henriques Silvério

Prof. Viriato Sérgio de Almeida Semião

Examination Committee

Chairperson: Prof. Carlos Frederico Neves Bettencourt da Silva

Supervisor: Prof. Vânia Cristina Henriques Silvério

Member of the Committee: Prof. Ana Sofia Oliveira Henriques Moita

October 2020

Acknowledgments

I would like to thank to my supervisors Vania Silverio and Prof. Dr. Viriato Semião for teaching me about microfabrication and heat flow in microchannels. Their constant support, motivation and suggestions allowed me to acquire knowledge in a new technology.

I would like to thank to all my INESC-MN colleagues for all the collaboration during this time especially to Cristiana Domingues and Martim Costa, which I spent the most time with. Their friendship and advice made the time in the lab more pleasant and amusing. I would also like to thank to INESC-MN for the space and materials availability to manufacture and perform the experiments.

Finally a special acknowledgment goes to my girlfriend and to my father for all the moral support given in the most demanding times, helping me to stay focused on the work allowing me to finish my degree.

I wish to acknowledge the Fundação para a Ciência e a Tecnologia for funding of the Research Unit INESC MN (UID/05367/2020) through plurianual BASE and PROGRAMATICO financing and National Infrastructure Roadmap Micro NanoFab@PT-Norte-01-0145-FEDER-22090. This project has received funding from the National funds through FCT under the program grant PTDC-FIS-PLA/31055/2017

Abstract

Microfluidics revolutionized the world with the ability to perform several operations, on a single chip with fluidic passage sizes in the micrometer range. Depending on the purpose and application of the device, different microchannel designs are implemented with the systems often being integrated with other detection technologies. This results in quick analyses and effective results while sampling very small amounts of fluids and reagents.

In this work the impact of confluence angle, which is the angle between two inlets and one outlet, and volumetric flow rate on temperature profiles inside microchannels was addressed. Light induced fluorescence (LIF), using Rhodamine (RhB) fluorescent dye solution, was applied to obtain the temperature of the flow. A micro heater was micro fabricated for this purpose, depositing aluminium in a glass substrate and patterning it to reach the desired design. Direct write laser (DWL) was used to create the hardmask, photolithography for the SU-8 mold and soft lithography for the polydimethylsiloxane (PDMS) microfluidic device, which was irreversibly sealed against a membrane of the same material using oxygen plasma treatment. The resulting structures had two inlets with different confluence angles ($30°$,$60°$,$90°$,$135°$) and one outlet. A mass vs heat transfer analysis was conducted for the $90°$ shaped microchannel. The different configurations of microchannels (different confluence angles) were tested for a fixed hot inlet volumetric flow rate of $Q_{hot} = 50\mu L/min$, and a variable cold inlet one of $Q_{cold} = 25, 50, 75\mu L/min$.

Results showed that for the $90°$ microchannel, heat diffusion is stronger than mass diffusion. Moreover, an increase in confluence angle results in wider and more symmetrical transition zones and a decrease in cold volumetric flow rate deflects the transition zone towards the $y = 0$ wall, improving the configurations with smaller angles (enhancing size and symmetry).

Keywords

Heat transfer in microchannels; T and Y shaped microchannels; Light Induced Fluorescence ; Non isothermal flows

Resumo

A microfluídica revolucionou o mundo através da sua capacidade de executar múltiplas operações, num único *chip* com tamanhos na casa dos micrómetros. Dependendo do propósito e aplicação do dispositivo, microcanais de diferentes designs são implementados, com os sistemas normalmente a serem integrados com outras tecnologias de deteção, resultando em análises rápidas e eficazes, tudo isto utilizando amostras com quantidades muito pequenas de líquidos e reagentes.

Neste trabalho, foi discutido o impacto do ângulo de confluência, ângulo formado entre as duas entradas e uma saída de fluído, e do caudal volumétrico nos perfis de temperatura, dentro dos microcanais. A técnica *light induced fluorescence* LIF (fluorescencia induzida por luz), usando uma solução fluorescente de corante Rodamina B , foi aplicada para obter a temperatura do escoamento. Um micro aquecedor foi concebido para a calibração da técnica, depositando alumínio em cima de um substrato de vidro e padronizando-o de forma a obter o *design* pretendido. A *direct write laser* (DWL) foi utilizada para criar a *hardmask*, fotolitografia para o molde de SU-8 e litografia suave para o dispositivo microfluidíco de PDMS, selado irreversivelmente contra uma membrana do mesmo material, recorrendo a um tratamento de plasma de oxigénio. As estruturas resultantes tinham duas entradas de fluído com ângulos de confluêcia diferentes ($30°$,$60°$,$90°$,$135°$) e uma saída. Uma análise de transferência de massa vs calor foi levada a cabo para o microcanal com um ângulo de $90°$. Os diferentes tipos de configurações de microcanais (diferentes ângulos de confluência) foram testados para um caudal volumétrico fixo na entrada quente de $Q_{quente} = 50\mu L/min$, e variável na entrada fria de $Q_{frio} = 25, 50, 75\mu L/min$. Os resultados mostraram que para o canal com a geometria de $90°$, a difusão de calor é mais forte que a de massa. Um aumento no ângulo de confluência resulta em zonas de transição mais largas e simétricas, e que uma redução na caudal volumétrico na entrada fria desvia a zona de transição na direcção da parede $y = 0$ melhorando as configurações com ângulos menores (melhorando simetria e tamanho).

Palavras Chave

Transferência de calor em microcanais; microcanais em T e Y; Fluorescência induzida por luz (LIF); Escoamentos não isotérmicos

Contents

List of Figures

Nomenclature

Greek Symbols

α	Thermal diffusivity ($m^2/2$)
α_{abs}	Absorptivity ($-$)
β	Collection coefficient ($-$)
ϵ	Emissivity ($-$)
ϵ_{abs}	Absorption coefficient (m^2/kg)
μ	Dynamic viscosity ($Pa.s$)
ν	Kinematic viscosity (m^2/s)
Φ	Quantum yield ($-$)
ϕ	Species concentration
ρ	Fluid density (kg/m^3)
σ	Stefan-Boltzman constant ($W/m^2.K^4$)
σ^2_{max}	Maximum variance ($-$)
Θ	Non dimensional temperature ($-$)

Roman Symbols

$\bar{c}$	Mean value of concentration field c ($-$)
ΔT_{a_i}	Maximum temperature difference at section a_i (℃)
$\dot{E}_g$	Energy generated internally by the system (W)
$\dot{E}_{in}$	Energy entering the system (W)
$\dot{E}_{loss}$	Energy lost by the system (W)
$\dot{E}_{out}$	Energy leaving the system (W)
$\dot{E}_{st}$	Energy stored by the system (W)
$\dot{m}_i$	Mass flow rate (kg/s)
$\dot{Q}$	Volumetric flow rate (m^3/s)
∇T	Temperature gradient (℃)
A	Cross section area (m)
a_i	Pixel intensity values at section of analysis i in the outlet channel
b	Absorption path length ($-$)
C	Dye concentration (kg/m^3)
C_p	Specific heat ($J/Kg.K$)
D_H	Hydraulic diameter (m)
E	Emissive power (W/m^2)
E_b	Black body emissive power (W/m^2)
G	Incident radiation (W/m^2)
G_{abs}	Absorbed incident radiation (W/m^2)
h	Convection heat transfer coefficient ($W/m^2.K$)
H_i	Enthalpy (J/kg)
I	Fluorescence itensity emited (W/m^3)
I_0	Light intensity flux (W/m^2)
I_M	Intensity of mixing ($-$)
I_N	Non dimensional pixel intensity value ($-$)
I_S	Segregation intensity ($-$)
$I_{RhB,T_{room}}$	Rhodamine B fluorescence intensity at room temperature (W/m^3)

I_{RhB}	Rhodamine B fluorescence intensity (W/m^3)
J	Mass diffusion flux
k	Thermal conductivity ($W/m.K$)
Le	Lewis number ($-$)
Nu_T	Constant temperature Nusselt number ($-$)
P	Wetted perimeter (m)
Pe	Peclet number ($-$)
Pr	Prandtl number ($-$)
$q"_{cond}$	Heat flux by conduction (W/m^2)
$q"_{conv}$	Heat flux by convection (W/m^2)
$q"_{rad}$	Heat flux by radiation (W/m^2)
Q_1	Volumetric flow rate at inlet 1 ($\mu L/min$)
Q_2	Volumetric flow rate at inlet 2 ($\mu L/min$)
Q_{cold}	Volumetric flow rate at cold inlet ($\mu L/min$)
Q_{hot}	Volumetric flow rate at hot inlet ($\mu L/min$)
Q_{out}	Volumetric flow rate at outlet ($\mu L/min$)
Re	Reynolds number ($-$)
S_0	Electronic ground state
S_1	Electronic exited state
S_i	Mass-distributed external force (N/m^3)
Sc	Schmidt number ($-$)
T	Temperature ($^{\circ}C$)
T_∞	Fluid temperature ($^{\circ}C$)
T_i	Temperature at inlet i ($^{\circ}C$)
T_s	Surface temperature ($^{\circ}C$)
T_{amb}	Ambient temperature ($^{\circ}C$)
T_{cold}	Temperature at cold inlet ($^{\circ}C$)
T_{hot}	Temperature at hot inlet ($^{\circ}C$)
T_{wall}	PDMS wall temperature ($^{\circ}C$)
u	Flow average velocity (m/s)
$u(y,z)$	Velocity in the main flow direction (m/s)
u_i	Fluid velocity i-direction (m/s)
x_i	Spacial i-direction (m)
$x_{fd,h}$	Hydrodynamic entry length (m)
$x_{fd,t}$	Thermal entry length (m)
y	Vertical direction along the channel height (m)

Acronyms

CAD	Computer Aided Design
CCD	Charge Couple Device
CVD	Chemical Vapor Deposition
DNA	Deoxyribonucleic Acid
DWL	Direct Write Laser
IAD	Ion Assisted Deposition
LIF	Light Induced Fluorescence
LOC	Lab-on-Chip
MTT	Molecular Tagging Thermometry
PCR	Polymerase Chain Reaction
PDMS	Polydimethylsiloxane
PMMA	Poly(Methyl Methacrylate)
PR	Photoresist
PVC	Polyvinyl Chloride
PVD	Physical Vapour Deposition
RF	Radiofrequency
RhB	Rhodamine B
RTD	Resistance Temperature Detectors
SVG	Silicon Valley Group
TGF	Temperature Gradient Focusing
TLC	Thermochromic Liquid Crystals
UV	Ultraviolet

Chapter 1

Introduction

1.1 Motivation

The development of lab-on-chip (LOC) technology is being increasingly used in a wide range of applications due to its benefits when compared to conventional macroscopic equipment. These benefits include small reagent volumes, fast response times, low cost, disposability, and reduction or elimination of cross contamination. For this reason, these *chips* and microfluidics in general are used in a vast range of applications including environmental sensing, medical diagnostics (HIV, tuberculosis, hepatitis, and malaria [1]), drug discovery, drug delivery [2], microscale chemical production, combinatorial synthesis and assays, artificial organs, micro propulsion and microscale energy systems.

Temperature control in microfluidic applications is crucial for a vast range of situations. Examples are polymerase chain reaction (PCR), temperature gradient focusing (TGF), digital microfluidics, mixing, or protein crystallization. Using light induced fluorescence (LIF), a non-intrusive technique to determine temperature, temperature profiles can be evaluated inside these micro devices and the impact of changing variables like confluence angle or volumetric flow rate can be studied in order to increase the process efficiency.

The main motivation of the present work is to characterize the mixing of two fluids at different temperatures in straight square cross section channels with T and Y shaped confluence angles ($30°$,$60°$,$90°$,$135°$), subjected to three different volumetric flow rates ($25, 50, 75 \mu L/min$).

1.2 Objectives

In order to characterize the thermal and mass mixing process inside the different shaped microchannels, this work was split in three main parts, each one essential to reach that aim.

Micro-fabrication (microfluidic devices and heaters) and preparation of all the components and techniques (LIF) needed to perform the experiments.

Mass (Rhb concentration) vs thermal (Non-dimensional profiles) mixing comparison in the T-shaped microchannel and thermal mixing quality (using temperature profiles) evaluation for that case.

Characterization of thermal transition zones for the different microchannel configurations (confluence angles) and volumetric flow rates.

1.3 Thesis outline

This thesis is divided in 5 chapters, including this one that states the motivation, main objectives and the outline of the chapters.

In chapter 2 a bibliographic revision of the most important subjects in the present work is addressed. Microfluidics is addressed, techniques to evaluate the temperature in microfluidics devices are presented and heat transfer in these devices is tackled as well. Insight on microfabrication and lithography processes is also provided in this chapter.

Chapter 3 details the fabrication of all the components and the techniques required to perform the experiments. The components include the microfluidic device, heaters and the experimental set-up itself, while the techniques addressed in this chapter are the LIF calibration and the digital image processing protocol necessary to treat and analyze the raw experiment data.

In chapter 4 the experimental results are presented and discussed. Firstly, the isothermal case is introduced and then a comparison with the non-isothermal case is performed. Mixing of fluid (mass and heat) gradients are addressed as well as transition zones (zone with different mass concentration/temperature). Secondly, results for different configurations of inlets in the microchannels are shown and discussed. Lastly, the impact of changing the cold volumetric flow rate will be debated.

In chapter 5 an overall view of the results obtained in chapter 4 is presented leading to the conclusions. Suggestions for future work are included in this chapter.

Chapter 2

State of the art

2.1 Microfluidics and heat transfer

Microfluidics allows for the fabrication of millions of microchannels that perform several operations on a single chip with sizes in the micrometer range. Depending on the purpose and application of the device, different channel designs can be implemented, with the systems often being integrated with detection technologies, this results in quick analyses and effective results while sampling very small amounts of fluids and reagents, in the order of femtoliters (fL) [3].

Microfluidics can be defined as "(. . .) The science and engineering of systems in which fluid behavior differs from conventional flow theory primarily due to small length scale of the system." [4], which is a generally accepted engineering definition. It is both a scientific area that studies the fluid behavior through micro-channels, and the technology of manufacturing microminiaturized devices with carved pattern through which fluids can flow or be enclosed. Microfluidics has a wide range of applications including environmental sensing, medical diagnostics, drug discovery, drug delivery, microscale chemical production, combinatorial synthesis and assays, artificial organs, micro propulsion and microscale energy systems.

The ease of customization and manufacture, the type of materials used for production, the ability to manipulate accurately and precisely the (bio)particles flowing in the introduced fluid samples, make microdevices efficient and reliable, yielding effective results with insignificant percentage error [5]. The process time, compared to traditional methods of diagnosis, is also reduced from hours, and even days, down to minutes. The miniature, compact configuration of microfluidic devices shows a substantial advantage in terms of portability, accessibility, and ease-of-use. Lab-on-a-Chip (LOC) devices use microfluidics for applications such as Point of Care testing of diseases, or Organ on a Chip studies. Their development requires the integration of multiple functions within a very small platform, easily transportable and that is capable of delivering a quick result. LOCs allow for an easy use by patients in monitoring and accessing certain health aspects such as blood urea nitrogen values, important for controlling kidney disease, or checking electrolytes levels during diuretic therapy [6].

In an economic perspective, the venture capitalist Vinod Kholsa, in his article for TechCrunch, predicted that an integration between future diagnostic devices and state-of-the-art algorithms could take the place of 80% of doctors [7]. While not being immediate, this highlights the importance of this growing technology. Nowadays LOCs are already being used as an effective rapid diagnosis of infectious diseases such as HIV, tuberculosis, hepatitis, and malaria [1]. Developing countries and poor areas could benefit from this technology. Microchannels have been incorporated in micromachined devices like micropumps, microvalves and microsensors incorporating single-phase liquid flow. More recently they got the attention of the biological and life sciences, fulfilling a need of analyze biological materials such as, deoxyribonucleic acid (DNA), cells, proteins and chemical reagents. Microchannels play an important role in pre-mixing chemical species before they enter a reaction chamber increasing the process efficiency. The high heat flux dissipation observed in high-speed microprocessors enhanced the studies on heat transfer in microchannels. Microelectromechanical devices development calls for smaller heat removal systems. Fluid transport and thermal control is required in very small passages, of several micrometers, to allow further breakthroughs in biomedical and genetic engineering [8]. Flow inside the microchannel is described by the continuity and Navier-Stokes equations as follows:

$$\frac{\partial \rho}{\partial t} + \frac{\partial}{\partial x_i}(\rho u_i) = 0 \tag{2.1}$$

$$\frac{\partial u_i}{\partial t} + \frac{\partial}{\partial x_i}(\rho u_i u_j) = -\frac{\partial p}{\partial x_i} + \frac{\partial \tau_{ij}}{\partial x_j} + S_i \tag{2.2}$$

Where:

- x_i is the spatial i-direction (m/s).
- u_i is the fluid velocity component in the i-direction (m/s).
- ρ is the fluid density (kg/m^3).
- S_i is a mass-distributed external force per unit volume (N/m^3).
- τ_{ij} is the viscous shear stress tensor (N/m^3).

Microfluidics is not only efficient and convenient, but it offers a low cost of production per device when comparing to other traditional technologies, resulting not only in an effective production but also disposal [9]. The two main reasons for this cost-effectiveness are the materials used to fabricate microfluidic devices and the methods of production. Materials used in the manufacturing of these devices are silicon, glass, thermoplastics or paper.

When working in biological applications, two main requirements have been reported, the first one being the need of maintaining a stable temperature of 37℃ to keep cells alive [10]; the effect of temperature on the response of cells to stimulus can be studied as long as temperature is homogeneous. Secondly, the temperature control in Polymerase Chain Reactions which is used widely in molecular biology in order to amplify target DNA in vitro. In both cases are examples of the need of a spatial homogeneity of the temperature profile. Temperature control, the subject of the present work, is essential for a vast range of applications in micro-devices, either in terms of profile (homogeneous or gradient) or in accessible range (Temperature range).

When working at microscale level, the common methods to measure temperature cannot be directly applied. These methods can be invasive or noninvasive. As the name suggests, noninvasive techniques are the ones that induce none to minimum impact on the system they are focused in. High-precision thermocouples, integrated resistance temperature detectors (RTD) and infrared thermography are examples of intrusive techniques. A high-precision thermocouple consists of two wire legs made from different metals welded at one end. That end is called a junction, which when subjected to a temperature change, creates a voltage that is converted to temperature using a preprogramed device. This thermocouple probes cannot be accurately used since the characteristic size of the junction is comparable to the microchannel cross section, resulting in poor spatial and temporal resolutions [11] and clogging. The integration of RTDs in microfluidic devices results in better spatial resolution but fails in providing information about local fluid temperature. A RTD consists of a resistance element and insulated copper wires. It works based on a basic principle: as the temperature of a metalic resistance element increases, so does the resistance to the flow of electricity. Electrical resistance (Ω) is then converted to temperature based on the characteristics of the element. Typical response time for a RTD is between 0.5 and $5s$ making them usually unsuitable (slow) for microscale applications. Infrared thermography is the process of using a thermal image to detect radiation (heat) coming from an object, converting it to temperature and displaying an image of the temperature distribution. It can also be used in surfaces, requiring an accurate value of the emissivity of the medium, which increases its complexity.

Examples of noninvasive whole-field temperature measurement methods examples are thermochromicliquid crystals TLC, molecular tagging thermometry (MTT) or light Induced Fluorescence (LIF). TLC uses a substance that exhibits a definite color at a specific temperature being usually used in a solution. As temperature changes so does the color and that way, after performing a calibration process, temperature can be addressed. MTT uses a pulsed laser to tag a phosphorescent molecule, which is a molecule that emits light after being exposed to radiation, premixed with water. The temperature is obtained based on the dependence of the phosphorescence lifetime with temperature. LIF is a spectroscopic method in which an atom or molecule, in this work rhodamine B (RhB), is excited to a higher energy level by the absorption energy followed by spontaneous emission of light, which is generally called fluorescence.

In this work the LIF technique was applied to study the mixing of two fluids at different temperatures in micron sized channels of square cross section.

2.2 LIF fundamentals

A photon is absorbed when its energy matches the energy gap between energetic states of that molecule. There are three types of energy states. From most energetic to least, electronic, vibrational and rotational. Each state is related to the emission in different wave length levels: electronic in the visible, vibrational in infrared and rotational in microwave spectrum regions as displayed in (Figure 2.1). After photon absorption and consequently a jump in energy state, the molecule can return to its energy ground state by non-radiative (via intra and intermolecular energy dissipation) and radiative process (through photon emission). For this work only the latter will be discussed since photon emission is essential for the LIF method.

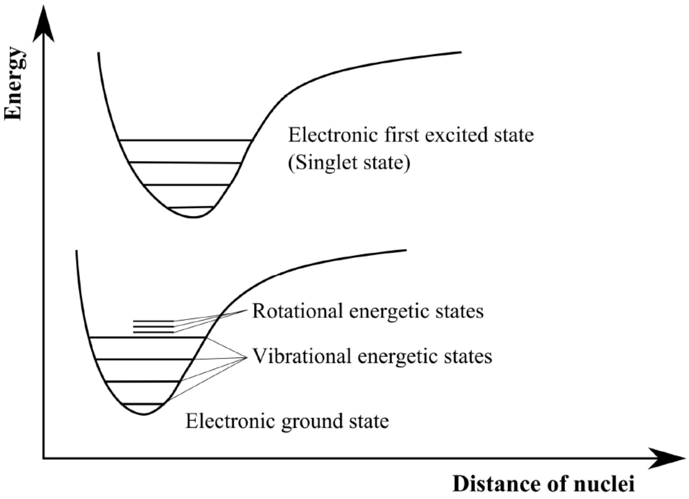

Figure 2.1: Different energetic states of a molecule. Energy differences of electronic states are larger than energy differences of vibrational and rotational energetic states [12].

Absorption of a photon with appropriate energy causes an electronic transition of a dye molecule from the ground state to the singlet state $(S_0 \rightarrow S_1)$ (Figure 2.2). This transition can occur from any existing vibrational energy level of S_0 to any vibrational energy level of S_1, see Figure 2.2. Fluorescence is taking place from the lowest vibrational level of the S_1 state to any vibrational level of the S_0 state (ground state). Phosphorescence results from radiative transition from the triplet state to the ground state $(T_1 \rightarrow S_0)$ and photoluminescence is a combination between phosphorescence and fluorescence (Figure 2.2). Photoluminescence is an example for the interaction of matter and electromagnetic radiation. It results from absorption and spontaneous reemission of a photon by a molecule.

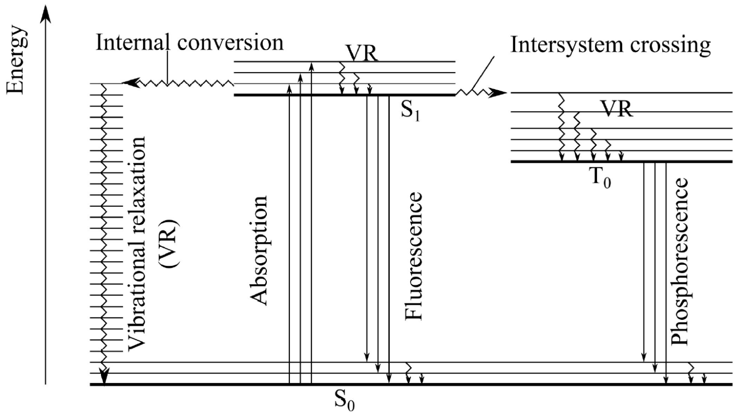

Figure 2.2: Jablonski diagram visualizing energetic states and possible radiative (straight arrows) and non-radiative transitions (staggered arrows) between these states [12].

To excite the dyed solution, energy needs to be provided. The fluorescence intensity emitted per unit volume, $I[W.m^{-3}]$ depends on the light incident flux $I_0[W.m^{-2}]$, the dye concentration $C[kg.m^{-3}]$, quantum yield $\Phi[-]$ (ratio of photons emitted and absorbed by the molecule, which depends on the temperature of the molecule) and the absorption coefficient $\epsilon_{abs}[m^2/kg]$ according to J. Sakakibara and R. Adrian [13]:

$$I = I_0 C \Phi \epsilon_{abs} \tag{2.3}$$

For low dye concentrations (in our case $25mg$ of RhB per liter of de-ionized water), [11] (2.3) becomes:

$$I = I_0 C \Phi \epsilon \beta_C b \tag{2.4}$$

Where β_C is the collection efficiency $[-]$ and b is the absorption path length $[-]$.

Images are taken at different temperatures and the corresponding fluorescence intensity values for each are stored. The fluorescent intensity values can be negatively influenced by multiple factors like optical setup, non-uniform illumination, photo-bleaching (reduction of the ability of a molecule to fluoresce resulting in fading signal intensity), chemical reactions (leads to new species showing no or altered fluorescence), solvent relaxation (light shifted to longer wavelength resulting in less energy being released), auto absorption and reemission effects due to Beer-Lambert law (due to overlap of emission and absorption spectra emitted radiation gets re-absorbed) and others. To tackle these, a normalization technique needs to be implemented, where the fluorescence intensity at room temperature is used to normalize all experiment data with the expression (2.5).

$$I_{HS-\mu LIFT} = \frac{I_{RhB}}{I_{RhB,T_{room}}} \tag{2.5}$$

Where $I_{HS-\mu LIFT}$ is the normalized fluorescence intensity, $I_{RhB}[W.m^{-3}]$ the fluorescence intensity at a certain temperature T and $I_{RhB,T_{room}}[W.m^{-3}]$ the fluorescence intensity at room temperature. This should make the technique system-independent and allows to correct errors that are invariant in time, or whose variation is known between any pair of images as presented by J. Crimaldi and J. Koseff [14]. After having the normalized values, dividing all the intensity values from the different images by the room temperature image, a normalized intensity vs temperature plot is obtained and, after inverting it, it is possible to directly relate temperature to fluorescence intensity [12].

LIF technique is of interest if phenomena are taking place on small spatial and temporal scales. In heat transfer at small-scale, highly transient mechanisms play a huge role during nucleate boiling and other phase transition processes, with these mechanisms being only partly understood due to their complex nature. Research activities focus on this subject, since the energy efficiency of many devices and industrial processes can be increased by an optimization of the heat transfer rates.

In this work, a characterization of the thermal profile in the channels will be addressed. It is mandatory to understand heat transfer and fluid flow in these microscale systems in order to better develop design and improve operation. In the absence of the electrokinetic or electroosmotic forces, the flow is expected to obey to macrofluidic laws without suffering any fundamental changes. In the literature [15], the author claimed that liquids like water, used in this work, should be treated as continuous media with the results obtained from classical theory being applicable in channels larger than 1μm, which is two orders of magnitude lower comparing to this work dimensions, meaning that macroscale theory should hold. Nevertheless, mass transfer in laminar and turbulent flow transport equations is not yet fully experimentally validated, transition from laminar to turbulent flow needs to be further evaluated, relative roughness effects (on transition, heat transfer, friction factors) should deserve close attention and the use of empirical constants derived from macroscale experiments should be used with careful and further developed to better fit microscale.

The use of optical measurement methods can play a crucial role in helping to understand these phenomena and to validate existing numerical models. These methods are being increasingly used intensively over the last years due to the great progresses in image acquisition (cameras) technology and soft/hardware for image processing. The development of digital highspeed cameras with framerates up to $15000 fps$ and more than 1000×1000 pixels of spatial resolution lead to an increasing importance of these techniques in science over the widely-used contacting measurement devices, like thermocouples, resistor-type thermometers or liquid expansion thermometers.

2.3 Microfabrication techniques

To fabricate the components of the experimental setup (thin film heaters and polydimethylsiloxane (PDMS) device, it is important to tackle some fundamentals on microfabrication. In general microfabrication can be divided in three major steps: deposition, lithography, and etching. A brief overview of the three is given bellow.

2.3.1 Deposition

Deposition is the process in which a thin film is deposited upon a substrate (commonly silicon or glass). This film can be a metal, an oxide or a nitride as examples. Accordingly to the material chosen, different techniques may be needed to correctly deposit the film. There are three main technologies for thin-film deposition: physical deposition (Sputtering), chemical deposition (Ion implantation) and physical-chemical deposition (Electroplating).

2.3.1.A Physical deposition (PVD)

Physical deposition (PVD) is mainly used for deposition of metal and alloys since it has high deposition rates and grain control size (ion beam deposition). PVD involves vaporizing a solid material in a vacuum, then depositing it onto a substrate. Vaporization can occur by three main ways: e-beam evaporation (electron beam), ion assisted deposition (IAD), thermal evaporation. A detailed explanation of electron beam will be addressed since it is the most common technique used and was applied to this work. The main concept of this technique is to use momentum transfer of ions to eject atoms from a target transferring them to the substrate, forming a film using the target material. This film accumulates in the substrate due to its lower electrical potential. To create the required conditions, inside the chamber, a powerful radiofrequency (RF) stimulation is applied to generate a highly energized plasma. A gas (sputtering gas) is inserted into the chamber, usually argon due to a combination of its atomic weight and inertness, changing from an atom to a positively charged ion (Ar^+) by interaction with other particles. These Ar^+atoms are attracted by the target (cathode) due to their positive charge, "etching" the atoms at the sputtering surface of the target ejecting them towards the surface of the substrate (Figure 2.3).

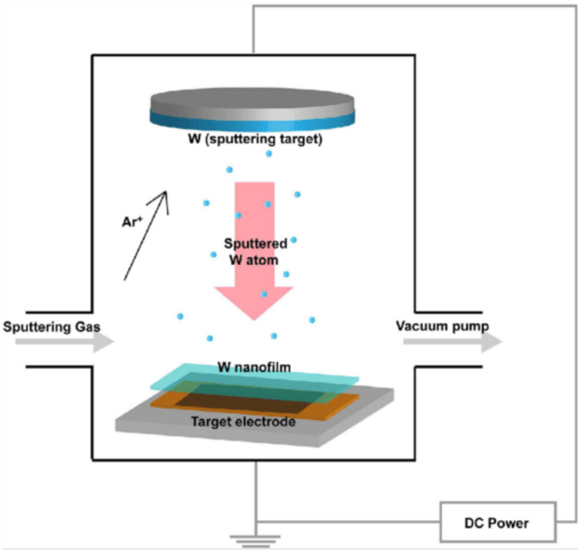

Figure 2.3: Example of physical vapour deposition (PVD): Tungsten Nanolayer Coating on Si Electrode [16]

For this to happen efficiently, a powerful vacuum is needed in order to prevent the scattering of the Ar^+ ions away from the sputtering target by other particles present inside the chamber. This is also true for the scattering occurring at the sample surface and, when controlled, results in a better throughput, better harnessing of the target atoms (better target efficiency) and higher deposition rates. These are the goals to achieve and for that, air pressure is a fundamental property for PVD. In Figure 2.4 the dependence of the mean free path with pressure is presented. When pressure decreases, the mean free path increases, meaning that, for a low pressure, the probability of a molecule, in this case nitrogen, colliding with another is much smaller than at high pressure. Since molecular density increases with pressure, the probability of molecular collision is higher.

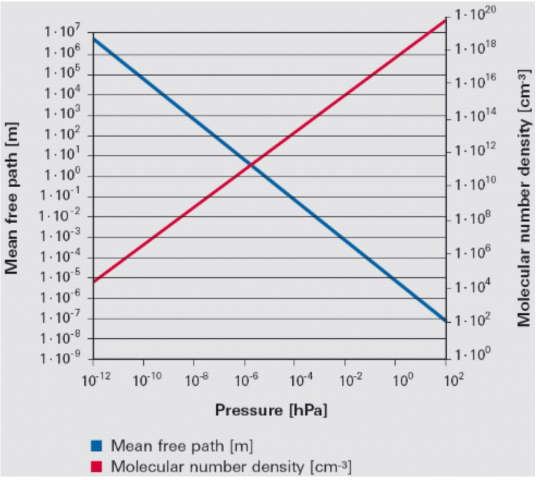

Figure 2.4: Molecular number density (red, right-hand y axis) and mean free path (blue, left-hand y axis) for nitrogen at a temperature of 273.15 K [17].

In this work magnetron sputtering deposition, a specific type of sputtering deposition, was used since it enhances the efficiency and swiftness of the process without the need of increasing chamber temperature (which would result in increased particle mobility). A magnetron, device that produces strong microwaves, is added to the setup producing a magnetic field along the target. This magnetic field will concentrate the electrons around the target, enhancing the probability of the inert gas atoms hitting it and becoming sufficiently energized to remove atoms from the sputtering target by momentum transfer. This increase in inert gas atoms hitting the sputtering target, although allowing the use of a lower temperature inside the chamber, results in heating of the magnetron due to energy dissipation, requiring cooling usually achieved with water. Figure 2.5 illustrates how magnetron deposition works [18] [19].

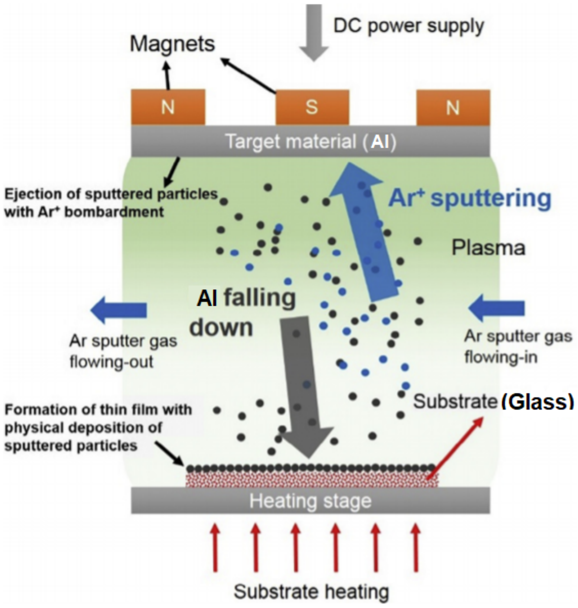

Figure 2.5: A schematic of the DC magnetron sputtering process [20].

Coatings created using PVD are highly durable, resistant to scratching and corrosion. Nevertheless, since they usually occur at higher temperatures and vacuum levels than other deposition techniques, degradation of the sample can occur, so caution is advised.

2.3.1.B Chemical Vapor Deposition (CVD)

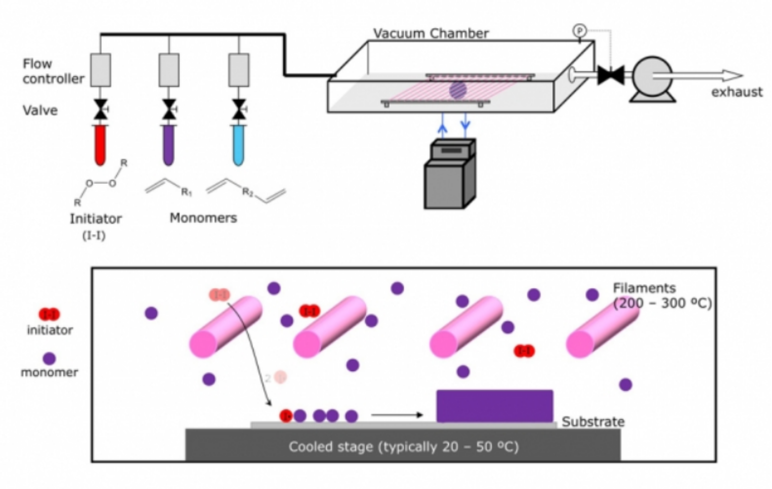

Figure 2.6: A schematic of the chemical vapor deposition (CVD) process [21].

Chemical Vapor Deposition differs from PVD since the atoms are chemically generated at the surface instead of being physically deposited on a substrate. CVD refers to the formation of a non-volatile solid film on a substrate, resulting from the reaction of vapor phase chemical reactants containing the proper constituents. First, a predefined mix of reactant gases and diluent inert gases is introduced at a specified flow rate into the reaction chamber. The gas species move to the substrate, with the reactants getting adsorbed on the surface of the substrate, undergoing chemical reactions forming the film. Lastly, the gaseous by-products of the reactions are desorbed and exhausted from the reaction chamber. Figure 2.6 exemplifies the process.

This method is used to produce high quality, high-performance, solid materials. The process is often used in the semiconductor industry to produce thin films [19].

2.3.1.C Physical-chemical Vapor Deposition

Physical-chemical deposition is a combination between physical and chemical depositions. One main example of this concept is electroplating. This process uses an electric current to reduce dissolved metal cations so that they form a thin coherent metal coating on an electrode. The anode is made of the metal to be plated on the cathode. Both components are submerged in a solution, called an electrolyte, including one or more dissolved metal salts as well as other ions that allow the flow of electricity. The metal atoms are then oxidized and dissolved in the solution by applying a direct current to the system, using a power supply. The dissolved metal atoms are reduced at the surface of the cathode forming a coating. This process can produce thick films by controlling the electrochemical parameters of the setup.

Films produced this way are typically less resistance to corrosion since this technique cannot produce intertwined alloys like PVD can.

2.3.2 Etching

Etching is used to remove specific unprotected layers for multiple purposes like wafer planarization, pattern transferring, isolation or cleaning. In deposition processes material is added but usually, undesired material needs to be removed to obtain the final design. According to the material to be removed, a suitable etchant needs to selected. The work of Williams et al. [22] or a similar document can be consulted for a correction etchant selection. Etching can be performed by two different ways, dry (plasma) etching and wet (chemical) etching (Figure 2.7).

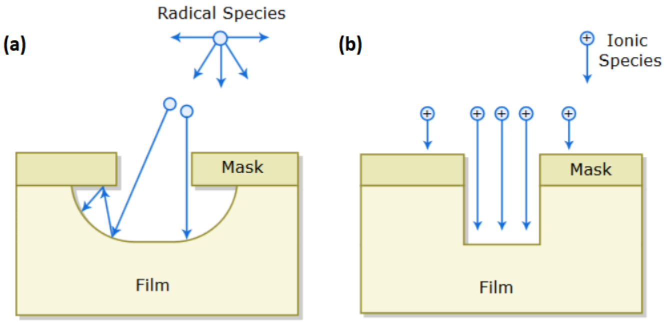

Figure 2.7: Illustration of etching techniques; (a) Wet (chemical) etching ; (b) Dry (plasma) etching

Dry etching, also called plasma etching, uses plasma or etchant gases to remove material from the substrate at low pressure (few millitorr) and low temperature (from room temperature to 250℃). It is more controllable, precise, and repeatable, when compared to wet etching, since a plasma is used instead of a liquid etchant to remove the materials. In dry etching a complex vacuum system is required to perform the process. Using a plasma to perform the etching process enables design with features sizes smaller than $100nm$ [23]. Etching has three main metrics, etch rate, uniformity and selectivity. The first is defined as etched depth per unit time. High etch rates are harder to control and are used for deep hole etching (deep penetration holes in wafers). The second metric refers to the percentage variation of the etch rates across a wafer. The latter is the ratio of the etch rates of one material over the other. A very high selectivity means that only the selected layer is etched without harming the substrate or the mask.

Wet etching removes the materials by immersing the wafers in a chemical solution that reacts with selected films to form soluble by-products. It is cost efficiently with easy implementation and it etches quickly. Sometimes, high selectivity (etching only the material intended without damaging the others) can also be achieved. However, it can result in high levels of defects on wafers, it is ineffective when used in features sizes smaller than $1\mu m$, challenging to control, and (being a chemical process) it yields chemical waste [24].

Etching can be isotropic or anisotropic. Isotropic etching has the same etch rate in all directions while anisotropic has different etch rates in the lateral and vertical directions (Figure 2.8).

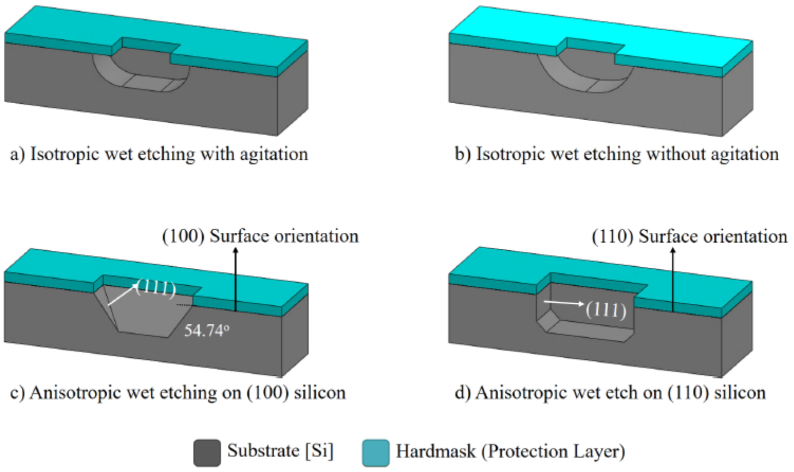
a) Isotropic wet etching with agitation
b) Isotropic wet etching without agitation
c) Anisotropic wet etching on (100) silicon
d) Anisotropic wet etch on (110) silicon

Figure 2.8: Characteristic etched profiles obtained by isotropic or anisotropic etching [25].

Figure 2.8 shows the difference between isotropic (a and b) and anisotropic (c and d) etching . Wet isotropic etching (orientation independent) makes use of aqueous acidic solutions containing HF (hydrogen fluoride) and HNO (azanone) or HNA (mixture of HF, CH_3COOH (acetic acid) and HNO3 (nitric acid)) to remove materials from the substrate while anisotropic etching uses crystal-orientation etchants of silicon (e.g., hydroxides of alkali metals) [25]. Wet etching was used in this work and the procedure is explained in the materials and methods chapter.

Since the removal of unwanted material is being discussed, it is important to address another technique called lift-off, which is also used for patterning. In lift-off, a sacrificial layer is deposited on the surface of the sample, usually a photoresist (PR). This PR layer is then inversely patterned before a target material is deposited. The sacrificial layer is then removed (lift-off), removing the material deposited on top, reveling the final design [26]. Figure 2.9 summarizes the process.

Lift-off is mainly used in large structures (μm), due to the risk of complete peel-off of the material, which is more likely to happen in smaller delicate structures (nm to few μm).

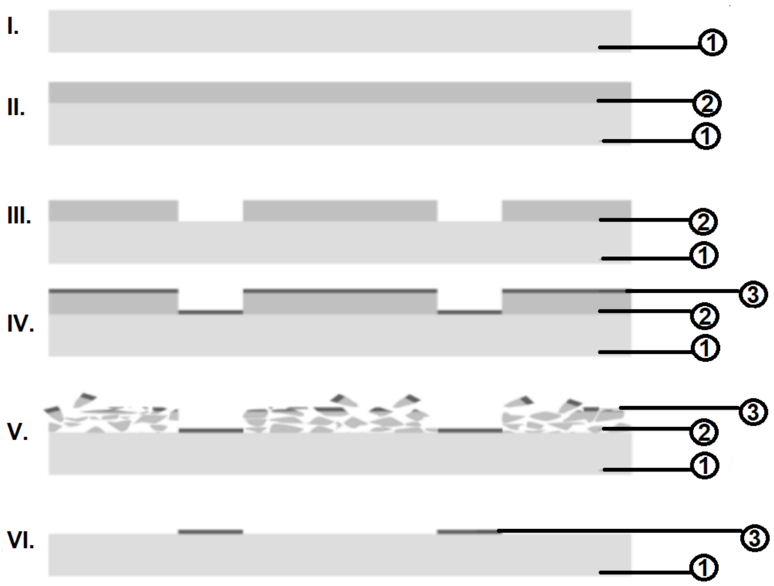

Figure 2.9: Lift off process steps (I. Substrate preparation, II. Sacrificial layer deposition, III. Patterning the sacrificial layer, IV. Target material is deposited, V. Washing both the sacrificial layer and target material, VI. Final patterned layers. (1. Substrate, 2.Sacrificial layer, 3.Target matter) [27].

2.3.3 Lithography

In this section the subjects of photolithography and soft lithography will be addressed since they are used to fabricate multiple components needed for the experimental work.

2.3.3.A Photolithography

Photolithography is the process used in microfabrication to pattern a certain *design* on a thin film or a substrate (typically a wafer). It needs to be performed in a clean environment since the standard size of airborne particles and the scales used in microfabrication are similar. Photolithography uses a photosensitive organic film called photoresist (PR). This PR is photosensitive changing properties when exposed to light (usually ultraviolet (UV)). There are two types of photoresist, positive (soluble in the developer after exposed) and negative (becomes insoluble in the developer after exposure), Figure 2.10.

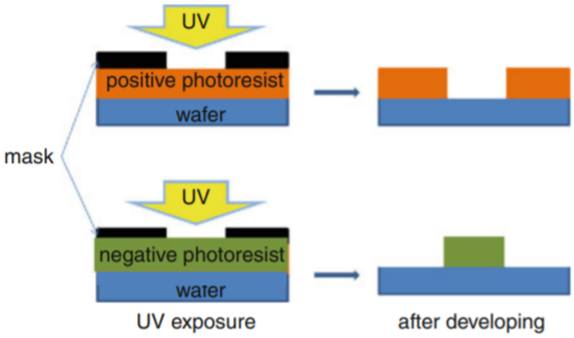

Figure 2.10: Positive and negative resist: exposure, development, and pattern transfer [28].

To perform photolithography, the PR (in this work SU-8) is poured into a substrate and spinned to allow a correct (even) distribution. Different speed rotations and accelerations result in different PR thicknesses allowing for different patterns. The coated substrate is selectively exposed, usually a UV light with a spectral band between $300\text{-}450nm$, through the photomask. A photomask normally consists of a deposition of aluminum, opaque to light, on a glass substrate where PR is deposited to allow patterning, when exposed to UV light using a direct writing laser (direct write laser (DWL)) (Figure 2.11). This machine patterns the PR using UV light matching the design created in a computer aided design (CAD) *software*.

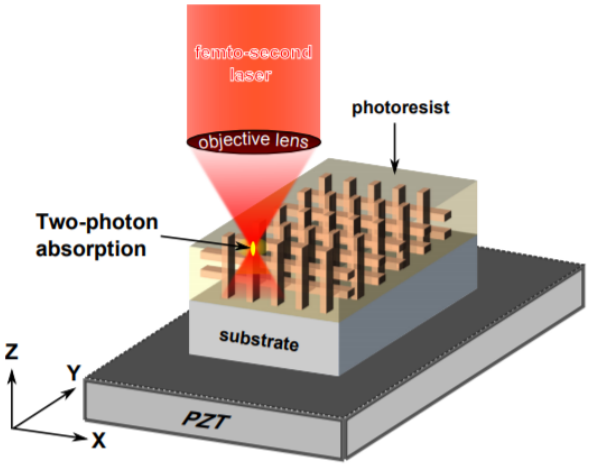

Figure 2.11: Schematic illustration of a direct laser writing system [29].

After exposing, an etching process is needed to remove the unwanted material. A wet etching solvent is applied, typically weak basic solutions varying from resist to resist, to obtain the final features. The resulting masks are used to created reusable molds, containing the designed features [30], [25].

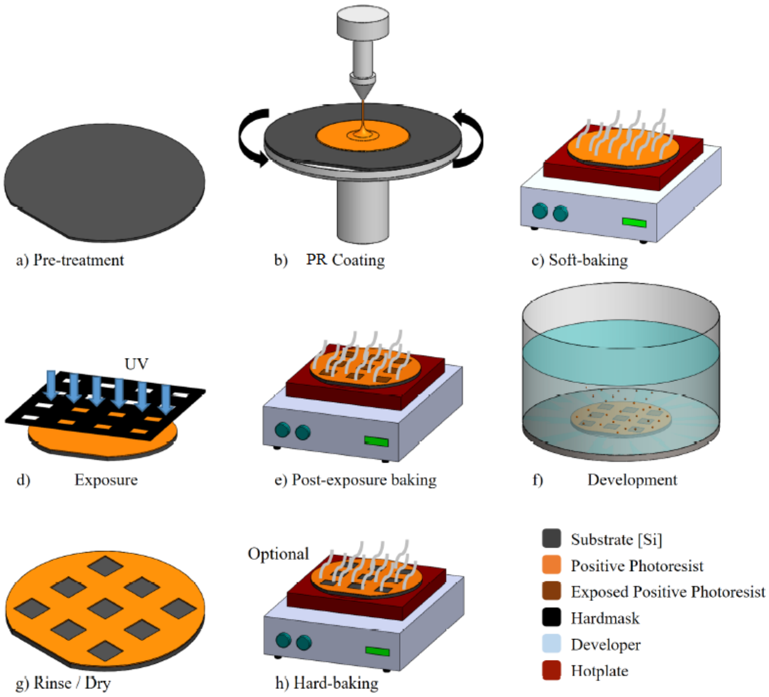

Figure 2.12: Fabrication of the master mold by photolithography [25].

For the fabrication of the the mold, first a silicon substrate is spin-coated with SU-8 negative photoresist followed by a baking step, removing any solvent that did not evaporate during the process. The previously created mask is then placed on top of the coated substrate and the structure is aligned. The photoresist on the silicon substrate is exposed to UV light in order to transfer the patterns to the mold. If a positive photoresist is used the areas exposed to UV light became soluble, for negative they became insoluble. The final step is to apply a developer to remove the unwanted photoresist, revealing the final design of the mold. Figure 2.12 summarizes the process for a negative PR [25].

2.3.3.B Soft lithography

PDMS

“Soft lithography is the technique used to rapidly and easily fabricate and replicate a wide range of elastomeric devices, i.e., mechanically soft materials (e.g., polymers, gels or organic monolayers) without costly capital equipment.” [25] Due to its simple fabrication procedure and strong sealing to a wide range of material, PDMS has become the most commonly used elastomer in rapid prototyping of microfluidic devices. It is composed of a two-part heat-curable mixture, a pre-polymer and a curing agent. The first is cross-linked with the latter usually in a 10:1 ratio in weight, but changing this ratio results in a mixture with different mechanical and chemical properties. Fabricating microfluidic devices using

PDMS reduces cost, improves biocompatibility and chemical inertness, decreases toxicity (comparing to other methods), enhance versatility, increases ease of manipulation and durability when compared to other materials used in soft lithography like polymers, gels, and organic monolayers [31]. Nevertheless, fabrication scale-up is compromised due to difficulties in repeatability and handling as a result of material softness. Being sensitive to minute changes in applied pressure, PDMS compression may result in deformation of the structure features or even cracks. The use of PDMS is more viable for low aspect-ratio channels since high aspect ratio can result in the collapse of the structure [25]. There are other types of polymers that can be also used to fabricate microfluidic devices, like polystyrene, polyvinyl chloride (PVC) and polycarbonate. However PDMS is the most common and was used for work.

Molded PDMS

When mixing the pre-polymer and the curing agent a significant amount of bubbles erupt that need to be dealt with. Vacuum is used in a desiccator to remove the bubbles. The mixture can then be used to cover the mold and after a baking step, the design is transferred to the PDMS as it hardens.

Plasma sealing

Generally this microstructures need to be sealed, usually to a glass or silicon substrate or to another PDMS membrane, using an oxygen plasma treatment. It alters the surface chemistry of the substrates and in the case of PDMS, used in this work, substitutes CH_3 (methyl) groups for OH (hydroxyl) groups creating a hydrophilic surface from a hydrophobic one. For this to happen, the structures are subjected to oxygen plasma where intensity strength and time are variables that depend on the goal intended. Placing the two surfaces in contact with each other, in this case PDMS and PDMS membrane, creates an irreversible bond and the desired structure becomes sealed [32]. Figure 2.13 illustrates the complete process.

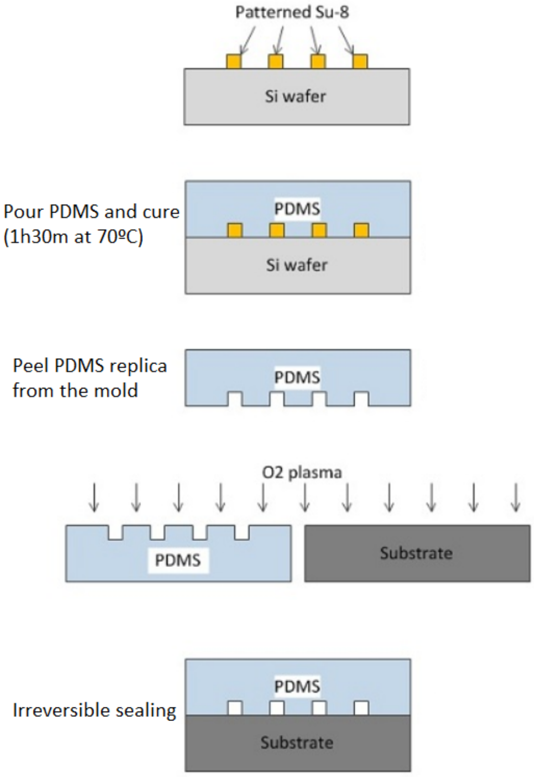

Figure 2.13: PDMS Soft-lithography illustration [33].

2.4 Thesis contribution

This work intends to characterize temperature profiles inside microchannels with multiple configurations (30°, 60°, 90° and 135°), subjected to different volumetric flow rates ($Q_{cold} = 25\mu L/min$, $Q_{cold} = 50\mu L/min$ and $Q_{cold} = 75\mu L/min$) at the cold inlet. The obtained results should help other authors selecting the optimal combination of configuration and volumetric flow rate, that yields the desired temperature at the intended location, fitting a specific work.

Chapter 3

Materials and Methods

In order to perform the experiments needed for this thesis it was necessary to microfabricate heaters and the microfluidic device. In this chapter, the steps that led to the microfabrication at the INESC-MN cleanroom facilities are presented.

3.1 Microfluidics device fabrication

To fabricate a microfluidic device three main processes are needed: hard mask fabrication, mold fabrication and PDMS fluidic structure fabrication.

3.1.1 Hard mask

First the design for the aluminium hard mask over glass was created using a CAD software (AutoCAD). The substrate used for this purpose was a $0.7mm$ thick and $5\times5cm^2$ of *Corning* glass that was previously cleaned. This cleaning process uses isopropanol and DI water to clean the surface and then a ultrasound bath with Alconox, for $30min$ at $65℃$ to remove the remaining dirt. After that, the substrate was rinsed with DI water again to remove the remaining Alconox and it was blow dried to eliminate all water still in the substrate. When the cleaning process was completed, a 1500Å thick $Al_{98.5}Si_{1.0}Cu_{0.5}$ (aluminum) film was deposited on the glass surface, using *Nordiko* 7000 magnetron sputtering system machine (Havant, Hampshire, UK), in the cleanroom at INESC-MN (Figure 3.1).

Figure 3.1: Nordiko 7000 loadlock and terminal for depositing Al

The glass sample with Al was then subjected to a vapor prime pre-treatment and was then transferred to the silicon valley group (SVG) track (Figure 3.2 (a)) at INESC-MN, where it was coated with $1.5\mu m$ of PR (PFR 7790G JSR, Sunnyvale, CA/USA) and then spinned at $500rpm$ for $10s$ to distribute the PR on the surface. The sample was then spinned at $2500rpm$ for $40s$ to obtain an uniform thickness of approximately $1.45\mu m$ and it was then soft baked at $85℃$ for $60s$ to harden.

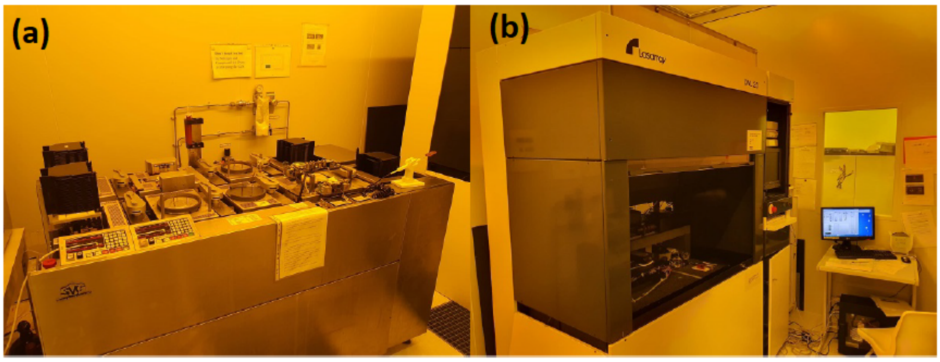

Figure 3.2: SVG track to coat photoresist and develop exposed wafers (a). Direct Write Laser terminal and laser housing is (b).

The CAD design was then transferred to the DWL lithography system (Heidelberg, DE) Figure 3.2 (b) at INESC-MN, where the pattern was photolithographically transfer to the photoresist. After exposure, the sample was transferred back to the SVG track and it was baked at $110℃$ for $60s$ followed by a cooling down period of $30s$. After that, a developer solution (TMA 238 WA) was set to react to the exposed PR for $60s$, followed by a $15s$ rinse with water and spinned for $30s$ to dry. Then an Al wet etching process was performed leading to the removal of exposed Al areas by chemical etching. A close inspection using the microscope was perform to verify if all the CAD file patterns were implemented in the sample (3.3).

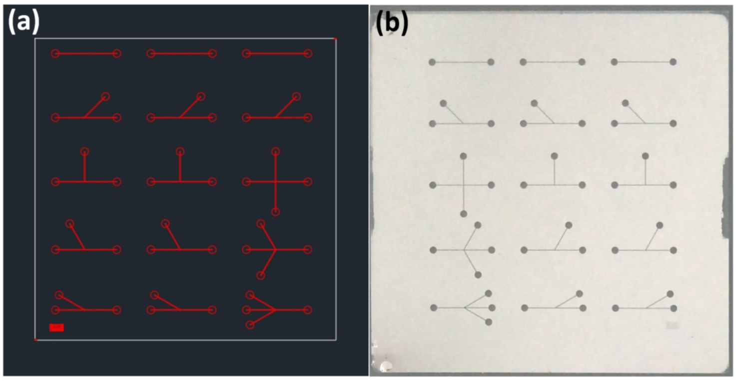

Figure 3.3: (a) *AutoDesk* CAD file; (b) Aluminium on glass hard mask

3.1.2 SU-8 mold

A Si sample of $0.7mm$ thickness and $5 \times 5cm^2$ was cleaned using acetone, IPA solution and DI water in order to remove residues and impurities from the surface. This substrate was then immersed in a heated *Alconox* solution bath at $65℃$ for $15m$, followed by cleaning with DI water and drying with compressed air. At this point the surface cannot have any visible residue. At the PDMS room inside the laminar flow hood, the Si sample dehydrates at $110℃$ for $5m$. SU-8 50 photoresist was then dispensed ($1mL$ for each $2.54cm^2$) and the sample was firstly spin coated for $500rpm$ during $10s$ at an aceleration of $100rpm/s$, and then at $1202rpm$ for $30s$ at $300rpm/s$ to achieve a thickness of $100\mu m$. The coated sample was then pre-baked at $65℃$ for $10min$ and then soft baked at $95℃$ for $30m$. After cooling down, it was exposed to UV light for $99s$ (UV lamp energy $5.95W.cm^{-2}$). After exposure, the sample was baked again at $65℃$ for $1min$ followed by another bake at $95℃$ for $10min$. A PGMEA developer was applied, after cooling down, during $10min$ with strong manual agitation. The resulting mold (Figure 3.4) was then cleaned with IPA and blow dried.

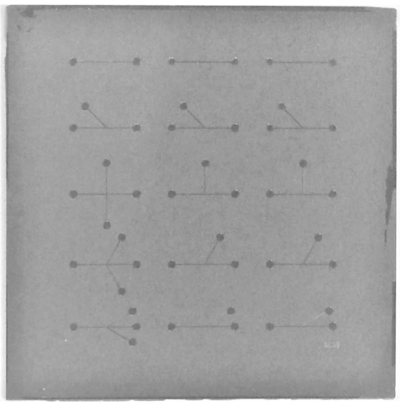

Figure 3.4: Microchannels SU-8 mold.

3.1.3 Molding the inlets, outlets and size of the microfluidic device

A poly(methyl methacrylate) (PMMA) structure needed to be created to hold the poured PDMS into the SU-8 mold. This structure consisted of two separate parts. The top one had the holes for the inlets/outlets of the channels, removing the need to puncture the structure, as well as guiding holes to facilitate the correct alignment with the bottom part. A CAD file containing the location of the holes was converted to machine code and the correct geometry was created using the milling machine (Figure 3.5 (a)).

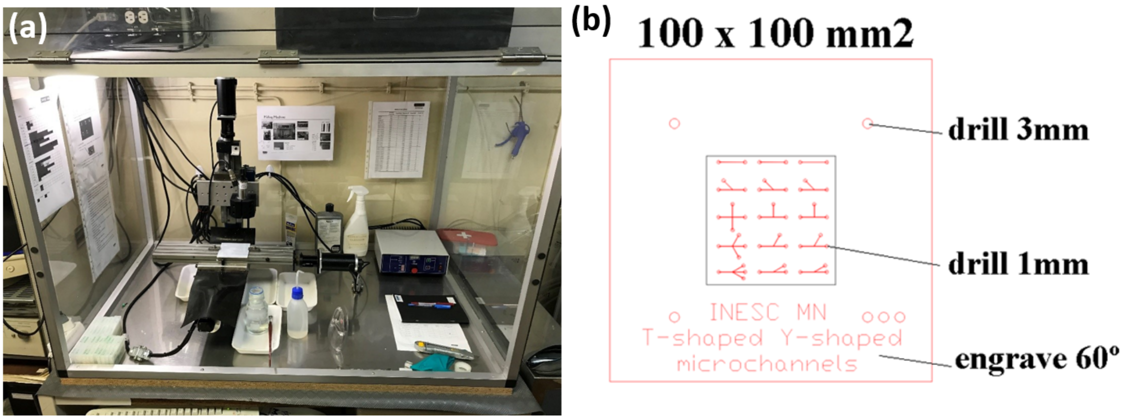

Figure 3.5: (a) Milling machine at INESC-MN; (b) Design for milling thePMMA molds.

INESC-MN logo and project name were engraved on the top mold as well. Both top and bottom parts consisted of two PMMA plates with $100 \times 100mm^2$ and $2mm$ thick with the configuration described and showed in Figure 3.5 (b).

The final result can be observed in Figure 3.6.

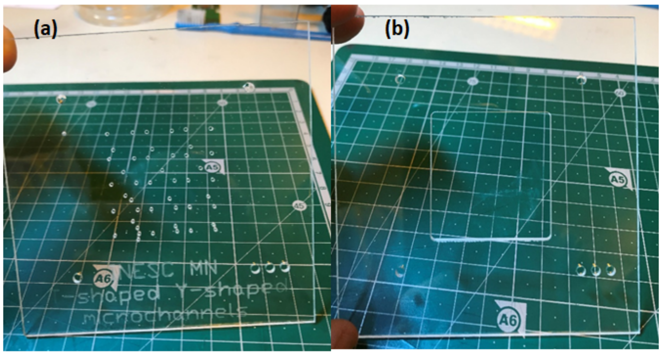

Figure 3.6: (a) Front part of PMMA mold; (b) Bottom part of PMMA mold.

3.1.4 PDMS structures

After the SU-8 mold was manufactured, a PDMS mixture needed to be prepared to manufacture the microchannel patterns. First the PDMS elastomer was produced, for that a mixture of *Liquid Sylgard 184* PDMS (Dow Corning, Midland, MI/USA) and curing agent *KIT* (*Dow Corning*, Midland, MI/USA) in a proportion of $10 : 1$ was prepared using a plastic cup and an analytical scale with $d = 0.0001g$ (*Scientech*, Bradford, MA/USA). The reagents were thoroughly mixed using a spatula and set to rest in a desiccator (*Bel-Art Products*, South Wayre, NJ/USA) for $45min$, to remove bubbles deriving from the mixing process. The SU-8 mold was aligned with the PMMA structures (Figure 3.7 (a)) using Kapton tape, design to hold the mixture.

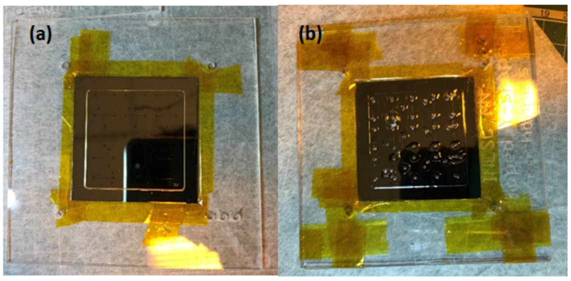

Figure 3.7: (a) PMMA and SU-8 mold; (b) Structure in use.

The PDMS mixture was carefully poured on the SU-8 mold to prevent the occurrence of bubbles. The top part of the PMMA structure, containing the inlet/outlet locations was aligned with the SU-8 mold, as can be observed in Figure 3.7 (b), and the two parts were fixed together using kapton tape. Metal connectors were inserted to mold the inlets and outlets. The structure then bakes in the oven at a temperature of $70^{\circ}C$ for $90min$. After that time, the structure was taken out of the oven and the metal inlets were carefully removed. With the help of a scalper, the PDMS structure was detached from the SU-8 mold. A final visual verification was performed to assure that the geometry was correctly carved into the PDMS and the inlets were in the appropriate locations (Figure 3.8).

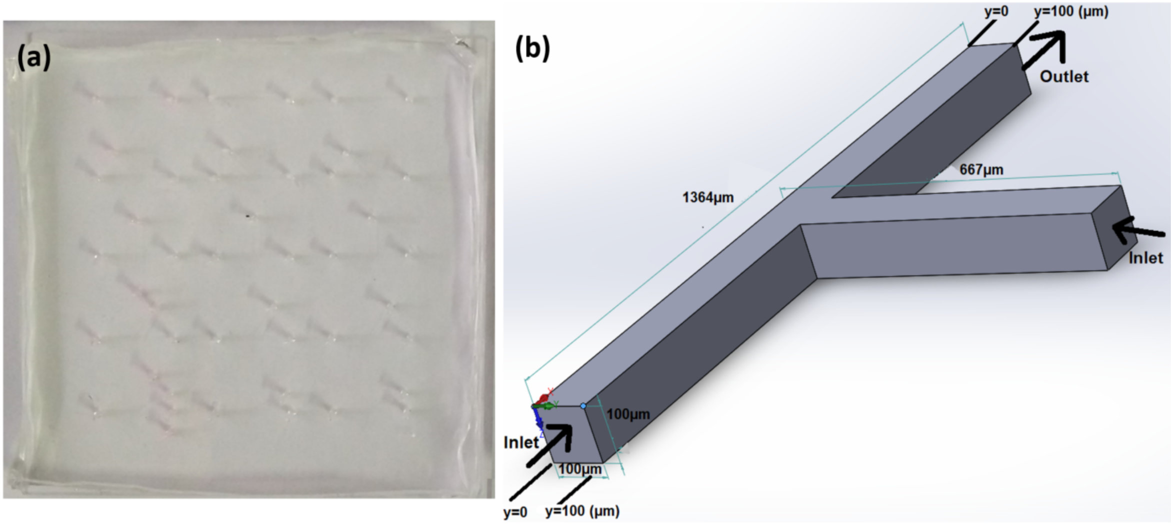

Figure 3.8: (a) PDMS microchannels, (b) Solidworks image displaying the $90^{\circ}C$ (T-shaped) microchannel dimensions.

3.1.5 PDMS Membrane

After removing the PDMS from the SU-8 mold the channels needed to be sealed. For that purpose, a PDMS membrane was fabricated. The same methodology was used for the PDMS mixture. A clean silicon wafer was centered on top of a spinner (*Laurel Corp.*, North Wales, PA/USA) Figure 3.9, placed inside the laminar flow hood (*FASTER-BSC-EN*, Cornaredo, Italy), and a vacuum pump was turned on to restrain its movement. When the PDMS mixture was clear off all bubbles, it was poured onto the center of the silicon wafer and the recipe, already programmed, was selected for the desired membrane height, which in this case was $500\mu m$. The process consists in spin coating at $250rpm$, at acceleration $100rpm.s^{-1}$ for $25s$. After conclusion, the wafer was carefully taken out of the spinner and was baked in the oven at $70^{\circ}C$ for $90min$. The PDMS was then removed from the oven and peeled from the wafer.

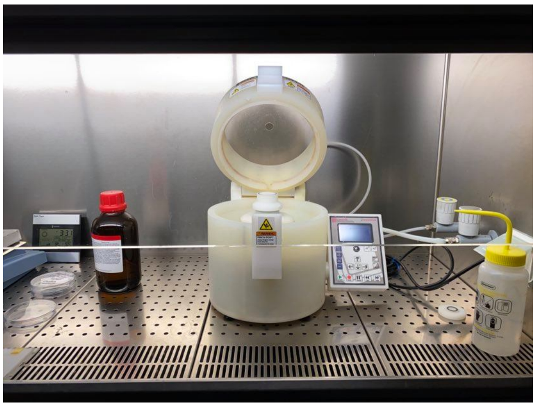

Figure 3.9: Spinner, Laurel Corp.

3.1.6 Oxygen Plasma bonding

With both the molded PDMS and the PDMS membrane produced, the expanded *Oxygen Plasma Cleaner PDC-002-CE* (*Harrick Plasma*, Ithaca, NY/USA) Figure 3.10, was used to irreversibly seal them together. After cutting, with the help of a scalper, the required membrane area, both PDMS mold and the recently cut membrane were inserted into the oxygen plasma machine, with the contact surface for bonding (exposed surface) facing up. Surfaces were exposed to oxygen plasma for $60s$ on $Medium$ intensity ($11W$). After the program finished, both hydrophilic PDMS pieces were quickly aligned face-to-face. To guarantee a correct sealing, the resulting structure was left undisturbed for $24h$.

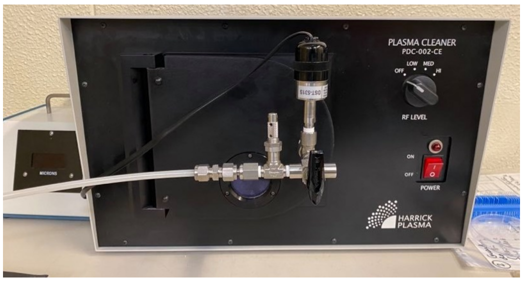

Figure 3.10: Expanded oxygen plasma cleaner PDC-002-CE, Harrick Plasma (Ithaca, NY/USA)

3.2 LIF calibration

To measure the temperature of the fluid inside the microchannels LIF was used. This technique is a non-invasive way to assess temperature and it is very useful when working with microsized channels. For this to work, a calibration was performed *apriori* using RhB, a substance whose fluorescence is temperature dependent, in addition to a setup of thermocouples, allowing to calibrate a curve linking temperature to fluorescence. This curve is then inversed and this data can be used to transform fluorescence (pixel values) in temperature.

3.2.1 Heater fabrication

A micro heater needed to be fabricated in order to perform the calibration experiment. The chosen design, presented in Figure 3.12, was created in *AutoCAD* software. To control the fluid temperature, one thin-film heater was fabricated as follows: a $0.75mm$ thick, $2.54 \times 2.54cm^2$ glass substrate was first cleaned using acetone, IPA solution and DI water. Using the *Nordiko 7000* (Figure 3.1) machine, a 10000Å thick Al film was deposited on the glass surface using a pre-selected program. A vapor prime pre-treatment was then applied to the coated glass for $30min$, before the PR could be dispensed on the surface rotating at $800rpm$ for $5s$, at the SVG track. The substrate was then spinned at $2500rpm$ for $30s$ to obtain an approximately $1.5\mu m$ thick PR layer and it was baked for $85℃$ for $60s$. The sample was then exposed in the DWL machine to transfer the CAD design to the PR. After exposure, the sample was baked again at $110℃$ for $60s$ and, after cooling for $30s$, a developer solution was used during $60s$ to remove the unwanted PR. Then an Al wet etching (TechniEtch Al 80 MOS Aluminium etchant) was performed during $11min$ removing Al from the sample and revealing the heater final design. The sample quality was verified, using the microscope, to guarantee that all the heater features were present. Electric pads were then covered with kapton tape, allowing electrical connection after the process, and a $1.5\mu m$ thick AlOx passivation layer was applied using *UHVII*-magneton sputtering to electrically isolate the heater.

3.2.2 LIF calibration set-up

To be able to perform the calibration of the LIF technique, *Matlab* tools were used, for image analysis, *QuickDAQ*, for thermocouple temperature registration and *Leica Application Suite*, for microscope image acquisition, were used. *ImageJ*, an image processing software and *Microsoft Excel*, for data analysis, were also used for secondary data processing. From the available literature [34], [35], [36], it was possible to replicate the calibration experiment using a *LEICA* noninverted microscope with a 100W mercury short-arc UV lamp, x10 magnification and charge couple device (CCD) camera. With this setup and a micro reservoir fabricated for this purpose it was possible to obtain a calibration curve linking

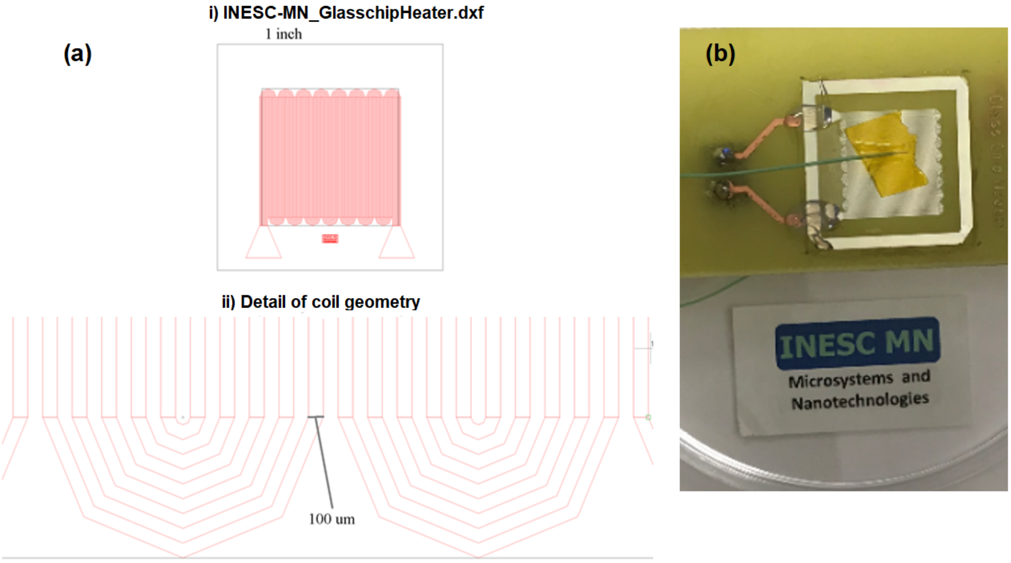

Figure 3.11: (a) Heater design: i) general design ; ii) detail of coil geometry. (b) Thin-film heater

temperature to fluorescence. This curve reflects the behavior of RhB, reducing its fluorescence when temperature increases. With the goal of removing possible experimental errors a normalization was conducted where all the images were normalized by one at room temperature, removing this way the contribution from lamp lifetime, temperature ramp rates and illumination issues. The microreservoir used had a rectangular shape $W(width) \times L(length)$ of $2.5 \times 5mm^2$ and $100\mu m$ height. Two inlets were punctured using $20-Gauge$ rounded syringes tips, (*Instech Laboratories, Inc.*, Plymouth Meeting,PA/USA) adapted to insulin syringes $1mL$ *U-100 Luer-Lock* (*Codan*, Lensahn, DE) and, by connecting tubing adapters *SC20/15*, (*Instech Laboratories*, Inc.Plymouth Meeting, PA/USA) to *Polyethylene BTPE-90 tubing* (*Instech Laboratories*, Inc., Plymouth Meeting, PA/USA) to allow the reservoir to be filled with the RhB solution. This solution was prepared adding 5mg of RhB base with 97% dye content (*Sigma-Aldrich*, USA) to $200mL$ of DI Water which results in a concentration of $25mg/L$. This was suggested by Arromba [34] as the optimal concentration to use since it shows the best temperature sensitivity. After the reservoir was filled, a *K-type Model 5TC-TT-KI-40-1M, PFA* insulated thermocouple (*Omega Engineering, Inc.*, Norwalk, US) was inserted in one of the inlets previously punctured and the reservoir was sealed using silicone to maintain the system hermetically sealed preventing liquid from escaping and/or evaporating. A second thermocouple was used to measure room temperature. The micro reservoir was then attached to a heater, created beforehand, using Kapton tape and it was inserted on the stage of the *LEICA* microscope. To perform the calibration, a correct selection of the microscope filter was needed. For RhB, which has an absorption bandwidth of $554nm$, and after consulting *LEICA* manual, the correct filter was $560/40nm$ capturing images of the emitted fluorescence ($575nm$). Figure 3.12 illustrates the set-up for the calibration experiment.

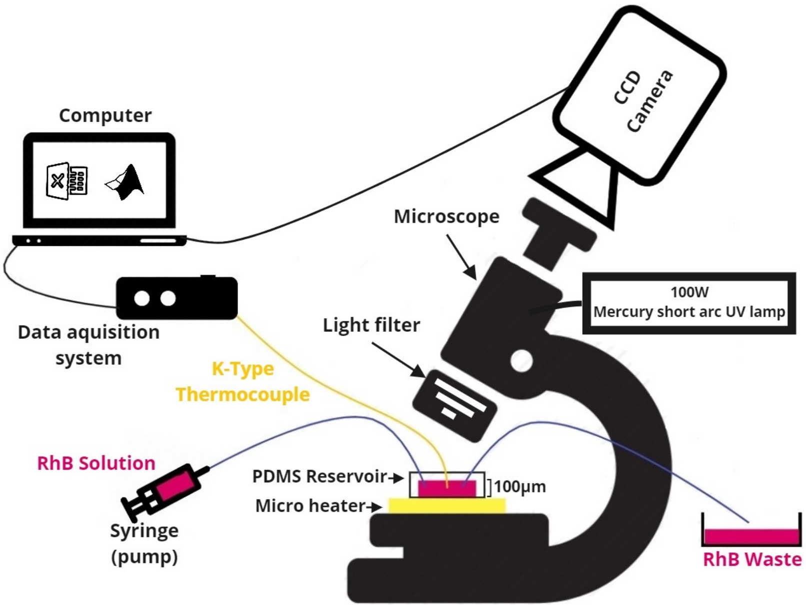

Figure 3.12: Calibration experiment set-up.

With the heater off, an image was taken at room temperature to allow normalization, all images were taken using an exposure time of 50ms. Power delivered to the heater was then increased, resulting in an increase of the temperature inside the reservoir, and images were taken, after temperature stabilized, in steps of approximately $2℃$ from room temperature to $51.5℃$, where the experiment ended due to the appearance of large air bubbles inside the reservoir. This range of temperatures is acceptable to work with in the microchannel experiments. The temperature values were obtained using the *QuickDAQ* software that reads the thermocouple data. The resulting calibration curve can be seen on Figure 3.13.

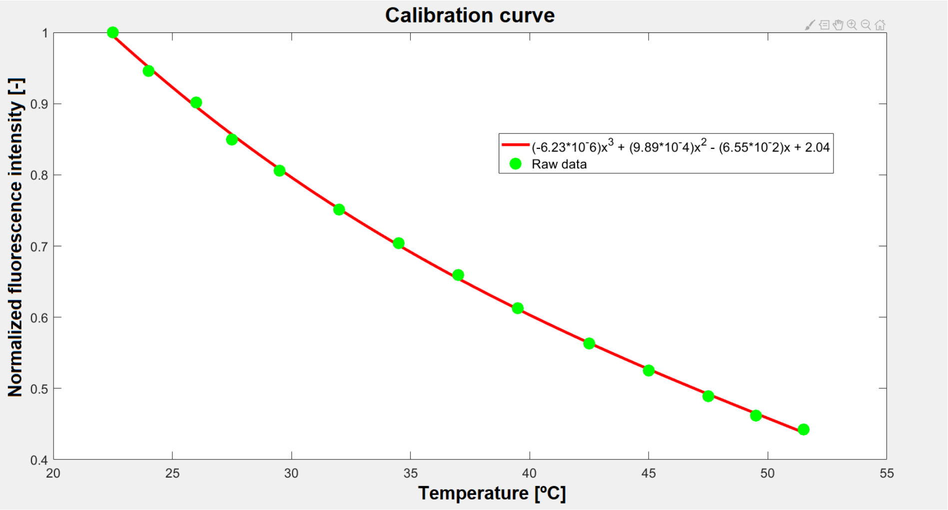

Figure 3.13: Calibration curve of normalized fluorescence intensity vs temperature

The sensitivity [$\%°.C^{-1}$] of the technique is given by the gradient of the fluorescence intensity $\frac{dI}{dT}$ and can be written as a function of image intensity, I_0, as:

$$Sensitivity = \frac{1}{I_0}(\frac{dI}{dT}) \times 100 \tag{3.1}$$

A sensitivity value of 1.92$\%°.C^{-1}$ was obtained for the experimental data in comparison with 1.68 $\%°.C^{-1}$ in the literature [34].

The resulting curve is in agreement with the literature [34] and will be used to asses the temperature of the fluid inside the microchannels in the next chapter.

3.3 Microchannel experiment set-up

3.3.1 Fabrication of copper-clad laminates heater to heat the fluid entering the hot inlet

To perform the microchannel experiments RhB solution needed to be heated in one of the two inlets, creating a difference in temperature at the confluence angle of both channels. This could not be accomplished with the heater used for calibration due to heat losses in the tubing. Due to the system small dimensions and low volumetric flow rates, those heat losses were of the order of 70% and the heated fluid would reach the channel hot inlet almost at room temperature. To tackle this, a small heater was fabricated using a copper-clad laminar sheet (*Pyralux* FR Copper-Clad Laminate). A region of this sheet was laser cuted in such a way that maximize the contact area between the heater and the tube dispensing fluid to the microfluidic device. This heater was placed very close to the inlet of the microfluidic device to further minimize the heat losses, making it possible to pump hot fluid into the microchannel. It works by Joule effect where an electric current is forced to pass through the heater releasing heat. A brief calibration was performed, prior to the experiment, to understand the heater limits and to establish a correlation between power supplied and temperature obtained. Temperature values were obtained using a thermocouple positioned at the microchannel inlets and outlet.

3.3.2 Microchannel experimental set-up

In this experimental work multiple microchannels with different confluence angle configurations, 30°, 60°, 90°, 135° (between inlets) and different (cold) inlet flow rates, $25\mu L/min$, $50\mu L/min$, $75\mu L/min$ were tested. The goal was to understand the influence of angle and volumetric flow rate in the fluid temperature distribution inside the microchannels. To accomplish this the calibration curve was used to determine the temperature values. The set-up for this experiment was similar to the one used for the calibration process (Figure 3.14).

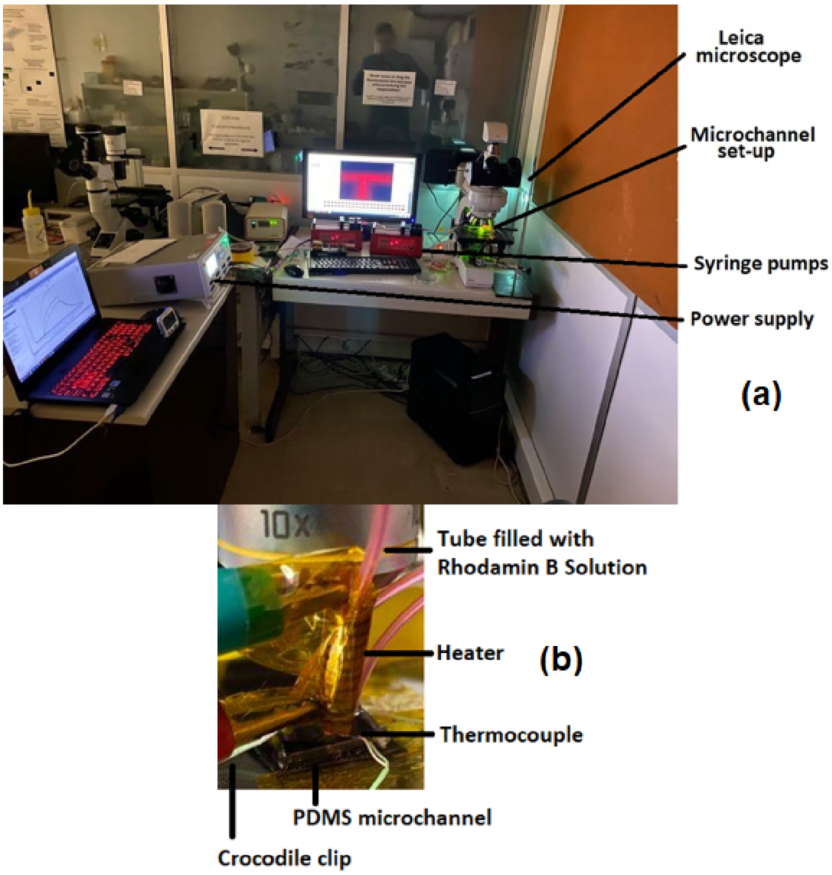

Figure 3.14: Experimental set-up (a). Microchannel set-up (b).

To perform these experiments, the copper-clad heater, that was previously fabricated (subsection 3.3.1), and a variable power source were used to provide the heating, using electric cables with crocodile clips to connect them. To deliver the RhB solution to the microchannel at a constant rate, two syringe pumps were used allowing two independent volumetric flow rates one for each inlet. The RhB solution was carefully collected using insulin $1mL$ syringes and a *SC20/15* tubing adapters were used to connect them to the inlets of the channel. In one of them the heater was attached near the end of the tube (close to the inlet) to provide heating to the fluid flowing inside the microchannel. A third tube was introduced in the outlet to collect the solution. *K-type* thermocouples were placed in the two inlets and in the outlet to obtain fluid temperature values. Using the syringe pump controls, multiple volumetric flow rates could be tested and, by changing the power supplied to the heater, inlet temperature in one of the inlets could be altered. This was tested in the four different microchannel configurations. Three tests were conducted for each squared cross-section area $W(width) \times H(height)$ of $100 \times 100\mu m$ microchannel configurations (Figure 3.15):

- $Q_{cold} = 25\mu L/min; Q_{hot} = 50\mu L/min$
- $Q_{cold} = 50\mu L/min; Q_{hot} = 50\mu L/min$
- $Q_{cold} = 75\mu L/min; Q_{hot} = 50\mu L/min$

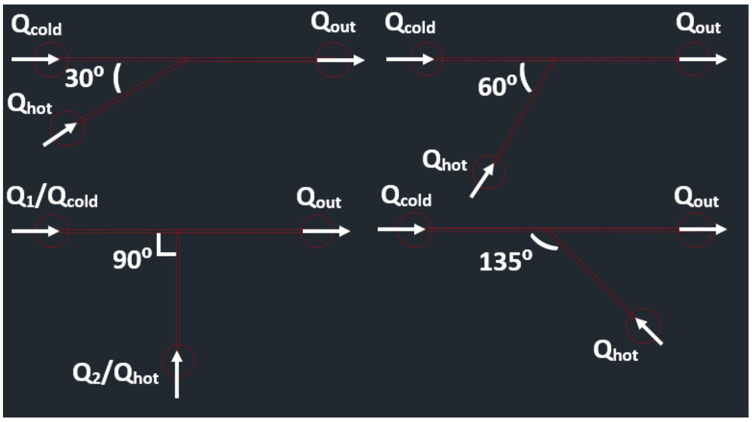

Figure 3.15: Microchannel configurations and flow rates

All the tests were conducted similarly, images were taken $30s$ apart during $24min$. During that time the power supplied by the heater was controlled in three ON/OFF cycles (Figure 3.16).

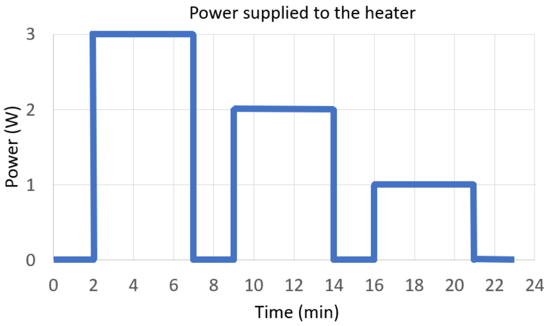

Figure 3.16: Power supplied to the heater for the microchannel experiment

This methodology was applied for every microchannel configuration and volumetric flow rates combination. Figure 3.14 displays the experiment set-up.

3.4 Image processing

3.4.1 Image acquisition (Digital color camera *DFC300FX*)

The images were acquired using an inverted *Leica* microscope equipped with a mercury short-arc $100W$ lamp and utilizing a $\times 10$ magnification lens, 50ms exposure time, $1\times$ gain and a saturation value of 1.

The resulting images had 1392×1040 pixels. The T-shaped (90°) microchannel used to explain the image processing procedure is presented in Figure 3.8.

Multiple images were acquired for different values of power supplied to the heater, which resulted in different temperatures inside the channel. This difference in temperatures is noticeable by different intensity of the pixels (fluorescence).

3.4.2 Image processing

In this subsection the methodology used to process the images obtained for the different flow configurations is described. Figure 3.17 depicts a raw image of the microchannel without any processing.

Figure 3.17: Raw image of a $90°$ microchannel.

To be able to study the flow inside the microchannel, several processing steps were performed as follows:

1. Rotation of the entire image to align the microchannel with x and y axes. This was done using *imrotate* function of *Matlab* (Figure 3.18).

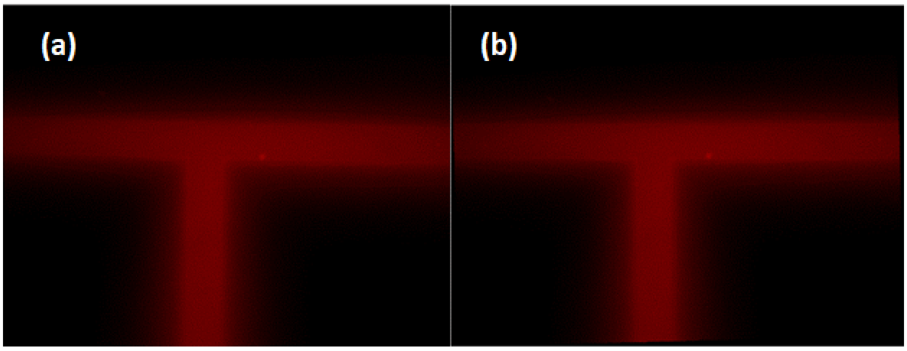

Figure 3.18: (a) Image before rotation; (b) Image after rotation; (here images are enhanced 50% brightness to help visualization).

2. Image conversion to grayscale images using *rgb2gray* function of *Matlab*.

$$Grayimage = 0.2989 \times R + 0.5870 \times G + 0.1140 \times B \tag{3.2}$$

With:

- **R** red channel (matrix) pixel value.
- **G** green channel (matrix) pixel value.
- **B** blue channel (matrix) pixel value

3. First (geometrical) delimitation of channel boundaries using functions *impoly* function of matlab (chooses a region of interest in an image and sets the value of all the remaining pixels intensity to 0 – see Figure 3.19.

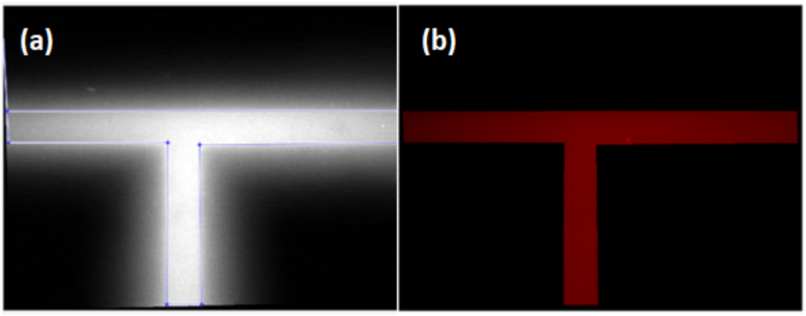

Figure 3.19: (a) Example of *impoly* function. Here image was enhanced using *imadjust* function of *Matlab* to enhance visualization; (b) Resulting image after first *impoly* treatment (here enhanced 50% brightness to help visualization).

4. Overlapping of all images using the first image (Figure 3.20 (a)). This is mandatory for the normalization process since it guarantees that all images are in the same (x,y) position. Custom function *registerImages*, available in the *Matlab* image processing toolbox, was used after calibrating its parameters. This function operates images using similarities between them; in our case the most important parameter is the pixel intensity, but other parameters such as number of iterations, relaxation factor are also used (see Appendix A). After this process, all images were overlapping illustrated in Figure 3.20 (b).

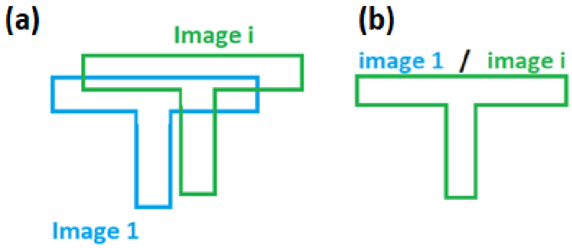

Figure 3.20: Representations of (a) image position before *registerImages*;(b) final result after *registerImages*.

5. Cropping of the images using *imcrop* function of *Matlab* (compelling all images to the same size).

6. Normalization of all images using the first image (*Imagegray*{*i*}/*Imagegray*{*1*}). This means dividing all the images matrix pixel by pixel by the first image at room temperature in the same illumination condition.

7. Calibration Formula application to all images except to *image*{*1*}. This calibration correlation comes from the RhB calibration process (described in subsection 3.2.2). It converts normalized pixel fluorescence intensity in the image to temperature as showed in Figure 3.21.

   $$Temperature\_matrix\{k\} = [\{(80238.0882 \times Normal\_matrix\_double\{k\} - 33689.5598)^2 + 351195434.1159\}^{(\frac{1}{2})} - 80238.0882 \times Normal\_matrix\_double\{k\} + 33689.5598]^{(\frac{1}{3})} - 705.5313/[\{(80238.0882 \times Normal\_matrix\_double\{k\} - 33689.5598)^2 + 351195434.1160\}^{(\frac{1}{2})} - 80238.0882 \times Normal\_matrix\_double\{k\} + 33689.5598]^{(\frac{1}{3})} + 52.8878;$$

   With:

   - $Normal\_matrix\_double\{k\} = Imagegray\{i\}/Imagegray\{1\};$

8. Setting pixels outside the channel to 0 and correcting pixels with spurious intensity values inside the channel. After applying the calibration correlation, some pixels outside the channel exhibited a normalized intensity value different from unity, and that had to be corrected. Inside the channel, on the other hand, there were several regions with noise, due to the presence of impurities (Figure 3.22).

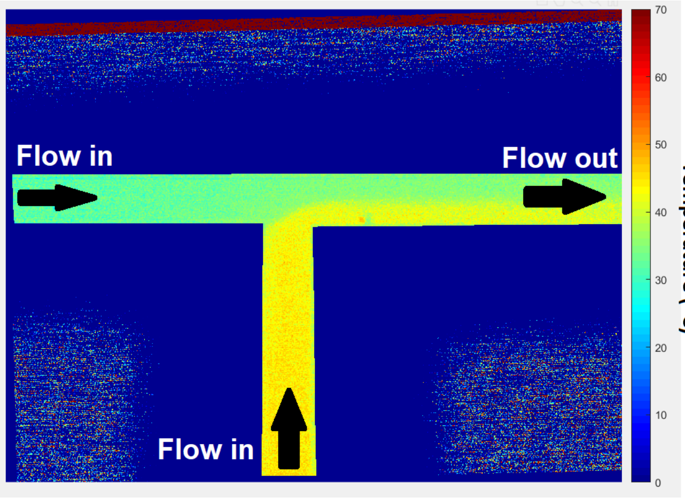

Figure 3.21: Example: $90°$; $Q_{cold} = 50\mu L/min$ $T_{in,cold} = 34℃$; $Q_{hot} = 50\mu L/min$, $T_{in,hot} = 45℃$;$image\{15\}$; $Power = 3W$. Displaying using *colourmap* function of *Matlab*

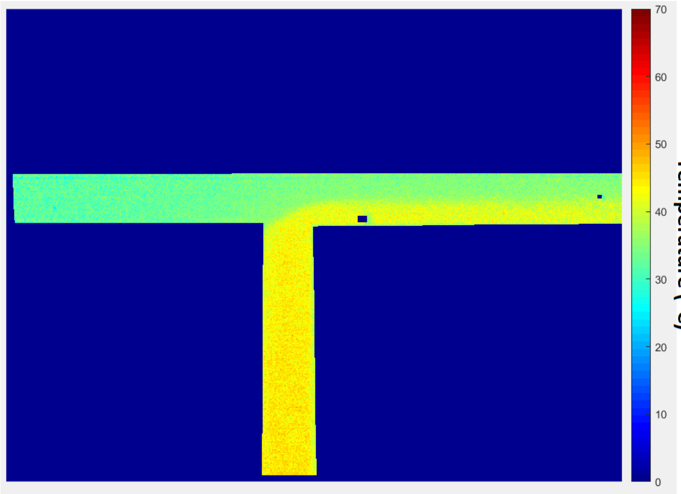

Figure 3.22: Figure 3.21 after corrections.

9. Second (physical) delimitation of the microchannel walls, based on the temperature image, to better define the channel boundaries. This step is needed since the technique used (LIF) has limitations (as any other technique) and it is challenging to accurately define where the physical boundaries are actually located based on images, mainly due to RhB absorption by the PDMS at the walls, enhancing their fluorescence and, therefore, making difficult to differentiate the inside from the outside of the channel. Figure 3.23 illustrates the outcome of this step.

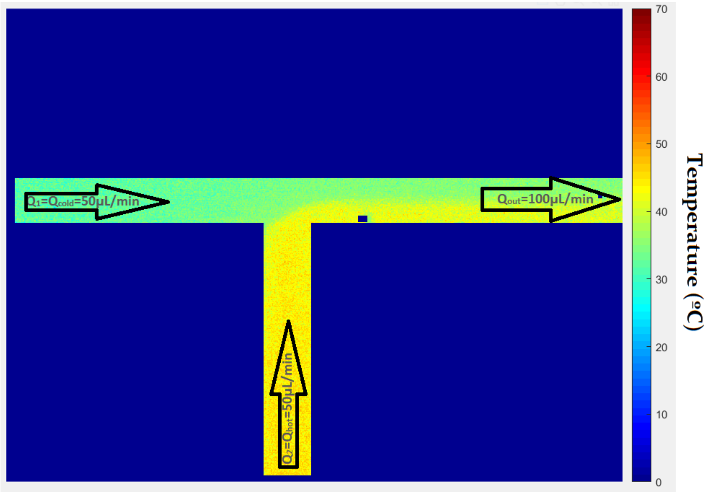

Figure 3.23: Final absolute temperature image.

10. Setting T_{min} and T_{max} of the pixels matrix as reference values. To ensure that a value that appears only once in the image (result of a remaining impurity) is not used, a criterion was adopted to define these quantities. A reference temperature value must exist at least for 20 entries in the entire matrix to be considered. This guarantees that the value selected does not come from a limitation on the technique but from a real temperature value of the fluid.

11. Non-dimensionalization of the temperature field of the fluid.

$$\theta = \frac{(T - T_{min})}{(T_{max} - T_{min})} \tag{3.3}$$

12. Setting values $\theta < 0$ to 0 (Figure 3.24).

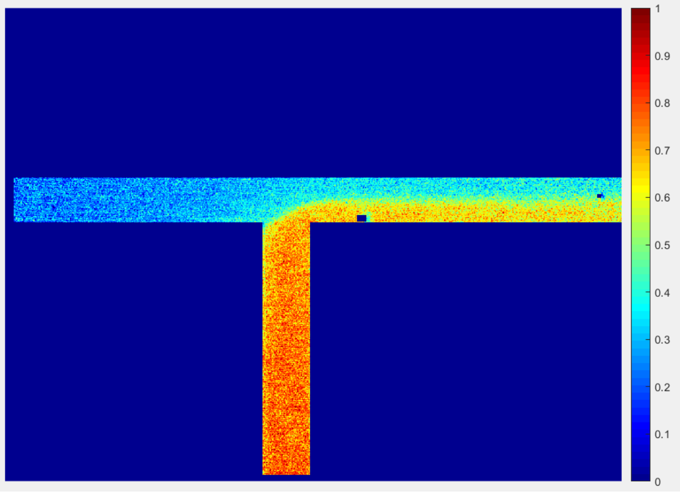

Figure 3.24: Image after non-dimensionalization.

13. Zoom of the confluence region (Figure 3.25).

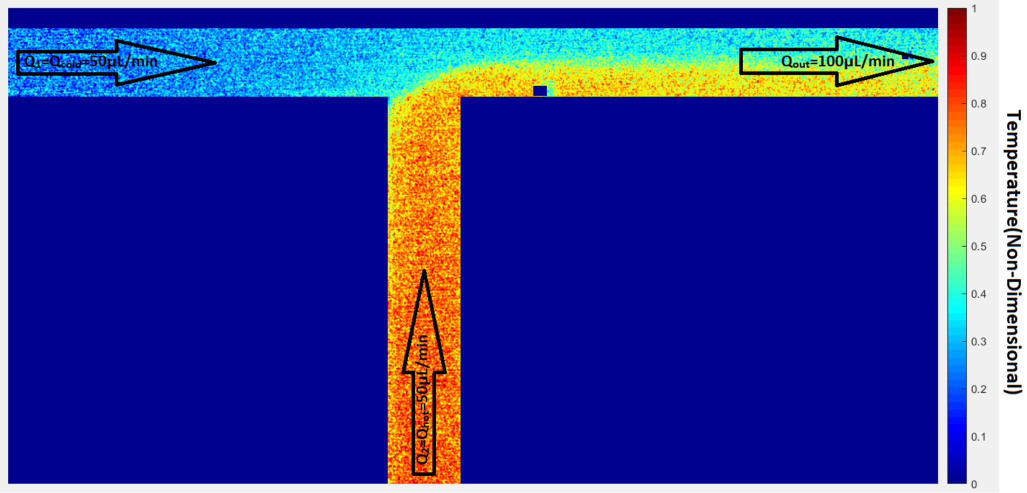

Figure 3.25: Final result, of the image processing, ready for analysis.

The experimental results are presented and discussed in chapter 4.

Chapter 4

Experimental Results and Discussion

4.1 Isothermal flow

To better understand the thermal process developing inside the microchannels, particularly if advection may be relevant, , an isothermal flow analysis was conducted. This gives insight into the phenomena involved when the two streams intersect at the junction region and flow towards the outlet of the channel. The information obtained for this case can then be compared to the non-isothermal case leading to a better overall comprehension of the flow. As displayed in Figure 4.1, at inlet 1, a diluted solution of RhB in water at room temperature, with a concentration of $25mg/L$, was pumped at a volumetric flow rate of $Q_1 = 50\mu L/min$. At inlet 2, in turn, deionized water at room temperature was pumped at the same volumetric flow rate of $Q_2 = 50\mu L/min$. These two fluid streams meet at the microchannel T(90°) junction and flow through to the outlet.

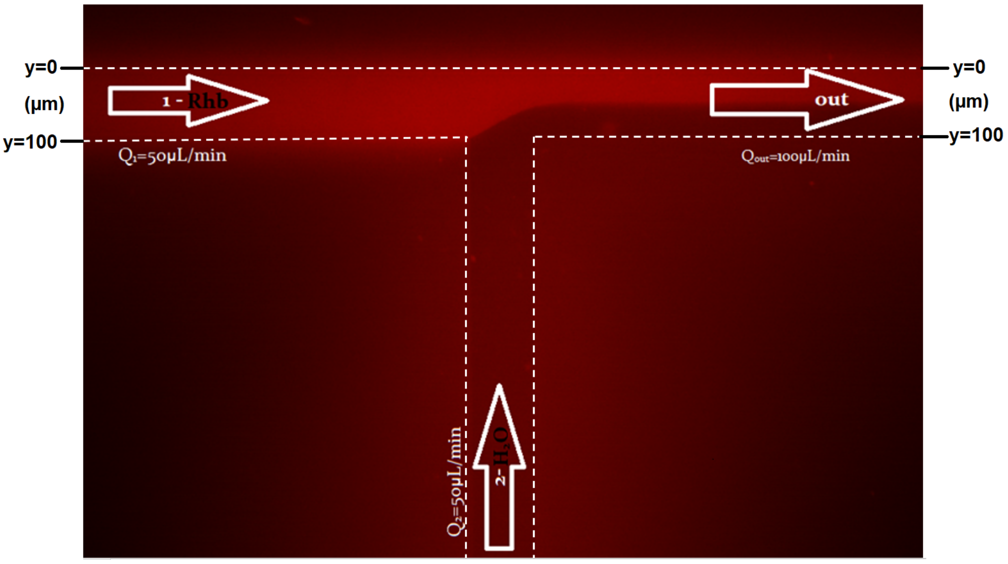

Figure 4.1: $90°$ microchannel raw image. $Q_1 = Q_2 = 50\mu l/min$. Exposure time= $200ms$ (the white dashed lines are added to the image for easier visualization of channel boundaries).

Specific analysis stations at each channel (*a*,*b*, *c*) were selected, as can be seen in Figure 4.2, and the concentration profiles, were plotted using Matlab. The presence of RhB provides the brightness (fluorescence) to the images, which means that the higher the brightness, the greater will be the concentration of RhB. The resulting profiles, which are essentially a mass transport portrait of the mixing flows, might be used to understand the isothermal flow structure, with the respective caution of taking into consideration the differences between momentum transport and mass transport. The profiles shown in Figure 4.2 were made dimensionless using $a_i/max(max(a_i))$, where a_i is a vector with the pixel intensity values in section a_i and $max(max(a_i))$ is the absolute maximum pixel intensity value of all sections (maximum pixel value was obtained for section a_1). Normalized results should be between 0 and 1.

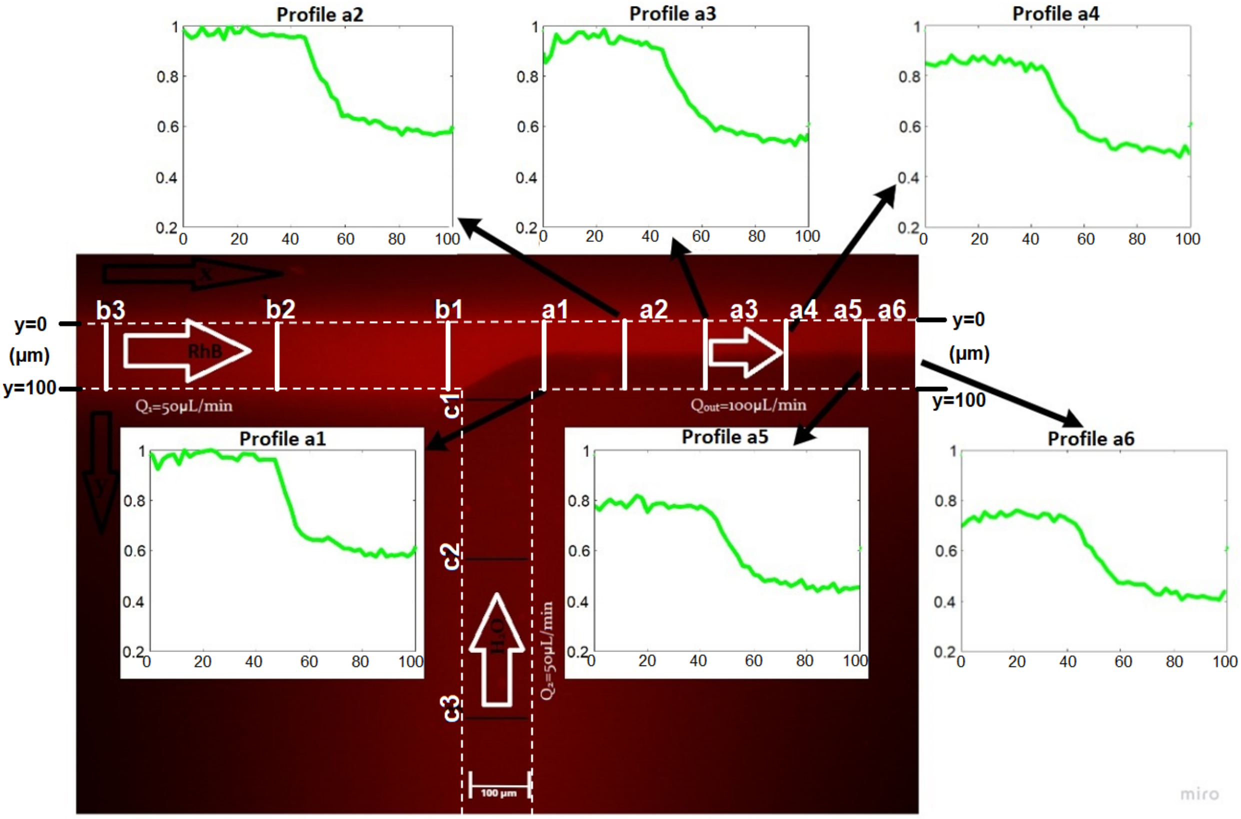

Figure 4.2: Sections of analysis and "mass concentration" profiles for $\mathbf{a_i/max(max(a_i))}$.

As can be observed in Figure 4.3, there is a vertical shift in the curves towards lower values. This shift can be explained by an illumination problem that results in pixel intensity value reduction as sections are defined further downstream the center of the image, where the light source is more intense. This means that section *a1* will have overall higher pixel values than the subsequent sections. It can also be noticed that, the maximum normalized pixel intensity remains constant in all sections, meaning that the difference between the maximum value on the graph and the minimum remain the same for every section, which suggests that mixing is poor as a consequence of having virtually no advection. However, the slope that clearly distinguishes the two zones, high and low normalized pixel values, gets smaller between subsequent sections, which indicates that the mixing is occurring locally by diffusion.

In *a1* mixing only occurs in approximately 10% of the channel width (direction perpendicular to the flow direction), while in *a6* this mixing zone is present in around 20%, as illustrated in Figure 4.3. This behavior suggests that for much longer outlet channels, and with more sections analyzed, this mixing zone would increase until eventually the the mixing would be complete. Therefore, it can be extrapolated that the gap between maximum and minimum normalized pixel intensity values would become smaller and, having the sufficient channel length in the flow direction to promote mixing, this difference would be zero at some finite length value.

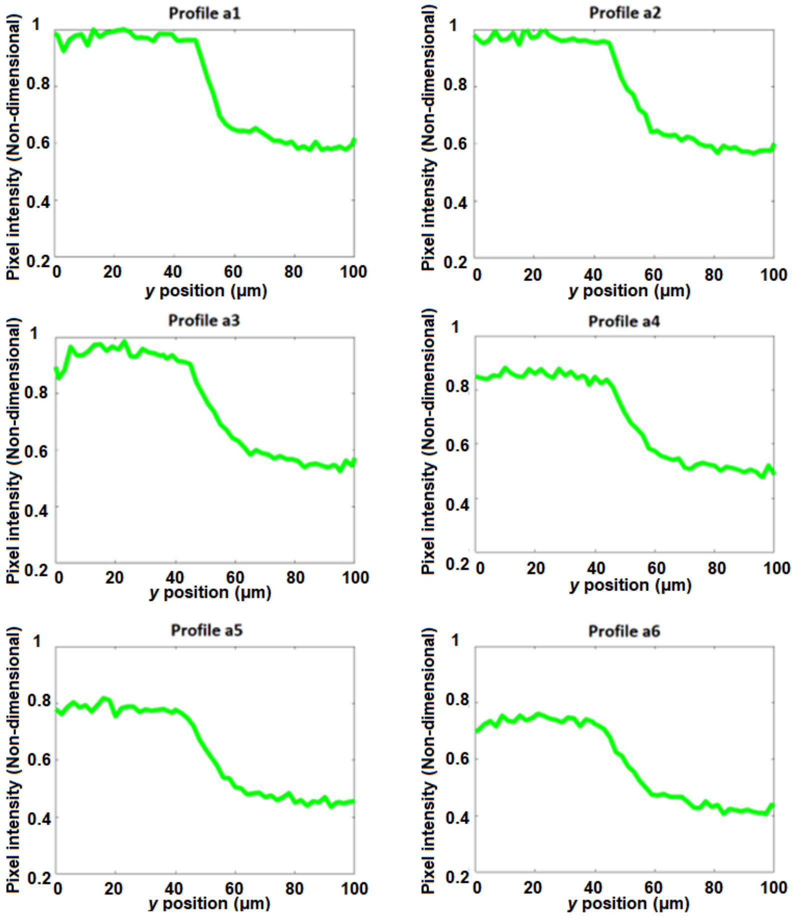

Figure 4.3: Pixel intensity profiles at different sections.

4.1.1 Flow analysis

Since the system (mass flow rate of H_2O and RhB solution) was left running for a couple of minutes before the pictures were acquired, it is acceptable to assume that it has reached the steady state conditions.

4.1.1.A Reynolds number

It is important to evaluate the Reynolds number to have a better understanding of the flow in this problem. The Reynolds number can be defined defined as expressed by (4.1):

$$Re = \frac{\rho u D}{\mu} = \frac{u D_H}{\nu} = \frac{\dot{Q} D_H}{\nu A} \tag{4.1}$$

$$D_H = \frac{4A}{P} \tag{4.2}$$

Where:

- ρ is the density of the fluid (kg/m^3)
- $\mathbf{u}$ is the flow average velocity (m/s)
- $\dot{\mathbf{Q}}$ is the volumetric flow rate (m^3/s)
- $\mathbf{D_H}$ is the hydraulic diameter of the microchannel (m)
- μ is the dynamic viscosity of the fluid $(Pa \cdot s)$
- ν is the kinematic viscosity of the fluid (m^2/s)
- A is the microchannel cross-section area (m^2)
- P is the wetted perimeter (m)

For this case:

- $Q_1 = Q_2 = 50\mu L/min = 0.833(3) \times 10^{-9} m^3/s$
- $Q_{out} = 100\mu L/min = 1.6666(667) \times 10^{-9} m^3/s$
- $A = 100\mu m \times 100\mu m = 10^{-8} m^2$
- $P = 100\mu m \times 2 + 100\mu m \times 2 = 4 \times 10^{-4} m$
- $D_H = \frac{4 \times 10^{-8}}{4 \times 10^{-4}} = 10^{-4} m$
- $v \approx V_{H_2O(20℃)} = 1.004 \times 10^{-6} m^2/s$ [1]

INLETS $Re_1 = Re_2 = \frac{0.833 \times 10^{-9} \times 10^{-4}}{1.004 \times 10^{-6} \times 10^{-8}} = 8.3$

OUTLET $Re_{out} = 16.6$

---

[1] RhB solution concentration very small ($C_{RhB} = 25mg/L$) which makes $v_{solution} \approx v_{H_2O}(20℃)$ a good estimate.

Since $Re = 16.6$, which is not much greater than 1, it is expected that the flow is always laminar. This type of flow does not provide good mixing since each fluid layer moves smoothly past the adjacent layer with little (only diffusive heat transfer) or no mixing. Turbulent flow, in turn, promotes mixing, due to the random fluctuations of the flow field parameters. Turbulent eddies, which are characteristic of turbulent flows, have a major role in the mixing process. In laminar flows, vortices can be generated (e.g., the von-Karman street of flows past bluff bodies), but their deterministic nature limits the mixing potential, when compared with turbulence. With Reynolds numbers, slightly above 1, inertial forces dominate over viscous forces. However, advection seems to occur almost exclusively in the main flow direction, whereas diffusion is mainly transversal to the flow direction, which is the preferential mixing direction.This can be noticed in the present study by the lack of disruption on the fluids interface and some penetration of one fluid to the other fluid stream, like that be observed by Calado et al. [37] for example (Figure 4.4). Moreover, these Reynolds numbers values mean that the diffusion characteristic time (which can be defined as L^2/v) is much larger than that of advection (which can be defined as L/u). Hence, a fluid element entering the outlet channel will be conveyed by advection to the outlet earlier than the time required for the diffusion momentum exchange to occur is attained.

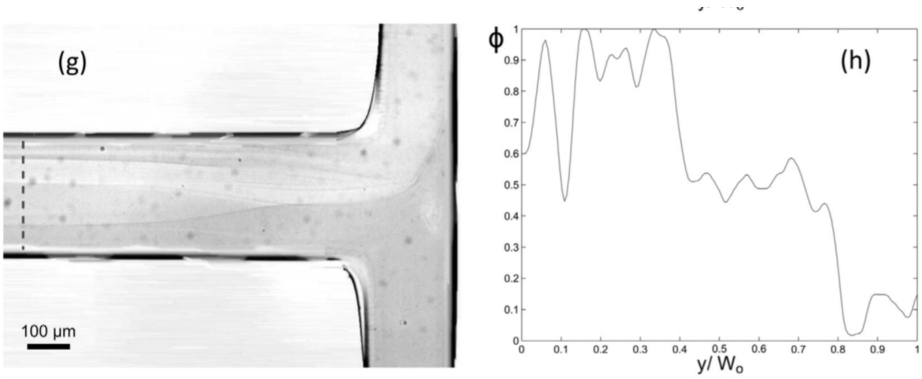

Figure 4.4: Illustrative examples of the flow pattern and concentration profile at the mixing channel in a T-shaped micromixer. (g) flow pattern for regime V ($Re_0 = 305$); (h) concentration profile for regime V ($Re_0 = 305$) [37]

.

4.1.1.B Schmidt number

To be adequate the use of mass transport images for the flow analysis, the Schmidt number must be calculated. This dimensionless parameter provides the relative magnitude of the momentum diffusivity (kinematic viscosity) and the mass diffusivity. The Schmidt number is defined as expressed by (4.3):

$$Sc = \frac{\nu}{D} = \frac{\mu}{\rho D} \tag{4.3}$$

Where $\mathbf{D}$ is the mass diffusivity (m^2/s).

RhB mass diffusivity in water [38] (21.5℃):

$$D = 3.6 \times 10^{-10}(m^2/s)$$

However, since the solution is very diluted, that is, it contains RhB in a very small concentration $(25mg/L)$, this becomes in practice a water self-diffusion problem. The water self-diffusion coefficient (25℃) [39] is $D = 2.57 \times 10^{-9}(m^2/s)$ and the water kinematic viscosity (25℃) [39] is $v_{H_2O} = 0.9225 \times 10^{-6}(m^2/s)$.

Hence, for this case, $Sc = 359$. The momentum diffusion (molecular viscous transport) dominates over the mass diffusion. This means that the characteristic mass diffusion time (that can be defined as L^2/D) is much larger than that of characteristic momentum diffusion time (that can be defined as L^2/v). Hence, as seen above, a fluid element entering the outlet channel will be conveyed by advection to the outlet prior to momentum diffusion to occur completely and, as just seen, even much earlier than the time available for mass diffusion to occur. Taking this into account, it is acceptable to use the mass transport images acquired as an indicator of the flow field structure (momentum transport). It is known that the very slow diffusion process of mass is *ca.* 400 times slower than that of momentum. But, and more important than this, it is known that advection in the main flow direction dominates (over diffusion) for both momentum and mass transport. This can be understood by looking at mass Peclet number. This non dimensional number yields the ratio between the rate of mass transferred by advection by the one being transferred by diffusion and is defined as expressed by (4.4):

$$Pe = \frac{D_H u}{D} = \frac{\dot{Q} D_H}{AD} = ReSc \tag{4.4}$$

In the case $(Q_1 + Q_2 = Q_{out} = 100\mu L/min)$, the value obtained $Pe = 6480$ confirms that advection in the main flow dominates over diffusion. Observing Figure 4.1, one can realize that a segregated flow (without transversal advection and a pale transversal diffusion) occurs in the outlet channel: there is a clear separation between the fluids and the steep gradients occurring at the fluids interface denote that mass transfer is very slow (Figure 4.3). Nevertheless, as can be seen in those figures, the RhB intensity decreases as the fluid moves downstream to the outlet (for successive stations) indicating that mass mixing is slowly occurring by diffusion (Figure 4.5).

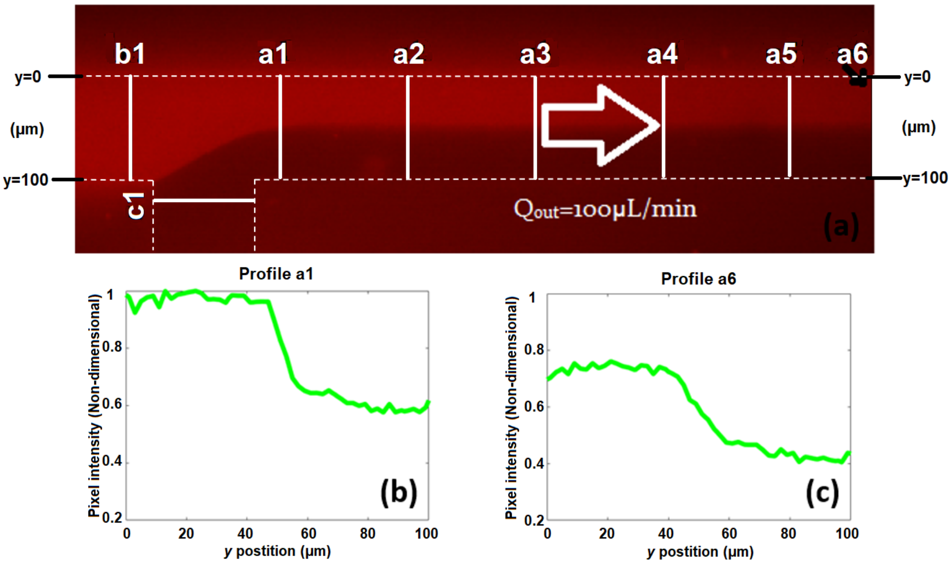

Figure 4.5: Illustrative example of the flow pattern and sections of analysis and concentration profiles at the mixing channel in a T-shaped micromixer. (a) flow pattern for $Q_{out} = 100 \mu L/min$ $(Re_{out} = 16.6)$; (b) concentration profile for section *a1*; (c) concentration profile for section *a6*

4.1.1.C Velocity profile

Figure 4.6 illustrates the velocity profiles parallel to the flow direction (x).

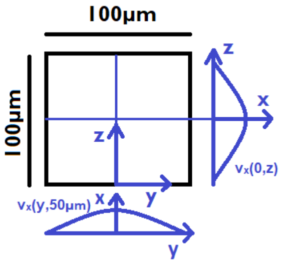

Figure 4.6: Velocity profile representation.

For laminar flow, the hydrodynamic length may be obtain from (4.5):

$$(\frac{x_{fd,h}}{D_H})_{lam} \approx 0.05 Re_{D_H} \tag{4.5}$$

Where:

- $x_{fd,h}$ is the hydrodynamic entry length (m).

$(\frac{x_{fd,h}}{D_H})_{lam} \approx 0.021$ meaning that the flow is fully developed $2.1 \mu m$ from the inlet. The images are taken in the intersection, at 3.4 mm from the inlets. Hence it is assumed that the flow is hydrodynamically fully developed as it reaches the intersection.

The laminar, fully developed flow in a rectangular channel exhibits a velocity profile $u(y,z)$ expressed by (4.6) [40].

$$u(y,z) = \frac{48Q}{\pi^3 WH}\left[\frac{\sum_{n,odd}^{\infty}\frac{1}{n^3}\left[1-\frac{\cosh(n\pi\frac{y}{H})}{\cosh(n\pi\frac{W}{2H})}\right]\sin(n\pi\frac{z}{H})}{1-\sum_{n,odd}^{\infty}\frac{192H}{n^5\pi^5 W}tanh(n\pi\frac{W}{2H})}\right] \tag{4.6}$$

Where:

- u is the velocity in the main flow direction x along the channel length L (m).
- y is the transverse direction along the channel width W (m).
- z is the vertical direction along the channel height H (m).

In this work $W = H = 100\mu m$, $-50\mu m \leq y \leq 50\mu m$, $0\mu m \leq z \leq 100\mu m$. Velocity profiles will be evaluated at $z = z_1 = 50\mu m$ (z centered). For $Q_1 = Q_{in1} = 50\mu L/min$ and $Q_2 = Q_{in2} = 50\mu L/min$, the average velocity at both inlet channels is:

$$U_{mean} = \frac{Q}{A} = 0.0833(m/s) \tag{4.7}$$

As for $Q_{out} = 100\mu l/min$, $U_{mean} = 0.0833(m/s)$. Using 4.6, the velocity profiles are presented for both volumetric flow rates (Figure 4.7).

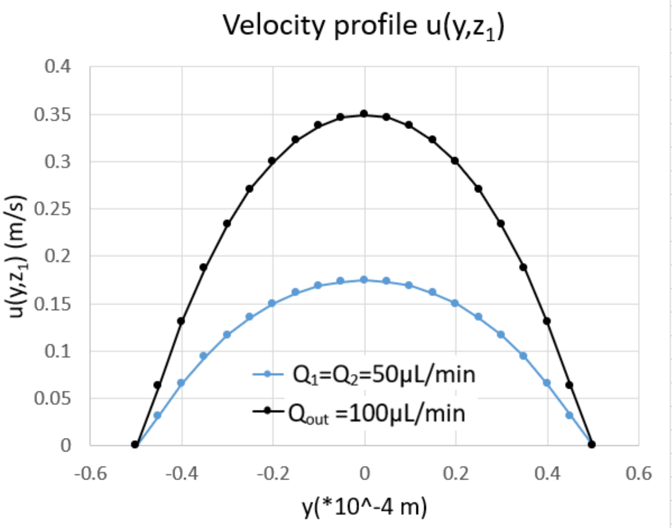

Figure 4.7: $u(y,z_1)$ velocity profile for $Q_1 = Q_2 = 50\mu l/min$ and $Q_{out} = 100\mu l/min$.

Since both fluids are DI water, RhB concentration is very small and does not affect the fluid properties, and momentum is much greater than mass diffusion, it is expected that the two different streams (Q_1 and Q_2) will rapidly evolve to a completely developed flow (Q_{out}) resulting in a symmetrical (y axis) velocity profile showed in Figure 4.7.

4.1.1.D Mass mixing

Mass diffusion occurs in the outlet channel where $Q = 100\mu l/min$ and $U_{mean} = 0.166m/s$. Bothe et al. [41], studied multiple flow velocities to evaluate the mixing quality in a T shaped microchannel with dimensions similar to those of this work. In order to assess the mixing quality (4.8) was used (based on *Danckwert's* intensity of segregation):

$$I_S = \frac{\sigma^2}{\sigma^2_{max}} \text{ with } \sigma^2 = \frac{1}{|V|}\int_V (c-\bar{c})^2 dV \tag{4.8}$$

With:

- $\bar{c}$ is the mean value of the concentration field c.
- σ^2_{max} is the maximum possible variance.

Given by $\sigma^2_{max} = \bar{x}_a(1-\bar{x}_a)$ where $\bar{x}_a$ is the average molar fraction. Another useful quantity is the intensity of mixing (I_M) and it is defined by (4.9):

$$I_M = 1 - \sqrt{I_S} = 1 - \frac{\sigma}{\sigma_{max}} \tag{4.9}$$

The values of I_S are between 0 and 1 (normalized), meaning that for a value of 0 the system is completely segregated and for a value of 1 the system is homogeneously mixed. Flow regimes for different *Reynolds* numbers were tested and presented on the work of Bothel et al. [41], for $U_{mean} = 0.01m/s$ and $0.9m/s$, and the results shown in Figure 4.8 were obtained.

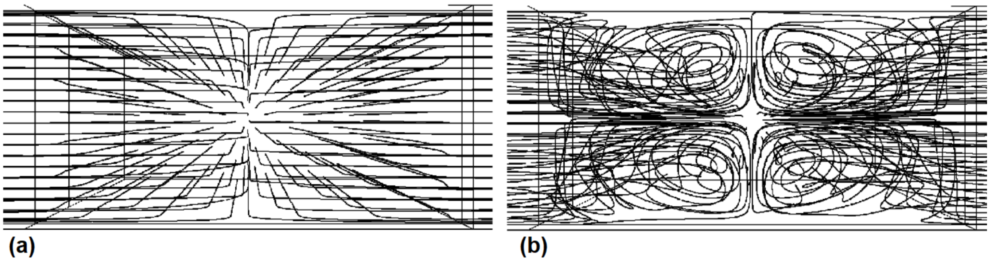

Figure 4.8: Path lines at the entrance of the mixing channel for average flow of (a)$0.01m/s$ and (b) $0.9m/s$ [41].

As can be observed, for the present work where $U_{mean} = 0.166 m/s$, it is expected that path lines are similar to the ones illustrated in Figure 4.8 (a), where two different fluids flow side by side in a flow structure consisting of two completely segregated regions. The same work uses tracer profiles to evaluate the degree of the mixing. For $U_{mean} = 0.9 m/s$, the maximum velocity, mixing is still very poor, and the intensity of mixing is almost zero, as clearly shown in Figure 4.9. In fact, a clear separation between the two fluid flows, with a quite well defined interface, can be seen in the figure.

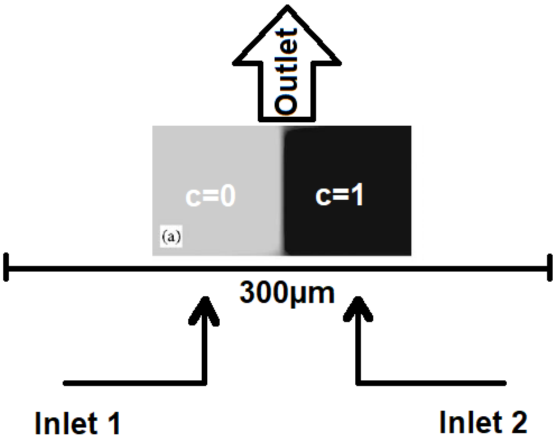

Figure 4.9: Tracer profiles on the cross section of the mixing channel $300\mu m$ for $U_{mean} = 0.9 m/s$ [41].

For the present work, since U_{mean} is even smaller, it is expected that the mixing is even lower – see Figure 4.10.

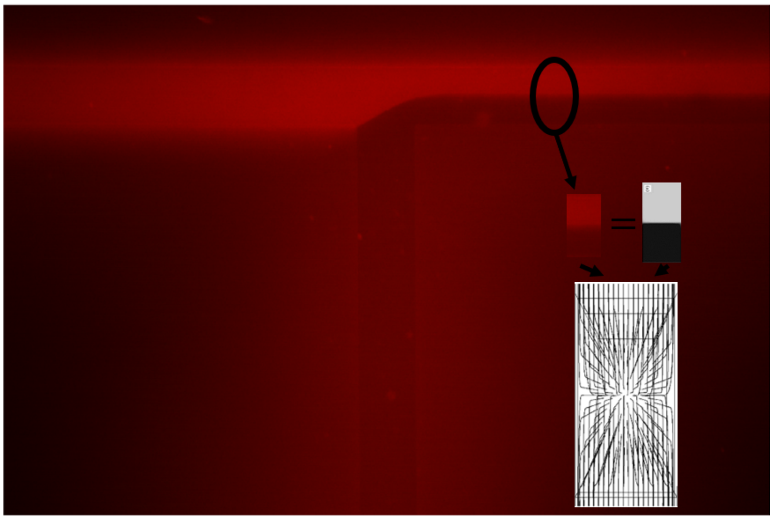

Figure 4.10: Comparison between current work and [41].

For greater velocities – see Figure 4.11 – instabilities of the Kelvin-Helmholtz type appear, giving birth to the formation of vortices, greatly enhancing mixing.

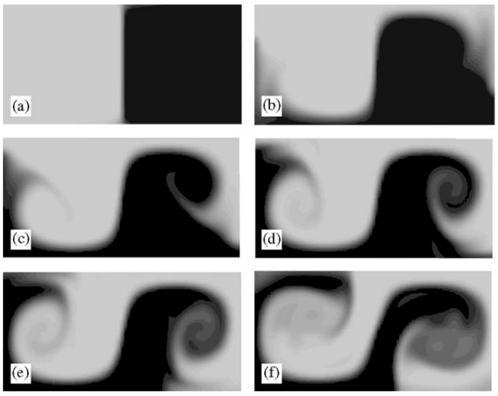

Figure 4.11: Tracer profiles on the cross section of the mixing channel $300\mu m$ behind its entrance for mean velocities of (a) $0.9m/s$, (b) $1.05m/s$, (c) $1.1m/s$, (d) $1.15m/s$, (e) $1.20m/s$ and (f) $1.4m/s$ [41].

4.1.1.E Diffusivity

Diffusivity, mass diffusivity or diffusion coefficient is a proportionality constant between the molar flux due to molecular diffusion and the gradient in the concentration of the species (or the driving force for mass diffusion). Diffusivity characterizes the *Fick's* law, expressed as (4.10).

$$J = -D\frac{d\varphi}{dx} \tag{4.10}$$

Where:

- J is the mass diffusion flux measuring the amount of a species that will cross a unit area during a unit time interval.
- φ (for ideal mixtures) is the species concentration
- x is the direction of the diffusion flux.

For the present work, $\frac{d\varphi}{dx}$ is not a simple task to estimate, making the calculation of J difficult to accomplish. Nevertheless, this diffusion flux, when obtained, is a strong tool to assess the technique limitations. In fact, RhB appears to diffuse to the porous PDMS walls by diffusion, accumulating there and making the walls definition, in the acquired images, and the calculation of the temperatures values close to those walls a challenge. In the work of Abate et al. [42], the authors demonstrate the RhB diffusion to the PDMS walls, as can be observed in Figure 4.12. The authors presented the difference between a uncoated and coatedd PDMS microchannels with squared cross section, the latter to prevent RhB diffusion to the PDMS walls.

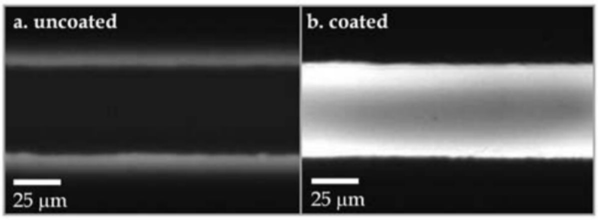

Figure 4.12: Comparison of diffusion of RhB into (a) uncoated PDMS channel, in which it has diffused into the PDMS walls, and (b) coated PDMS channels, in which it has been prevented form diffusing into the PDMS walls. [42].

Glawdel and co-workers [43], the fast diffusion process of RhB to the PDMS walls by testing the photobleaching of absorbed RhB, with the goal of improving temperature measurements. Photobleaching is a destructive process where the fluorophore loses the ability to emit light under prolonged exposure to excitation. This is very helpful in reducing the effect of extra fluorescence emitted by RhB accumulated at the PDMS walls – see severe accumulation of RhB in Figure 4.13 (a). With photobleaching (see images in Figure 4.13 b), a significant reduction in light intensity is observed with increasing time and, after $30min$ of photobleaching, the only signal acquired is due to the RhB in the fluid.

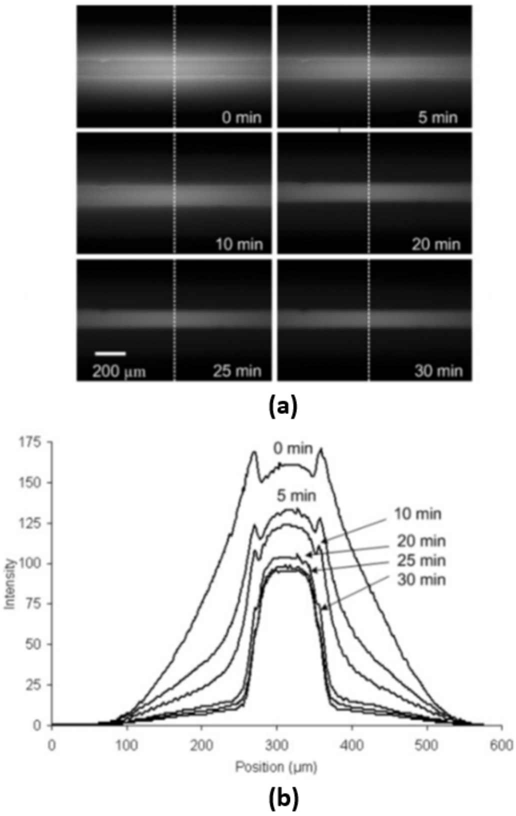

Figure 4.13: (a) Sequence of fluorescent images acquired during the course of photobleaching a PDMS microchannel with a $100\mu m$(solution of RhB pumped at $20\mu L/min$. (b) Corresponding light intensity profiles showing the decrease in signal from absorbed RhB [43].

This photobleaching technique was then applied by the authors to a non-isothermal flow mixing case in a Y-shaped mixer, where a hot fluid is admitted from the left and cold fluid from the right inlets, mixing in a third branch and flowing then in the outlet channel (Figure 4.14 and Figure 4.15).

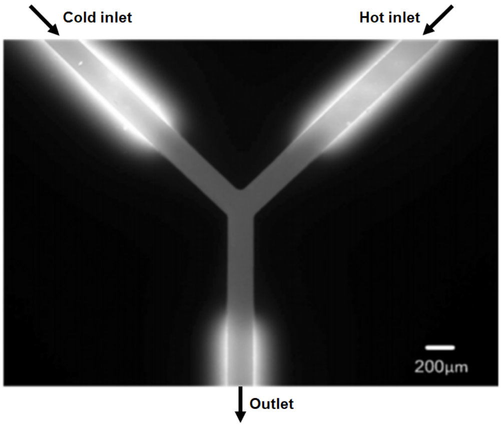

Figure 4.14: Wide view (10x) of the intersection taken after the photobleaching experiment. The hot stream on the left-hand side causes a larger amount of absorption than the cold stream on the right [43].

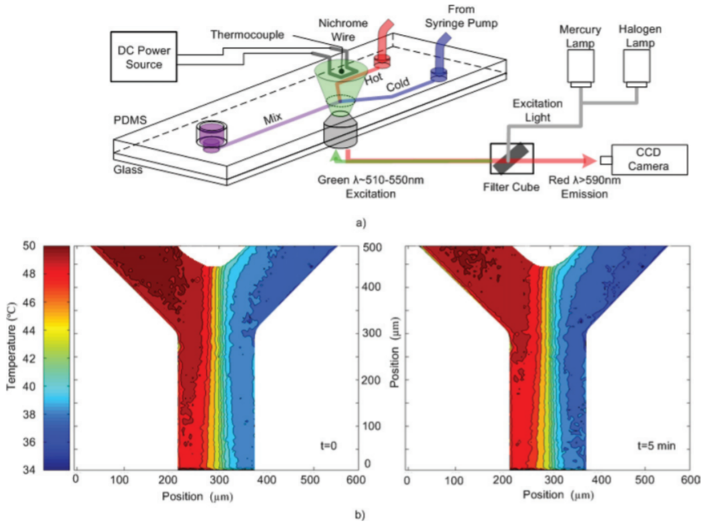

Figure 4.15: (a) Schematic of the experimental setup of the Y-channel PDMS chip. (b) Temperature contour plots of the intersection obtained from two images taken $5min$ apart while applying the photobleaching technique to prepare the area for fluorescent based thermometry [43].

The method presented by Glawdel et al, reduces the errors between the left and right images in Figure 4.15 (b), which were taken 5 min apart, since it greatly reduces the emission contribution of the absorbed RhB at the PDMS walls, which would result in misleading temperature values in the acquired images. In this thesis, RhB diffusion to the PDMS walls affected the outcome of this experiment and this will be discussed in chapter 5.

4.2 Isothermal vs non-isothermal flow

After studying what happens in an isothermal flow, the non-isothermal case can be introduced. To perform the non-isothermal experiment both inlets 1 and 2 are pumped with RhB solution $(25mg/L)$ with the first remaining at room temperature while the latter is heated before entering the microchannel. The maximum power of $3W$ used in the experiments was selected since it was the one that delivered the clearest results. For the temperature dependent case, change in a pixel intensity will not occur due to a difference in solution concentration, like in the isothermal experiment, but due to a temperature difference that governs the emission properties of RhB. For this analysis, a comparison is made between intensity of light in Figure 4.16 (a), which is linked to RhB mass concentration, and the dimensionless temperature showed in Figure 4.16 (b).

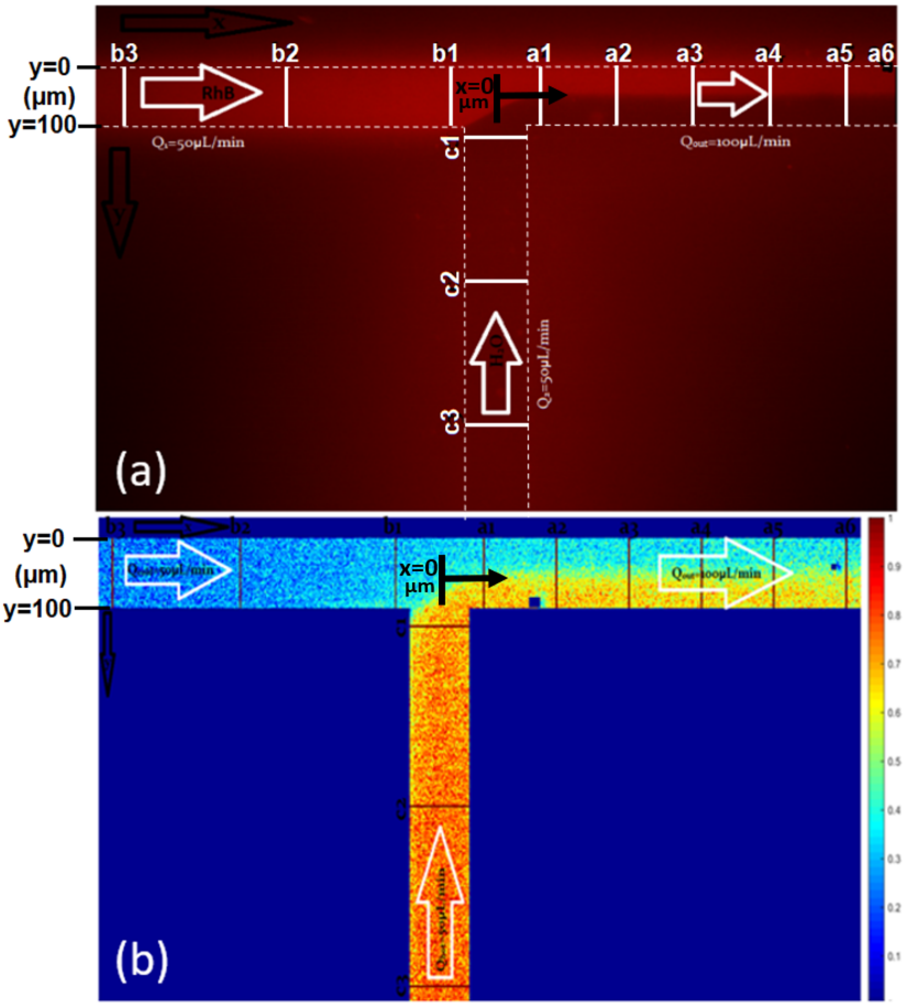

Figure 4.16: (a) Isothermal flow 90° microchannel; (b) Non-isothermal flow 90° microchannel.

4.2.1 RhB concentration vs Temperature distribution

As before, to normalize the RhB concentration profiles, the parameter $a_i/max(max(a_i))$ was adopted. Temperature profiles were obtained using a 9-point moving average (using, besides the central pixel, 4 pixels before the central pixel and 4 after the central pixel, substituting the value of that central pixel by the mean of the 9 values) along the lines (a,b and c) depicted in the above-mentioned figures.

For $a_i/max(max(a_i))$:

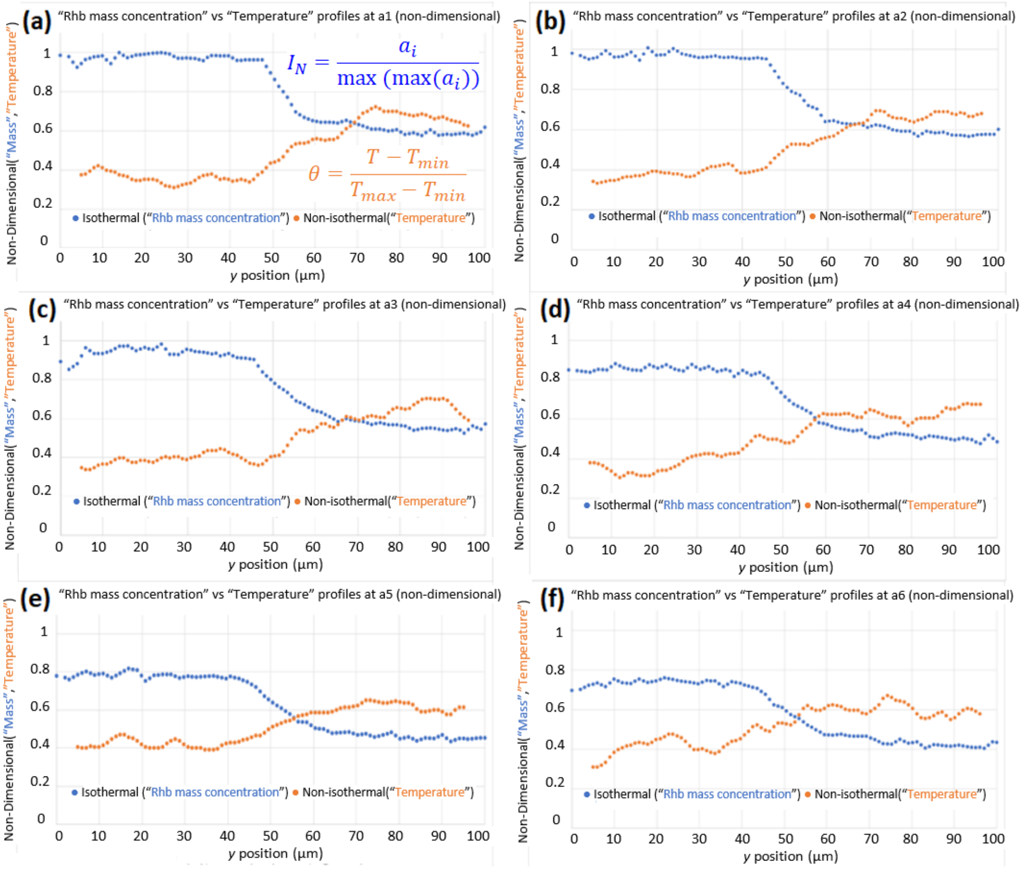

Figure 4.17: RhB "mass concentration" and Temperature profiles at (a) *a1*; (b) *a2*; (c) *a3*; (d) *a4*; (e) *a5*; (f) *a6*.

The blue points in Figure 4.17 represent the normalized pixel intensity that is proportional to the RhB mass concentration (isothermal flow, higher values correspond to more RhB in the solution) and orange points represent the non-dimensional temperature (non-isothermal flow). In both cases different areas can be identified. For the RhB concentration, a high concentration area, a transition area and a low concentration area are evident. As for temperature, a hot area, a cold area and a transition area are evident as schematized in Figure 4.18. Transition starts when concentration/temperature starts to rise/fall and ends when the variable stabilizes again.

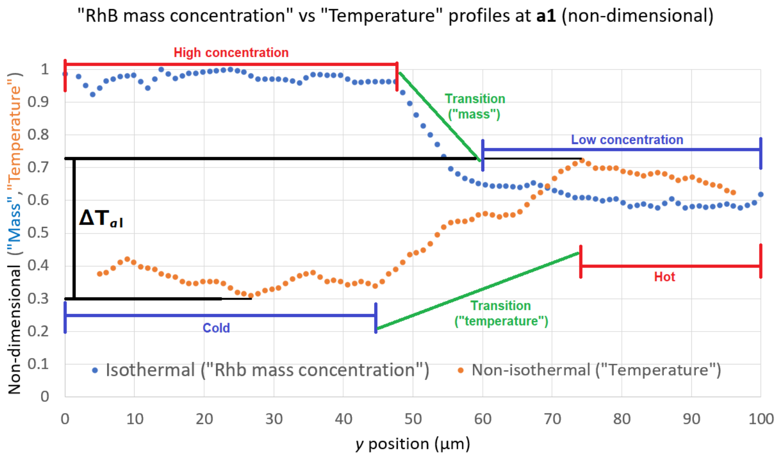

Figure 4.18: Illustration of the different zones at position *a1* (blue-Concentration; orange-Temperature).

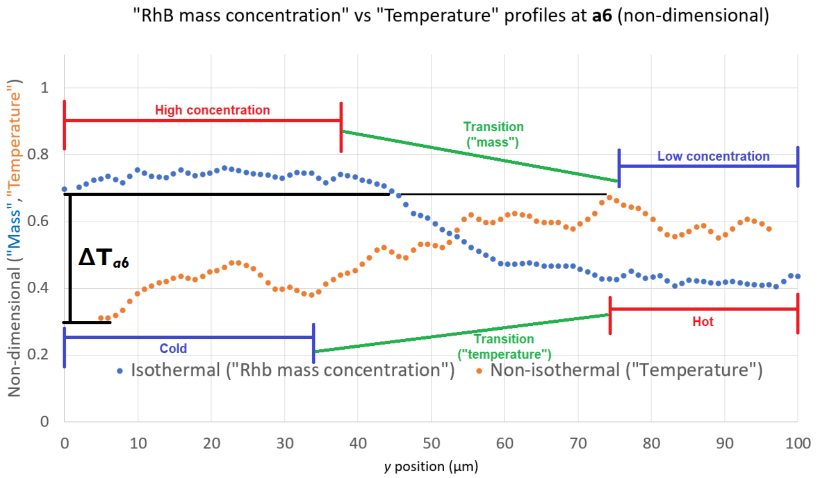

Figure 4.19: Illustration of the different zones for *a6* (blue-Concentration; orange-Temperature).

There is a defined pattern that corresponds to both the temperature and concentration: after a more or less defined plateau both start and end the transition zone at approximately the same position, returning to another plateau, which indicates that there is a clear separation of the fluids both for the concentration (blue points) and for the temperature (orange points). Cold fluid is present $y = 0$ and hot fluid near $y = 100\mu m$. The slope of the transition zone is less steep as the analysis stations are closer to the outlet of the channel. This means that the temperature gradient is smoother as the flow moves downstream the outlet channel, suggesting that heat transfer by diffusion has occurred. The same behavior is identified for RhB concentration where $y = 0$ corresponds $max_{concentration}$ and $y = 100\mu m$ corresponds to $min_{concentration}$), although with a steeper gradient, which suggests that mass transfer has occurred but at a lower rate when compared to heat transfer (Figure 4.19). This can be explained by the *Lewis* number (Le).

This parameter is defined as the ratio between the thermal diffusivity and the mass diffusivity. It is used to characterize fluid flows where there is simultaneously heat and mass transfer.

$$Le = \frac{\alpha}{D} = \frac{Sc}{Pr} \tag{4.11}$$

With:

- α is the thermal diffusivity (m^2/s).
- Pr is the non-dimensional Prandtl number ($Pr = \frac{c_p \mu}{k}$)

In this case:

$$\alpha_{RhBsol} \approx \alpha_{H_2O}$$
$$D = D_{H_2O-H_2O} \text{ (water self-diffusion problem as discussed previously)}$$

In this experiment, the temperature ranges from $T_{min} = 26℃$ and $T_{max} = 50℃$. To take this into account, two different Lewis numbers will be computed: Le_{hot}, corresponding to T_{max} and Le_{cold} to T_{min}.

For Le_{cold}:

$$\alpha_{H_2O(25℃)} = 1.45 \times 10^{-7} m/s$$
$$D_{(25℃)} = 2.57 \times 10^{-9} (m^2/s)$$
$$Le_{cold} = \frac{1.45 \times 10^{-7}}{2.57 \times 10^{-9}} = 56$$

For Le_{hot}:

$$\alpha_{H_2O(50℃)} = 1.56 \times 10^{-7} m/s$$
$$D_{(50℃)} = 9.51 \times 10^{-9} (m^2/s)$$
$$Le_{hot} = \frac{1.56 \times 10^{-7}}{9.51 \times 10^{-9}} = 16$$

Since both values are greater than 1, it is expected that thermal diffusivity dominates over mass diffusivity in every section of the channel. This means that the characteristic mass diffusion time (which can be defined as L^2/D) is much larger than that of the heat diffusion characteristic time (which can be defined as L^2/α). This fact justifies and corroborates the wider and faster growing transition zone for temperature (heat transfer) than for concentration (mass transfer).

An overall temperature decrease is observed between the maximum value located in the hot zone (near $y = 100\mu m$) and the minimum one located in the cold zone (near $y = 0$)). This also evidences that there is some heat transfer from the hot fluid towards the cold fluid along the outlet channel with $\Delta T_{a1} \approx 0.41$ and $\Delta T_{a6} \approx 0.3$ ($\Delta T_{a1} > \Delta T_{a6}$, with $\Delta T = T_{max} - T_{min}$). It can also be noted that, comparing the two zones hot and cold, the decrease in temperature for the first is higher than the increase verified in the latter suggesting that heat is being loss to the walls.

4.2.2 Transition zone

As far as the transition zone along the outlet channel is concerned, for stations *a1* to *a6*, the location of its starting pixel (measured from $y = 0$)and its length were obtained and plotted in a single graph. In this graph and future ones, sections *a1* to *a6* are substituted for the actual distance of each from the beginning of the confluence ($x = 0$, where the two fluids meet) – see Figure 4.20.

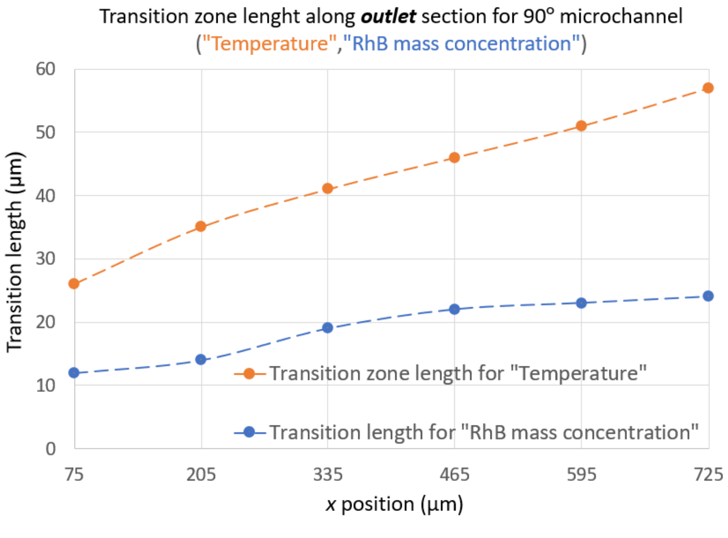

Figure 4.20: Transition zone length along outlet channel section for 90° microchannel

As can be observed in Figure 4.20, considering the “Temperature” data (orange), the transition widens considerably along the outlet channel length when compared to the concentration (blue) one. The latter has a much slower growth rate, as the slope suggests, and an overall smaller length.

4.2.3 Thermal mixing

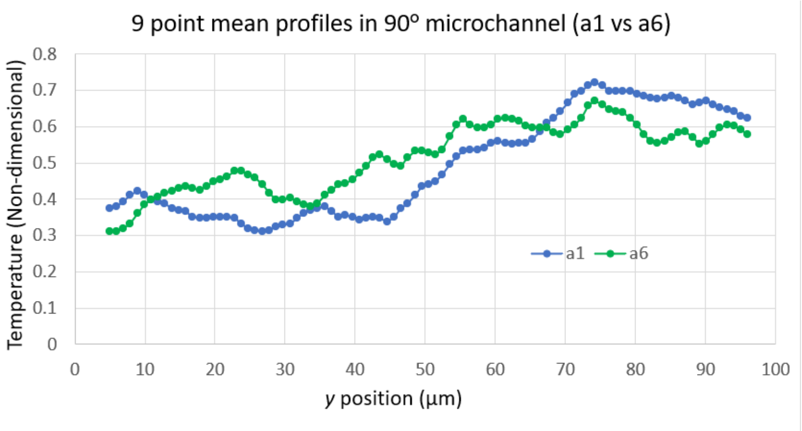

Figure 4.21: *a1* and *a6* comparison for 90° microchannel ("Temperature")

Figure 4.21, which shows the non-dimensional thermal profiles at $x = 75\mu m$ (*a1*-nearest from intersection) and $x = 725\mu m$ (*a6*-closest to the outlet), evidences that heat is being transferred from the hot to the cold fluid: the cold zone, near $y = 0$ (33% width), gets warmer and the hot zone, near $y = 100\mu m$ (38% width), gets colder. From *a1* to *a6*, the slope gets smoother and temperature increase about 10% near $y = 0$ and decreases about 10% near $y = 100\mu m$ suggesting that heat was transfer along the outlet by diffusion. A

4.2.3.A Prandtl number

For the purpose of understanding the transfer process of thermal diffusion, the Prandtl number (*Pr*), equivalent to the Schmidt number in mass transfer, should be investigated since it provides a comparison between momentum diffusivity and thermal diffusivity. The magnitude of this parameter defines which mechanism dominates the process. If $Pr << 1$, thermal diffusivity dominates, which means that heat diffusion has a characteristic time (L^2/α) smaller than that of the momentum diffusion (L^2/v). If, otherwise $(Pr >> 1)$ momentum diffusivity dominates, which means that heat diffuses much slower than momentum.

Prandtl number is defined as expressed by (4.12).

$$Pr = \frac{\nu}{\alpha} = \frac{c_p \mu}{k} \tag{4.12}$$

Where:

- c_p is the specific heat $(J/kg.K)$.

- **k** is the thermal conductivity ($W/m.K$).

The same strategy used for Lewis number will be performed for the Prandtl number (Pr_{hot} and Pr_{cold}).

For Pr_{cold}:

$$C_{p(25°C)} = 4180(J/kg{\cdot}K)$$
$$k_{(25°C)} = 604.41 \times 10^{-3}(W/m.K)$$
$$\mu_{(25°C)} = 893.41 \times 10^{-6}(N.s/m^2)$$
$$Pr_{cold} = \frac{4180 \times 893.41 \times 10^{-6}}{604.15 \times 10^{-3}} = 6.2$$

For Pr_{hot}:

$$C_{p(50°C)} = 4181(J/kg{\cdot}K)$$
$$k_{(50°C)} = 643.15 \times 10^{-3}(W/m.K)$$
$$\mu_{(50°C)} = 546.13 \times 10^{-6}(N.s/m^2)$$
$$Pr_{hot} = \frac{4181 \times 546.13 \times 10^{-6}}{643.15 \times 10^{-3}} = 3.6$$

Although $Pr > 1$ (6.2 and 3.6 for cold and hot fluids respectively), the order of magnitude is the same, meaning that momentum diffusion is not substantially higher than thermal diffusion. The fact that $Pr > 1$, suggests a slow thermal diffusion explaining why there is only a slight difference between the non-dimensional temperature profiles at stations *a1* and *a6*. It is also important to define the thermal entry length in order to evaluate the thermal development of the flow. 4.13 defines the thermal entry length for a laminar flow:

$$(\frac{x_{fd,t}}{D_H})_{lam} \approx 0.05 Re_{D_H} Pr \tag{4.13}$$

Where:

- $x_{fd,t}$ is the thermal entry length (m).

In this work $(\frac{x_{fd,t}}{D_H})_{lam} \approx 2.88$ which means that the flow is expected to be thermally fully developed at *a6*.

4.2.4 Energy Balance

A general energy balance will be conducted to the system to better understand the heat transfer mechanism in play and the possible energy losses present.

The general energy balance runs:

$$\dot{E}_{in} - \dot{E}_{out} + \dot{E}_{g} = \dot{E}_{st} \tag{4.14}$$

Where: $\dot{E}_{in}$ is the energy entering the system per unit time, $\dot{E}_{out}$ the energy leaving the system per unit time, $\dot{E}_{st}$ the energy stored in the system per unit time and $\dot{E}_{g}$ the energy generated internally by the system per unit volume and unit time. When applied to the system (defined as schematized in Figure 4.22 by the hot and cold fluids), $\mathbf{\dot{E}_{st}}$ **and** $\mathbf{\dot{E}_{g}}$ can be considered nil, assuming steady state conditions and no heat sources/sinks (system left running for enough time to reach equilibrium). Heat transfer between the system and the solid boundaries can occur by 3 mechanisms: conduction, convection, and radiation. Separating the $\dot{E}_{out}$ term into two components, one referring to the energy leaving the system with the fluids flow ($\sum_{j=outlets} \dot{m}_j H_j$, and the other referring to the heat losses through the channel walls ($\dot{E}_{loss} = A_{mechanism} q"_{mechanism}$), (4.14) becomes:

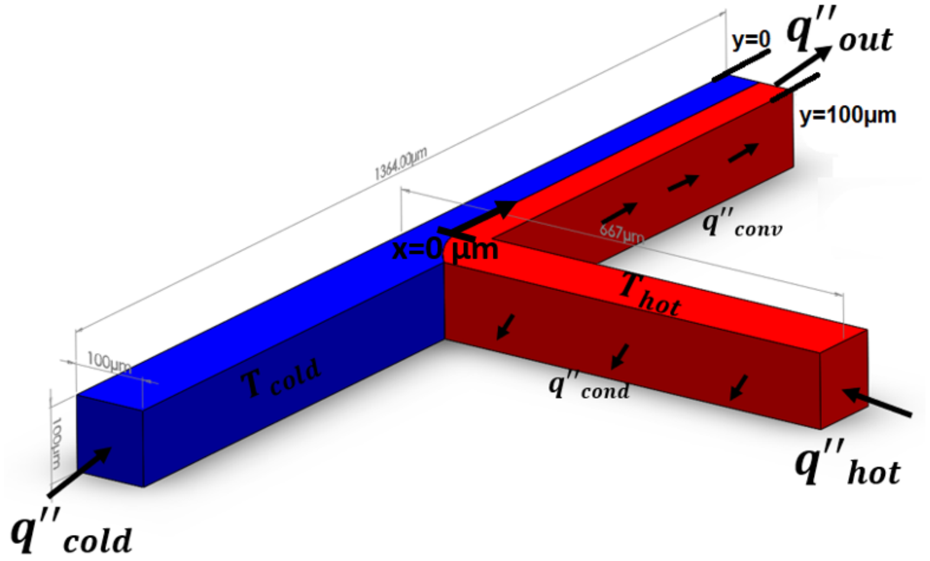

Figure 4.22: 90° microchannel 3D image (solidworks)

$$\dot{E}_{in} - \dot{E}_{out} = 0 \tag{4.15}$$

$$\sum_{i=outlets} \dot{m}_i H_i = \sum_{j=outlets} \dot{m}_j H_j + A_{cond} q"_{cond} + A_{conv} q"_{conv} + A_{rad} q"_{rad} \tag{4.16}$$

Where:

- $\dot{m}_i$ is the mass flow rate (m^3/s)).
- H_i is the enthalpy (J/kg).
- $q"_{cond}$ is the heat flux by conduction per unit time (W/m^2).
- $q"_{conv}$ is the heat flux by convection per unit time (W/m^2).
- $q"_{rad}$ is the heat flux by radiation per unit time (W/m^2).
- A_{cond} is the area perpendicular to the conduction heat flux (m).
- A_{conv} is the area perpendicular to the convection heat flux (m).
- A_{rad} is the area perpendicular to the radiation heat flux (m).

4.2.4.A Conduction

Fourier's law characterizes heat conduction (4.17).

$$\overrightarrow{q"_{cond}} = -k\nabla T \tag{4.17}$$

Where:

- $\overrightarrow{q"_{cond}}$ is the conduction heat flux vector in the direction opposing the temperature gradient(W/m^2).
- ∇T is the temperature gradient (K/m).

Conduction may occur between the PDMS walls and the fluid inside the microchannel but since the heat loss due to convection is dominant and the thermal conductivity of the water is very small, conduction heat transfer will be neglected as a simplification. In fact, this conduction is considered only below at the fluid/PDMS interface (convection).

4.2.4.B Convection

The convection heat transfer mode is comprised of two mechanisms: diffusion (transfer due to random molecular motion) and advection. Convection heat transfer occurs between a fluid in motion and a bounding surface when the two are at different temperatures. It can be calculated using Newton's law of cooling (4.18):

$$q"_{conv} = h(T_s - T_\infty) \tag{4.18}$$

Where:

- h is the convection heat transfer coefficient $(W/m^2.K)$.
- T_s is the surface temperature $(K or ℃)$.
- T_∞ is the fluid temperature $(K or ℃)$.

In this case $h = h_{RhBSol} \approx h_{H_2O}$. For a rectangular microchannel in a fully developed laminar flow with uniform wall temperature, considering that the PDMS wall temperature remains constant and equal to the room temperature, as presented in [8] (4.19):

$$Nu_T = 7.541(1 - 2.610\alpha_c + 4.970\alpha_c^2 - 5.199\alpha_c^3 + 2.702\alpha_c^4 - 0.548\alpha_c^5 \tag{4.19}$$

With $\alpha_c = \frac{a}{b} = 1$, in this case since the channel has square cross section.

$$Nu_T = 7.541(1 - 2.610 + 4.970 - 5.119 + 2.702 - 0.548) = 2.98$$

or the convection heat transfer coefficient (4.21):

$$h = \frac{Nu_T k}{D_h} \tag{4.20}$$

$$k_{H20}(30.9℃) \approx 620 \times 10^{-3}(W/m.K);\ k_{H20}(44.4℃) \approx 635 \times 10^{-3}(W/m.K)\ [44]$$

$$h_{H_2O(30.9℃)} = \frac{2.98 \times 620 \times 10^{-3}}{10^{-4}} = 1847.6(W/m^2.K)$$

$$h_{H_2O(50℃)} = \frac{2.98 \times 635 \times 10^{-3}}{10^{-4}} = 1892.3(W/m^2.K)$$

4.2.4.C Radiation

Thermal radiation is the energy emitted by matter that is at a nonzero absolute temperature. It does not require a presence of a material medium like conduction or convection and can be transfered in vacuum. **Stefan-Boltzman law** sets an upper limit for the emissive power (E), which is the rate at of energy release per unit area (W/m^2) (4.21).

$$E_b = \sigma T_s^4 \tag{4.21}$$

Where:

- $\mathbf{E_b}$ is the emissive power of a black body (W/m^2).
- σ is the **Stefan-Boltzman** constant $\sigma = 5.67 \times 10^{-8} (W/m^2K^4)$.

This law applies only to a blackbody (ϵ=1). For actual surfaces the radiative heat flux is (4.22):

$$E = \epsilon\sigma T_s^4 \tag{4.22}$$

Where:

- E is the emissive power (W/m^2).
- ϵ is the emissivity ($0 \leq \epsilon \leq 1$).

The incident radiation on the surface is called irradiation (G). Part of that radiation can be absorbed by the surface. The rate at which radiant energy is absorbed per unit surface area may be evaluated from knowledge of a surface radiative property termed absorptivity. That is (4.23):

$$G_{abs} = \alpha_{abs} G \tag{4.23}$$

Where:

- G is the incident radiation (W/m^2).
- α_{abs} is the absorptivity ($0 \leq \alpha_{abs} \leq 1$).
- $\alpha = 1$, opaque
- $\alpha = 0$, transparent

The net rate of radiation heat transfer from the surface, expressed per unit are of the surface, is (4.24):

$$q_{rad}" = \epsilon E_b - \alpha_a bsG \tag{4.24}$$

Where:

- $q"_{rad}$ is the radiative heat flux (W/m^2)

4.2.5 Energy Balance applied to the system

After defining all the mechanisms of heat transfer, it is important to quantify the losses in this work system. For this purpose a small study on heat losses will be addressed. To evaluate $T_{in(cold)}$, $T_{in(hot)}$ and T_{out}, the mean values at section *b1*, *c1* and *a6* respectively were used. For $T_{mean@coldwall}$ and $T_{mean@hotwall}$ a mean value was obtained using all the pixels in the outlet channel near $y = 0$ for the first and near the $y = 100\mu m$ wall for the latter. Figure 4.22 represents the system in analysis.

Data:

$T_{amb} = T_{wall} = 25(^{\circ}C)$
$T_{in(cold)} = 31.3(^{\circ}C)$
$T_{mean@coldwall} = 31.3(^{\circ}C)$
$T_{out} = 38.4(^{\circ}C)$
$T_{mean@hotwall} = 43(^{\circ}C)$
$T_{in(hot)} = 44.4(^{\circ}C)$
$T_{Out} = 38.4(^{\circ}C)$
$h_{H_20(30.9^{\circ}C)} = 1847.6(W/m^2.K)$
$h_{H_20(43^{\circ}C)} = 1892.3(W/m^2.K)$

$\dot{Q}_{cold} = \dot{Q}_{hot} = 0.833(3) \times 10^{-9}(m^3/s)$
$\dot{Q}_{out} = 1.666(6) \times 10^{-9}(m^3/s)$
$\rho_{H_20(31.3^{\circ}C)} = 995.0(kg/m^3)$ [44]
$\rho_{H_20(44.4^{\circ}C)} = 990.1(kg/m^3)$ [44]
$\rho_{H_20(38.4^{\circ}C)} = 993.0(kg/m^3)$ [44]
$H_{H_20(31.3^{\circ}C)} = 131164(J/kg)$ [45]
$H_{H_20(44.4^{\circ}C)} = 185926(J/kg)$ [45]
$H_{H_20(38.4^{\circ}C)} = 160842(J/kg)$ [45]
$A_{in(cold)} = A_{in(hot)} = A_{in} = 1 \times 10^{-8}(m^2)$

Assumptions:

- Steady-state flow ($\frac{d}{dt} = 0$)
- $T_{amb} \approx T_{wall}$, remains constant in all regions of the microchannel.
- $q"_{rad} \approx 0$, microscale problem, radiation might only be relevant at larger temperature values.
- $q"_{cond} \approx 0$, water thermal conductivity is very small meaning that conduction is negligible comparing to convection.
- $q"_{conv}$ is evaluated using $T_{mean@hotwall}$ in the hot region, and $T_{mean@coldwall}$ in the cold region.

$$q"_{conv(cold)} = h_{H_20(30.9^{\circ}C)} \times (T_{mean@coldwall} - T_{wall}) = 1847.6 \times (30.9 - 25) = 1.09 \times 10^4 W/m^2$$
$$q"_{conv(hot)} = h_{H_20(43^{\circ}C)} \times (T_{mean@hotwall} - T_{wall}) = 1892.3 \times (43 - 25) = 3.4 \times 10^4 W/m^2$$

$$\dot{E}_{loss,conv} = A_{conv} q"_{conv} \tag{4.25}$$

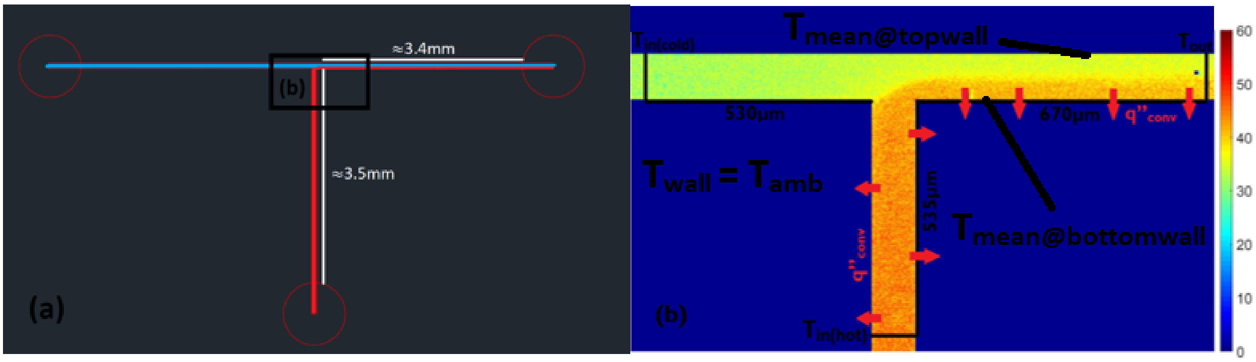

Figure 4.23: (a) Simplification of 90° microchannel hot (red) and cold (blue) zones. Image taken from AutoCAD software; (b) Region of analysis.

With (Figure 4.23):

$$A_{conv(cold)} = (4 \times 530 \times 10^{-6} \times 100 \times 10^{-6}) + (670 \times 10^{-6} \times 100 \times 10^{-6} \times 2)$$
$$A_{conv(cold)} = 2.12 \times 10^{-7} + 1.34 \times 10^{-7} = 3.46 \times 10^{-7} m^2$$
$$A_{conv(hot)} = (4 \times 535 \times 10^{-6} \times 100 \times 10^{-6}) + (670 \times 10^{-6} \times 100 \times 10^{-6} \times 2)$$
$$A_{conv(hot)} = 2.14 \times 10^{-7} + 1.34 \times 10^{-7} = 3.48 \times 10^{-7} m^2$$

$$\dot{E}_{loss,conv} = \dot{E}_{loss,conv(hot)} + \dot{E}_{loss,conv(cold)} \tag{4.26}$$

$$\dot{E}_{loss,conv} = 3.46 \times 10^{-7} \times 1.09 \times 10^{4} + 3.48 \times 10^{-7} \times 3.4 \times 10^{4} \approx 0.015W$$

$$\dot{E}_{in} = \dot{m}_{cold} \times H_{H_2O(31.3℃)} + \dot{m}_{hot} \times H_{H_2O(44.4℃)} \tag{4.27}$$

$$\dot{E}_{in} = \dot{Q}_{cold} \times \rho_{H_2O(31.3℃)} \times H_{H_2O(31.3℃)} + \dot{Q}_{hot} \times \rho_{H_2O(44.4℃)} \times H_{H_2O(44.4℃)}$$
$$\dot{E}_{in} = 0.833(3) \times 10^{-9} \times 995.0 \times 131164 + 0.833(3) \times 10^{-9} \times 990.1 \times 185926$$
$$\dot{E}_{in} = 0.262(W)$$

$$\dot{E}_{out} = \dot{Q}_{out} \times \rho_{H_2O(38.4℃)} \times H_{H_2O(38.4℃)} \tag{4.28}$$

$$\dot{E}_{out} = 1.666(6) \times 10^{-9} \times 993 \times 160842$$
$$\dot{E}_{out} = 0.266(W)$$

$\dot{E}_{in} < \dot{E}_{out}$ suggesting that heat is entering the system elsewhere. By letting the system run for a couple of minutes, to ensure steady state conditions, heat was also added to the system through the use of the heater positioned very close to the PDMS structure. It was dissipated to the PDMS walls raising the temperature above ambient, resulting in energy entering the system in the cold zone instead of leaving it, through convection as it was first assumed. Ways to mitigate this problem are, increasing the PDMS height and/or applying cooling (forced convection), with air at ambient temperature by the use of a fan or other cooling system. This can mitigate the problem and reduce the heat being added to the system via the walls. Other option is to change the heater location but, as it was discussed in the previous chapter, heat loss in the tube can become an issue.

4.3 Non-isothermal flow

4.3.1 Influence of confluence angle in transition zone length and location

After detailing the phenomena ocurring in the $90°$ shaped microchannel using the same volumetric flow rate ($Q_{cold} = 50\mu L/min$) in both inlets, a study on the confluence angle, the angle between the two inlets, will be addressed . Figure 4.24 shows the change in temperature transition length for the different shaped microchannels, $30°$, $60°$, $90°$, $135°$ along the outlet channel where $x = 0$ denotes where thermal mixing starts to occur (note that first analysed sections are located approximately at $x = 75\mu m$ for all cases). By fixing the volumetric flow rate for all the configurations, angle effects can be better understood. The obtained plot is a combination of the temperature profiles obtained with *Matlab* analysis of the images resulting in a more accurately defined transition zone. Processed images from flow in the different shaped microchannels can be seen in the Appendix B.

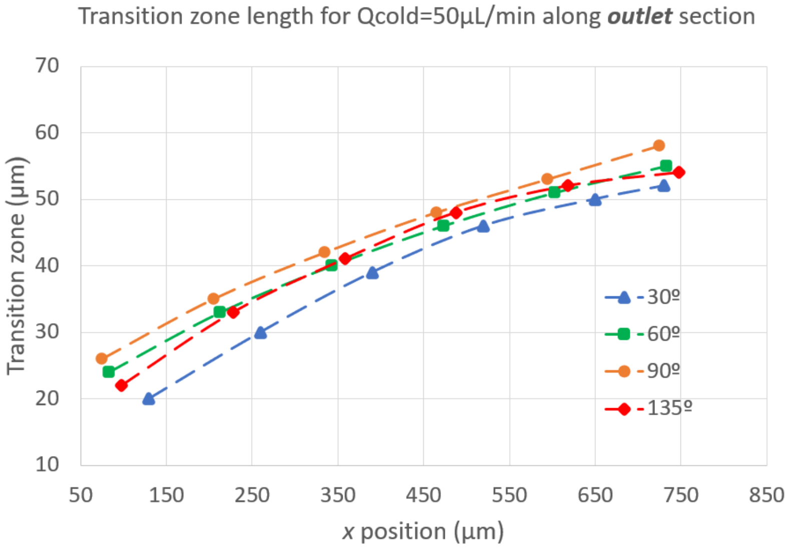

Figure 4.24: Transition zone length using $Q_{cold} = 50\mu L/min$ along outlet section for different confluence angles.

When observing Figure 4.24 it can be noted that the $30°$ configuration yields the smallest transition zone along all outlet channel length. In this configuration, the hot stream will be pressed against $y = 100\mu m$, due to the small angle, and the portion of the outlet channel containing hot fluid will be smaller when compared to the $60°$ or the $90°$ configurations. In $60°$ and $90°$ configurations, the hot stream is able to penetrate the cold stream further due to the higher angle between both streams, resulting in a much wider region where hot fluid is present, this can be noticed in a simplified representation of the temperature profiles (Non-dimensional - θ) in each microchannel configuration stated in Figure 4.25. In this type of figures, $y = 0$ denotes the top wall and $y = 100\mu m$ the bottom wall.

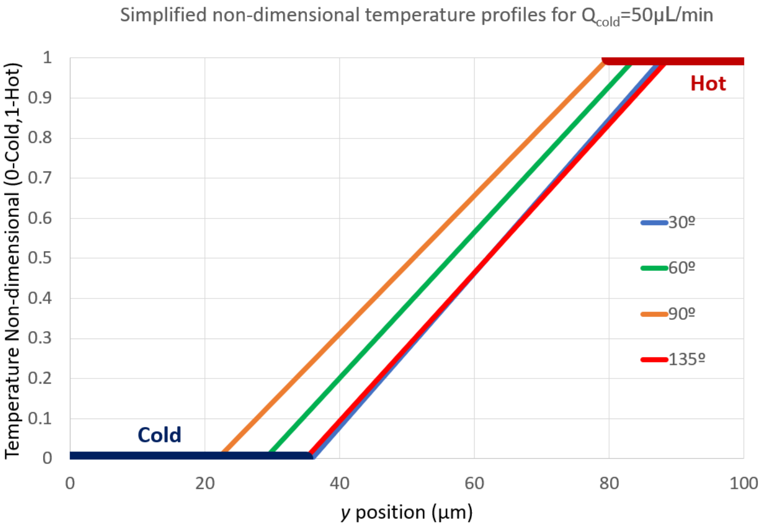

Figure 4.25: Simplified non-dimensional profiles using $Q_{cold} = 50\mu L/min$ at the last data point (*a6*) for different confluence angles.

For the $30°$ and $135°$ shaped microchannels, there is a much larger cold zone near $y = 0$ that remains unaffected by the hot stream, creating a transition zone located much closer to $y = 100\mu m$. Focusing on the first ($30°$), the transition zone is located between $36\mu m$ and $88\mu m$ resulting in a width of $52\mu m$. The latter ($135°$) is between $35\mu m$ and $90\mu m$ with a size of $54\mu m$. The $135°$ configuration is the only that experiences counterflow, which results in a slightly wider transition zone early (when compared to $30°$ (Figure 4.24)) on the channel due to the streams collision. This collision can enhance local advection and enhances mixing near that region, despite being diffusion heat transfer the main mechanism for all the cases, as discussed before. It creates a semicircular shape that generates some disruption in the flow movement, observed by the oscillation seen in the temperature images (Appendix B), that can explain the different overall behavior (growth), when comparing to other configurations.

It can be observed that with the increase in angle (until 90°), the transition zone becomes more centered and symmetrical (Figure 4.26). The $90°$ shaped microchannel is the one with the widest transition zone length (58μm) due to the fact that it can grow by cooling the fluid near $y = 100\mu m$ and heat the fluid in $y = 0$ resulting in a more symmetrical heat transfer along the microchannel width (from $22\mu m$

to $80\mu m$). Being the $30°$ and 135° configurations the ones that experience a transition zone closer to $y = 100\mu m$, when all the fluid near that wall transfers heat, the growth can only happen by heating of the cold fluid near the opposing wall. As can be observed in Figure 4.24, a decrease in slope is evident for these two configurations, when looking at the last data points, while for the $60°$ and the $90°$ a continuous growth is expected for further positions along the outlet channel. Of all configurations the $90°$ has the most symmetrical and largest transition zone.

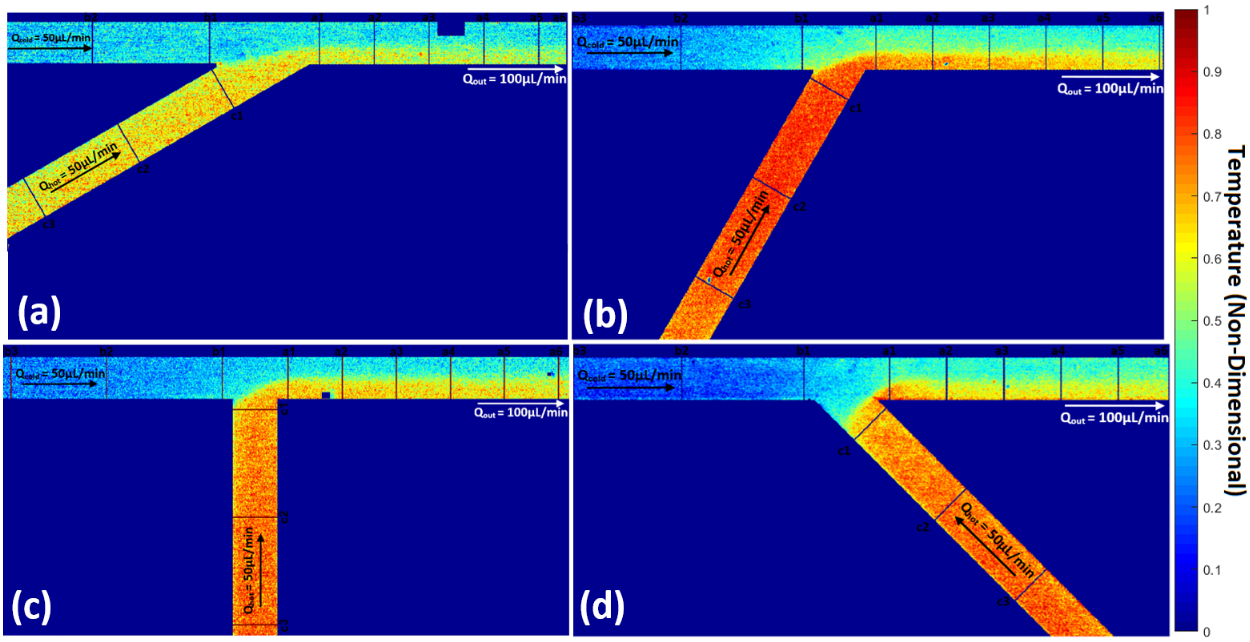

Figure 4.26: Microchannel configurations for $Q_{cold} = Q_{hot} = 50\mu L/min$; (a) 30°, (b) 60°, (c) 90°, (d) 135°.

4.3.2 Influence of volumetric flow rate on transition zone length and location

Having discussed the effect of confluence angle on transition zone length and location, a study on the effect of changing the cold inlet volumetric flow rate will be addressed. Three different volumetric flow rates, $Q_{cold} = 25\mu L/min$, $50\mu L/min$ and $75\mu L/min$, will be analyzed for the four, $30°$, $60°$, $90°$ and $135°$, configurations. Processed images corresponding to all the data presented are available in Appendix B.

4.3.3 $30°$ shaped microchannel

Figure 4.27 shows the change in transition zone length for the different cold volumetric flow rates for the $30°$ microchannel along the outlet channel, while Figure 4.28 illustrates the simplified non-dimensional profiles at point (*a6*) for the same conditions.

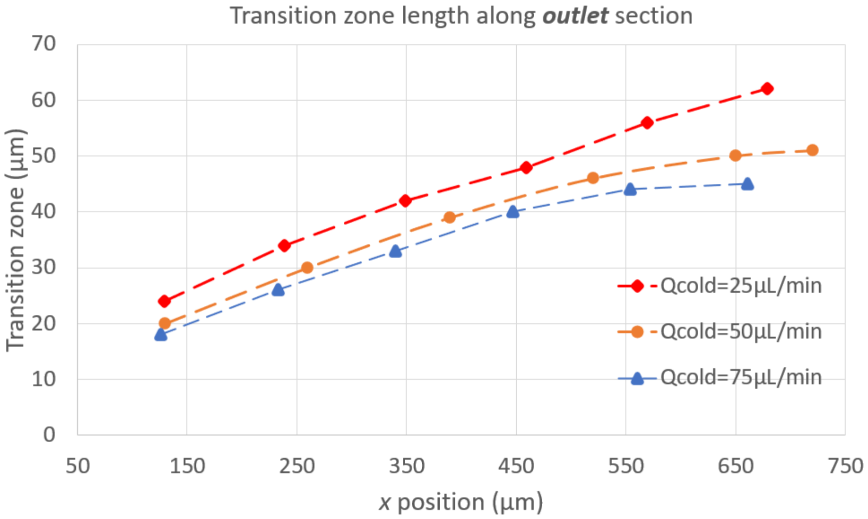

Figure 4.27: Transition zone length along outlet for $30°$ microchannel for different volumetric flow rates.

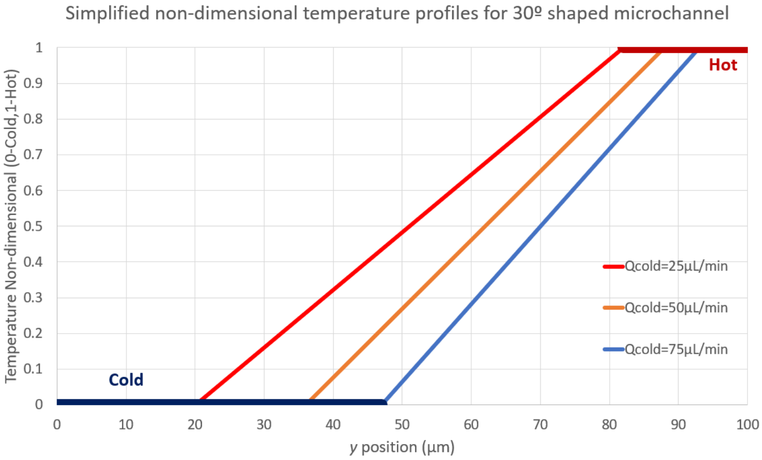

Figure 4.28: Simplified non-dimensional profiles for $30°$ shaped microchannel at the last data point (*a6*) for different volumetric flow rates.

For this configuration, observing Figure 4.27 focusing on the last point (*a6*), it can be noted that increasing the cold volumetric flow rate (to $75\mu L/min$) leads to an smaller transition zone ($47\mu m$ to $93\mu m$, $45\mu m$ in size) and, focusing on the blue data in Figure 4.28, to a thinner hot zone (when comparing to the symmetric case). The combination of a small angle and a higher cold stream leads to an even greater constriction of the hot fluid against $y = 100\mu m$ resulting in a slower increase in transition zone length. By reducing the cold volumetric flow rate (to $25\mu L/min$) the opposite occurs, the hot fluid can reach closer to $y = 0$ and a more symmetrical transition zone can be obtained, as can be observed in Figure 4.28 denoted by the red line. This results in a faster increase in transition zone length which can be verified by the relatively high slope in the data showed in Figure 4.27. This decrease in the cold volumetric flow rate counteracts the low confluence angle $(30°)$ making this combination a good option to achieve a more symmetrical $(20\mu m$ to $82\mu m)$ and wider $(62\mu m)$ transition zone .

4.3.4 $60°$ shaped microchannel

Figure 4.29 shows the change in transition zone length for the different cold volumetric flow rates for the $60°$ microchannel along the outlet channel, while Figure 4.30 illustrates the simplified non-dimensional profiles at point (*a6*) for the same conditions.

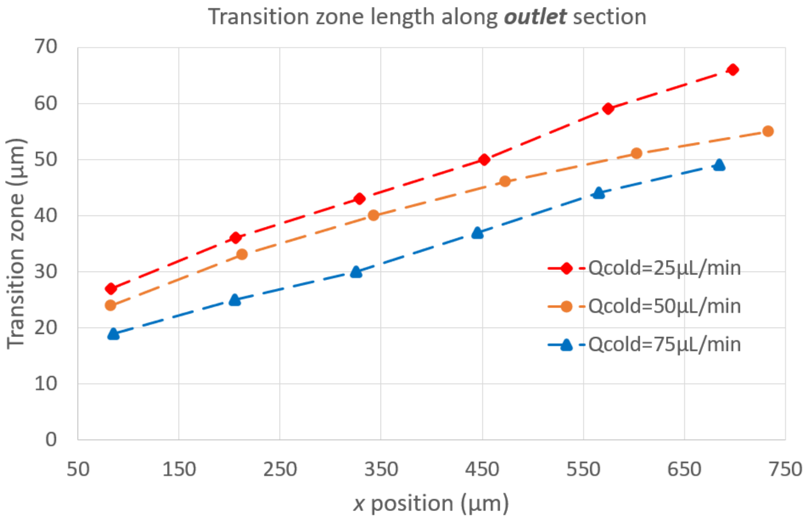

Figure 4.29: Transition zone length along outlet for $60°$ microchannel for different volumetric flow rates.

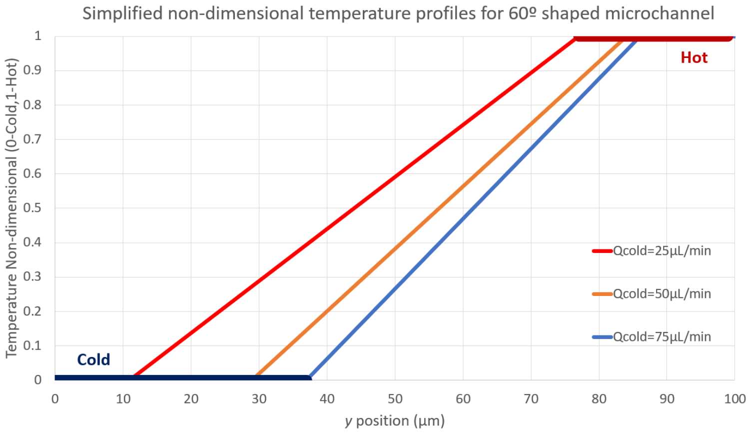

Figure 4.30: Simplified non-dimensional profiles for $60°$ shaped microchannel at the last data point (*a6*) for different volumetric flow rates.

The $60°$ configuration results are similar to the previous case, with an overall increase of the transition zone length (upwards vertical shift in Figure 4.29) and a reduction of the cold zone near $y = 0$ (horizontal shift towards the left in Figure 4.30. It is important to note that for $Q_{cold} = 75\mu L/min$ the transition zone grows faster ($37\mu m$ to $86\mu m$, $48\mu m$ in size) for the $60°$ in comparison to the $30°$ configuration, due to the combination of confluence angle and volumetric flow rate. For the first, the higher angle mitigates the effect of a higher cold stream resulting in a faster growing transition zone.

4.3.5 $90°$ shaped microchannel

Figure 4.31 shows the change in transition zone length for the different cold volumetric flow rates for the $90°$ microchannel along the outlet channel, while Figure 4.32 illustrates the simplified non-dimensional profiles at point (*a6*) for the same conditions.

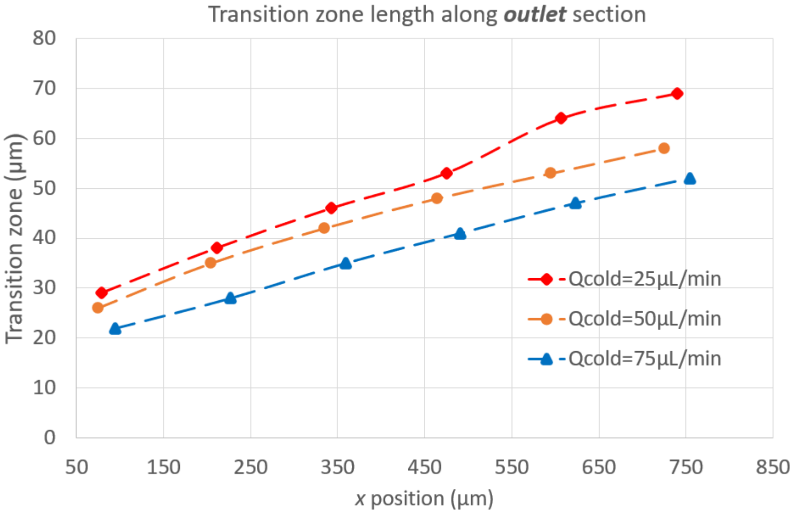

Figure 4.31: Transition zone length along outlet for $90°$ microchannel for different volumetric flow rates.

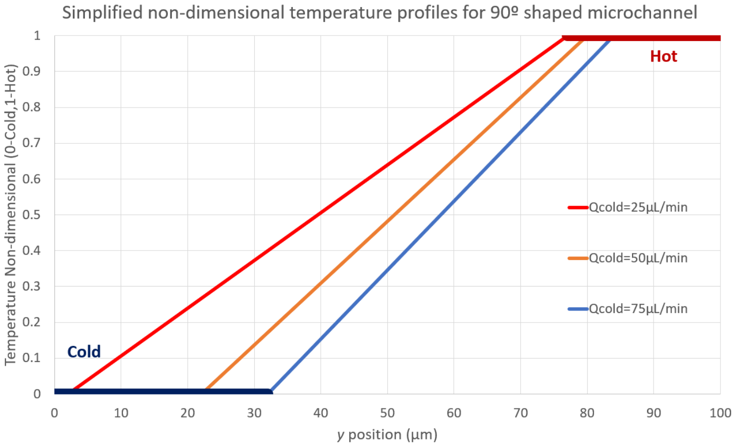

Figure 4.32: Simplified non-dimensional profiles for $90°$ shaped microchannel at the last data point (*a6*) for different volumetric flow rates.

If the angle is further increase to $90°$, an additional increase in transition zone and decrease in the cold region near $y = 0$ is observed (Figure 4.31 and Figure 4.32). When Q_{cold} is set to $25\mu L/min$, combined with a high angle, the hot fluid can reach the minimum distance from $y = 0$ leading to the almost complete obliteration of the cold zone. This fact is perceived in Figure 4.32 by the small length of the cold zone,only about $3\mu m$, and in Figure 4.31 by the decrease in slope verified in the last to points, suggesting a decrease in transition zone growth for the remaining of the outlet channel. Inversely if Q_{cold} is set to $75\mu L/min$, the effect of the high angle will balance this increase in cold fluid stream, attenuating the effects, as the slope in the last points suggest in Figure 4.31, when compared to lower angle configurations.

4.3.6 $135°$ shaped microchannel

Figure 4.33 shows the change in transition zone length for the different cold volumetric flow rates for the $135°$ microchannel along the outlet channel, while Figure 4.34 illustrates the simplified non-dimensional profiles at point (*a6*) for the same conditions.

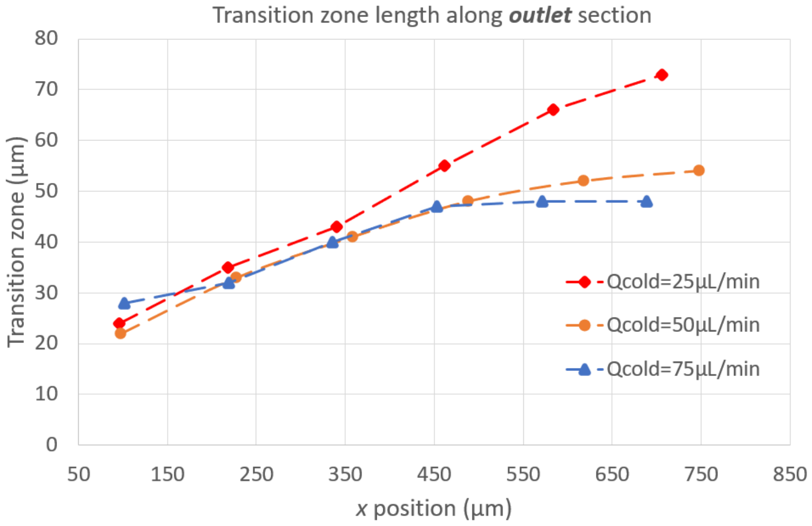

Figure 4.33: Transition zone length along outlet for $135°$ microchannel for different volumetric flow rates

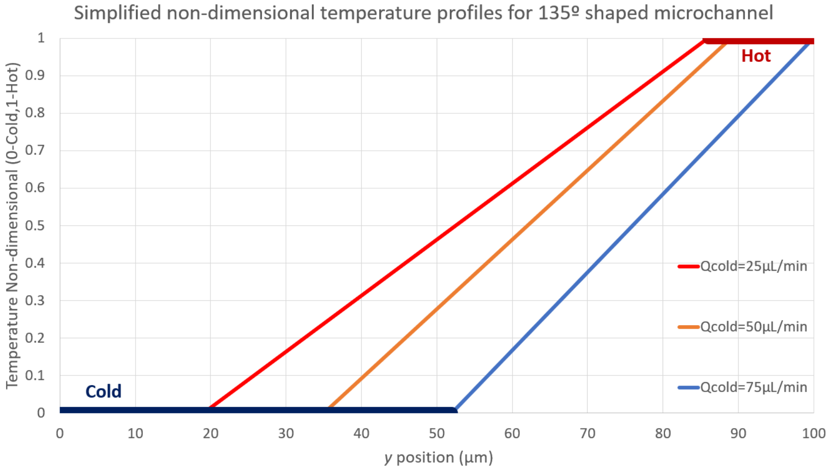

Figure 4.34: Simplified non-dimensional profiles for $135°$ shaped microchannel at the last data point (*a6*) for different volumetric flow rates.

By inducing a counterflow configuration at the junction zone, with an angle of $135°$, the hot fluid is mainly present close to $y = 100\mu m$, as discussed before. If a cold volumetric flow of $75\mu L/min$ is set for this configuration, the zone in which hot fluid is present will practically disappear making the transition zone move towards $y = 100\mu m$ ($52\mu m$ to $100\mu m$). This combination is by far the least symmetric transition zone and the high starting value showed in Figure 4.33 results from the rapid cooling of the hot fluid which explains the locally rapid increase. With this combination of factors, the transition zone will grow slowly and will be concentrated mainly near $y = 100\mu m$. On the contrary if Q_{cold} is set to $25\mu L/min$, it will balance the effect of the angle and a more symmetric transition zone ($19\mu m$ to $82\mu m$) is expected, as Figure 4.34 indicates by a much more balanced size of cold and hot zones. This almost symmetrical growth will help the transition zone to keep increasing as the slope shows in Figure 4.33. In fact, a faster growth is expected using this combination when comparing to the $90°$ using the same $25\mu L/min$ cold volumetric flow rate as the slope obtained for the two configurations demonstrates.

Chapter 5

Conclusion and future work

5.1 Concluding remarks

The main objective proposed for this work was to study the thermal behavior of two confluent flows in micron sized channels. For that, it was necessary to fabricate the microfluidic devices and heaters, perform the LIF calibration before applying the technique. The study focused on the comparison on the isothermal (Rhb concentration) with the non-isothermal (temperature) and the influence of confluence angle and volumetric flow rate in thermal transition zone length and position.

From the comparison between the isothermal case, intended to evaluate mass diffusion through the use of two confluent flows with different Rhb concentrations, and the non-isothermal case, intended to evaluate thermal mixing through the use of two different flows of the same fluid at different temperatures, various conclusions emerged. For the first case, mass transfer occurred mainly due to diffusion, as the low *Reynolds* number $(Re = 16.6)$ highlighted, and momentum diffusion dominated over mass diffusion, proven by the high *Schmith* number $(Sc = 359)$. A high *Peclet* number $(Pe = 6.48 \times 10^3)$, which combines both effects and yields the ratio between mass transferred by advection and the one transferred by diffusion, helped explaining the stratified flow observed, where the higher and lower concentration fluids were clearly segregated. For the latter (non-isothermal), momentum diffusion dominated over thermal diffusion as the *Prandtl* number $(Pr = 3.6)$ indicated. Comparing the first with the latter, it was concluded that thermal diffusion was greater than mass diffusion. This statement is supported by the *Lewis* number, which defines the ratio between thermal diffusion and mass diffusion and, being greater than one for all temperatures $(Le = 16$ for the higher temperature case) suggests that in fact thermal diffusion was greater than mass diffusion.

Relatively to the thermal transition zone analysis, the influence of two factors was discussed, confluence angle and volumetric flow rate.

An angle increase will enable the hot stream to reach regions in the outlet channel closer to $y = 0$ resulting in a more symmetric and wider thermaltransition zone. This means that the $90°$ showed the most symmetrical (from $22\mu m$ to $80\mu m$) and wider thermal transition zone $(58\mu m)$ and, on the contrary, the $30°$ configuration presented the transition zone located closest to $y = 100\mu m$ $(36\mu m$ to $88\mu m)$ and with the smallest size $(52\mu m)$. Focusing on the $135°$, because it experiences a counterflow configuration at the junction region, the hot stream has to curve towards the outlet channel, exhibiting small penetration in the cold stream. As a consequence, it yields results similar to the $30°$ as far as the to transition zone location is concerned ($35\mu m$ to $90\mu m$), but slightly wider ($54\mu m$). This fact can be explained by a local increase in advection near the junction due to the collision of the two streams enhancing thermal mixing in that area. It can be witness by a wider thermal transition zone in the first analyzed station (a1) when comparing to the $30°$ configuration which does not exhibit this kind of flow.

In regard to (cold inlet) volumetric flow rate change, it was concluded that with its reduction, the hot stream would be able to penetrate further into the cold stream resulting in a general transition zone deviation towards $y = 0$. This leads to the symmetry of the thermal transition zone in small angle and counterflow configurations, as can be observed by the $30°$ and $135°$ cases, respectively. The first transition zone was located between $20\mu m$ to $82\mu m$ (width=$62\mu m$) while the latter was from $19\mu m$ to $86\mu m$ (width=$67\mu m$) making it the wider transition zone obtained in all tests. In more symmetrical geometries (with higher angle), the impact is less important, as can be perceived looking at the $90°$ example. It exhibits a transition zone starting at $3\mu m$ and ending at $72\mu m$ (width=$69\mu m$) which is less than the one obtained for the $135°$. Finally, an increase in cold volumetric flow rate will result in thinner and less symmetric, shifted towards $y = 100\mu m$, transition zones for all the angles tested. For example, for the $30°$ configuration, transition zone is located between $47\mu m$ and $97\mu m$ resulting in a width of only $50\mu m$, the lowest obtained in this experiment.

5.2 Future work

Considering all the tasks performed to developed this thesis, some suggestions and directions can be given to improve and guide future works in this area.

- In the microfabrication process, inside the microchannels, barriers with different configurations could be created to induce advection and transient patterns, like vortices in the flow with the goal of improving mixing. This is true either for mass or thermal mixing. Other option is to increase the outlet channel length, which increases the diffusion characteristic time, giving the system more time to transfer heat or mass.

- Regarding the LIF technique, calibration and experiments that use it, could be conducted in structures in which RhB does not diffuse into them, or that are protected against this phenomenon. Other option is to use photobleaching to minimize the impact of fluorescence emission associated with RhB diffused in the walls.

- The experimental apparatus can be further improved by microfabricating a specific heater to locally heat the hot fluid and uniformize heat losses.

- Higher angles of confluence can be studied as well as barriers or longer outlets to better understand the thermal behavior in these microfluidic flows. Additionally, higher inlet flow temperatures and pulsed flows could also be adressed.

References

[1] Schulze H , Crain J , Giraud G , Bachmann T . Multiplexed optical pathogen detection with lab-on-a-chip devices. Journal of biophotonics. 2009;2(4):199–211.

[2] Damiati S , Kompella U , Damiati S A , Kodzius R . Microfluidic Devices for Drug Delivery Systems and Drug Screening. Genes. 2018;9(2):103.

[3] "Introduction to lab-on-a-chip 2020: review, history and future"; [accessed 2020 Jun 23]. Available from: https://www.elveflow.com/microfluidic-reviews/general-microfluidics/introduction-to-lab-on-a-chip-2015-review-history-and-future/.

[4] Nguyen N , Wereley S , Shaegh S . Introduction. In: Fundamentals and Applications of Microfluidics. 3rd ed. Norwood: Artech House; 2019. p. 1–10.

[5] Sonmez U , Jaber S , Trabzon L . Super-enhanced particle focusing in a novel microchannel geometry using inertial microfluidics. Journal of Micromechanics and Microengineering. 2017;27(6).

[6] Komatireddy R , Topol E . Medicine unplugged: The future of laboratory medicine. Clinical Chemistry. 2012;58(12):1644–1647.

[7] Khosla V. “Do We Need Doctors Or Algorithms?”; 2012 [accessed 2020 May 23]. Available from: https://techcrunch.com/2012/01/10/doctors-or-algorithms/.

[8] Kandlikar S G, Garimella S, Li D, Colin S, King M R . Single-phase liquid flow in minichannels and microchannels. In: Heat Transfer and Fluid Flow in Minichannels and Microchannels. Oxford: Elvesier Science Ltd; 2006. p. 87–136.

[9] Gomez F A . The future of microfluidic point-of-care diagnostic devices. Bioanalysis. 2013;5(1):1–3.

[10] Hun P J , Lee P J, Sabounchi P , Lin R , Lee L P . Continuous perfusion microfluidic cell culture array for high-throughput cell-based assays. Biotechnology & Bioengineering. 2005;89(1):1–8.

[11] Chamarthy P , Garimella S V , Wereley S T . Measurement of the temperature non-uniformity in a microchannel heat sink using microscale laser-induced fluorescence. International Journal of Heat and Mass Transfer. 2010;53(15-16):3275–3283.

[12] Vogt J. Development of novel Particle Image Thermometry methods for highly resolved measurements of temperature and velocity fields in fluids; 2014. .

[13] Sakakibara J , Adrian R J . Whole field measurement of temperature in water using two-color laser induced fluorescence. Experiments in Fluids. 1999;26(1-2):7–15.

[14] Crimaldi J P , Koseff J R . High-resolution measurements of the spatial and temporal scalar structure of a turbulent plume. Experiments in Fluids. 2001;31(1):90–102.

[15] Gad-el-Hak M . The Fluid Mechanics of Microdevices—The Freeman Scholar Lecture. Fluids Engineering. 1999;121(1):5–33.

[16] Son B D , Lee J K, Yoon W Y. Effect of Tungsten Nanolayer Coating on Si Electrode in Lithium-ion Battery. Nanoscale Research Letters. 2018;13(1):2.

[17] Pfeiffer. “Introduction to vacuum technology, fundamentals, mean free path”; [accessed 2020 Aug 23]. Available from: https://www.pfeiffer-vacuum.com/en/know-how/introduction-to-vacuum-technology/fundamentals/mean-free-path/.

[18] Mattox D M . Introduction. In: Mattox D M .Handbook of Physical Vapor Deposition (PVD) Processing. 2nd ed. Oxford: Elvesier Science Ltd; 2010. p. 2–6.

[19] Adachi H , Wasa K. Thin Films and Nanomaterials. In: Wasa K, Kanno I, Kotera H. Handbook of Sputter Deposition Technology: Fundamentals and Applications for Functional Thin films,Nanomaterials, and MEMS. 2nd ed. Oxford: Elvesier Science Ltd; 2012. p. 14–28.

[20] Son H H , Seo G H , Jeong U , Shin D Y , Kim S J . Capillary wicking effect of a Cr-sputtered superhydrophilic surface on enhancement of pool boiling critical heat flux. International Journal of Heat and Mass Transfer. 2017;113:117.

[21] MIT. “Chemical Vapor Deposition”; [accessed 2020 Aug 23]. Available from: http://news.mit.edu/2015/explained-chemical-vapor-deposition-0619.

[22] Williams K R ,Gupta K , Wasilik M . Etch rates for micromachining processing-Part II. Journal of Microelectromechanical Systems. 2003;12(6):761 – 778.

[23] Nayak A P , Islam M S , Logeeswaran V J . Dry Etching. In: Bhushan B. Encyclopedia of Nanotechnology. Dordrecht: Springer Science Ltd; 2012. p. 587–589.

[24] Nayak A P , Islam M S , Logeeswaran V J . Wet Etching. In: Bhushan B. Encyclopedia of Nanotechnology. Dordrecht: Springer Science Ltd; 2012. p. 2829–2830.

[25] Silverio V , Freitas S C . Microfabrication Techniques for Microfluidic Devices. In: Rosales F J G. Complex Fluid-Flows in Microfluidics. 1st ed. Porto: Springer Science Ltd; 2018. p. 25–51.

[26] MicroChemicals. “LIFT-OFF”; [accessed 2020 Aug 12]. Available from: https://micro-chemicals.com/technical_information/lift_off_photoresist.pdf.

[27] Galib A . Graphene grown by chemical vapor deposition on evaporated copper thin films (master's thesis). Chalmers University of Technology. Gothenburg,2012;.

[28] Madou M , Wang C. Photolithography. In: Bhushan B. Encyclopedia of Nanotechnology. Dordrecht: Springer Science Ltd; 2012. p. 2051–2060.

[29] Do M T . Fabrication of submicrometer 3D structures by one-photon absorption direct laser writing and applications (dissertation). École normale supérieure de Cachan. Cachan,2015;p. 26.

[30] P Tabeling. Introduction to Microfluidics. New York: Oxford University Press; 2005.

[31] Elveflow. "Introduction to PDMS soft-lithography and polymer molding for microfluidics"; [accessed 2020 Jul 07]. Available from: https://www.elveflow.com/microfluidic-reviews/soft-lithography-microfabrication/introduction-about-soft-lithography-and-polymer-molding-for-microfluidic/.

[32] Bhattacharya S , Datta A , Berg J M , Gangopadhyay S . Studies on surface wettability of poly(dimethyl) siloxane (PDMS) and glass under oxygen-plasma treatment and correlation with bond strength. Microelectromechanical Systems. 2005;14:590–597.

[33] "Introduction of Soft Lithography"; [accessed 2020 Jul 24]. Available from: https://www.seas.upenn.edu/~nanosop/Intro_SoftLitho.htm.

[34] Arromba J . LED Induced Fluorescence using microscale visualization methods (master's thesis). Instituto Superior Técnico. Lisboa,2014;.

[35] Ross D Gaitan M Locascio L E . Temperature measurement in microfluidic systems using a temperature-dependent fluorescent dye. Analytical Chemistry. 2001;73(17):4117–4123.

[36] Vogt J . Development of novel Particle Image Thermometry methods for highly resolved measurements of temperature and velocity fields in fluids (dissertation). Darmstadt,2014;.

[37] Calado B , Semiao V . Characterization of the mixing regimes of Newtonian fluid flows in asymmetrical T-shaped micromixers. Experimental Thermal and Fluid Science. 2016;72:218–227.

[38] Rani S A SPS Pitts B. Rapid Diffusion of Fluorescent Tracers into Staphylococcus epidermidis Biofilms Visualized by Time Lapse Microscopy. Antimicrobial agents and chemotherapy. 2005;49(2):728–732.

[39] Guevara-Carrion G , Vrabec J , Hasse H . Prediction of self-diffusion coefficient and shear viscosity of water and its binary mixtures with methanol and ethanol by molecular simulation. The Journal of Chemical Physics. 2011;134(7).

[40] Bruus H . Analytical Navier-Stokes solutions. In: Bruus H. Theoretical microfluidics. Oxford: Oxford University Press; 2008. p. 19–42.

[41] D Bothe HW C Stemich. Fluid mixing in a T-shaped micro-mixer. Chemical Engineering Science. 2006;61:2950–2958.

[42] Abate A R , Lee D , Holtze C , Krummel A T , Do T, Weitz D A . Glass coating for PDMS microfluidic channels by sol–gel methods. Lab on a Chip. 2008;8(4):516–518.

[43] Glawdel T , Almutairi Z , Wang S , Ren C L . Photobleaching absorbed Rhodamine B to improve temperature measurements in PDMS microchannels. Lab on a Chip. 2009;9(1):171–174.

[44] Incropera F , Dewitt D P . Fundamentals of heat and mass transfer. 6th ed. New York: Wiley; 2006.

[45] Engineering ToolBox. ”Water - Enthalpy (H) and Entropy (S)”; 2009 [accessed 2020 Apr 13]. Available from: `https://www.engineeringtoolbox.com/water-properties-d_1508.html`.

Appendix A

Code of Project

A.1 *registerimages* function

```
registerImages function
function [MOVINGREG] = registerImages(MOVING,FIXED)
%  [MOVINGREG] = registerImages(MOVING,FIXED) Register grayscale images
%  MOVING and FIXED using auto-generated code from
the Registration
%  Estimator app. The values for all registration parameters were set
%  interactively in the app and result in the registered image stored in the
%  structure array MOVINGREG.

% Auto-generated by registrationEstimator app on 09-Dec-2019
%-----------------------------------------------------------


% Convert RGB images to grayscale
FIXED = rgb2gray(FIXED);
MOVING = rgb2gray(MOVING);

% Default spatial referencing objects
fixedRefObj = imref2d(size(FIXED));
movingRefObj = imref2d(size(MOVING));

% Intensity-based registration
[optimizer, metric] = imregconfig('monomodal');
optimizer.GradientMagnitudeTolerance = 1.00000e-04;
optimizer.MinimumStepLength = 1.00000e-05;
optimizer.MaximumStepLength = 6.25000e-02;
optimizer.MaximumIterations = 1000;
```

```
optimizer.RelaxationFactor = 0.500000;

% Align centers
fixedCenterXWorld = mean(fixedRefObj.XWorldLimits);
fixedCenterYWorld = mean(fixedRefObj.YWorldLimits);
movingCenterXWorld = mean(movingRefObj.XWorldLimits);
movingCenterYWorld = mean(movingRefObj.YWorldLimits);
translationX = fixedCenterXWorld - movingCenterXWorld;
translationY = fixedCenterYWorld - movingCenterYWorld;

% Coarse alignment
initTform = affine2d();
initTform.T(3,1:2) = [translationX, translationY];

% Apply transformation
tform = imregtform(MOVING,movingRefObj,FIXED,fixedRefObj,'translation',
optimizer,metric,'PyramidLevels',3,'InitialTransformation',initTform);
MOVINGREG.Transformation = tform;
MOVINGREG.RegisteredImage = imwarp(MOVING, movingRefObj, tform,
'OutputView', fixedRefObj, 'SmoothEdges', true);

% Store spatial referencing object
MOVINGREG.SpatialRefObj = fixedRefObj;
```

Appendix B

Influence of confluence angle and volumetric flow rate

B.1 Influence of confluence angle in transition zone length and location

B.1.1 $Q_{cold} = Q_{hot} = 50\mu L/min$

B.1.1.A 30° configuration

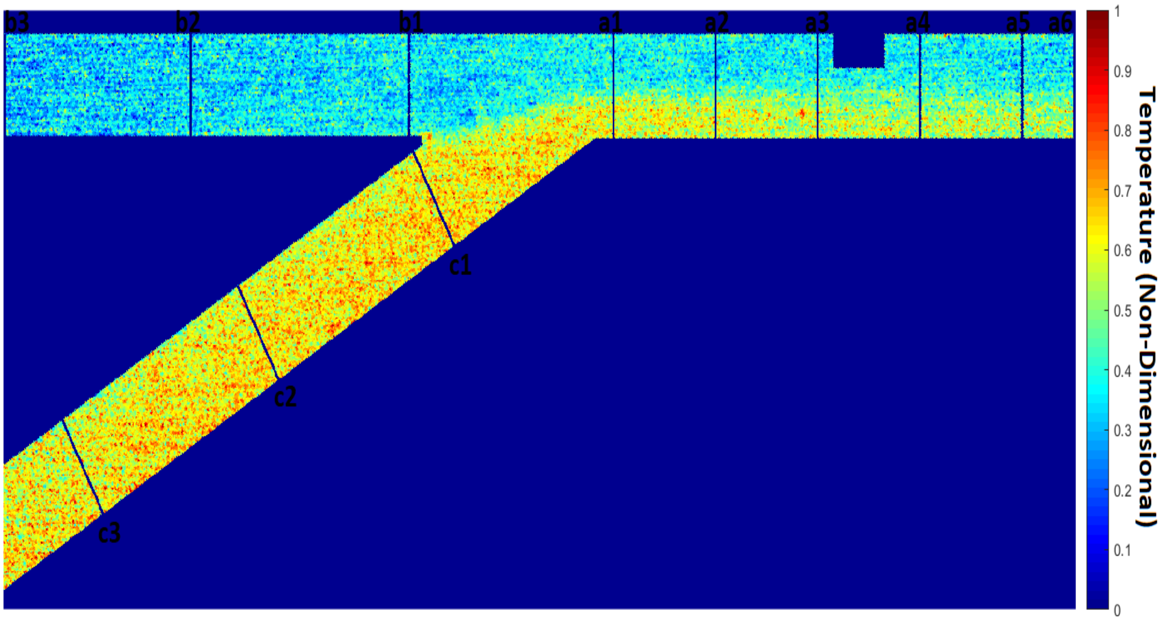

Figure B.1: 30° microchannel for $Q_{cold} = 50\mu L/min$

B.1.1.B 60° configuration

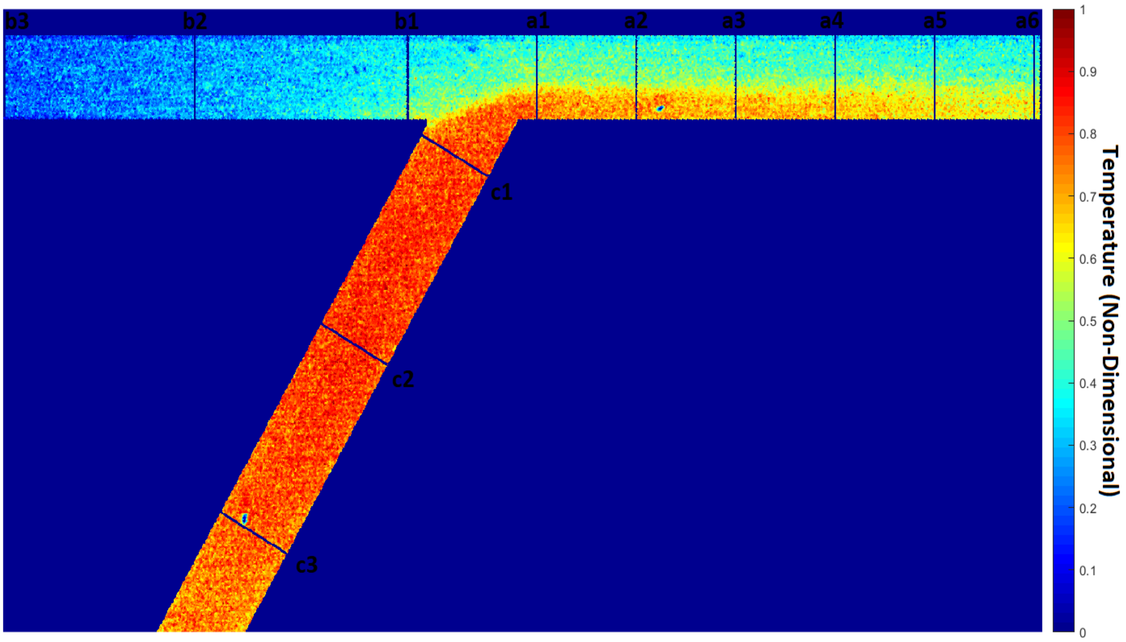

Figure B.2: 60° microchannel for $Q_{cold} = 50\mu L/min$

B.1.1.C 135° configuration

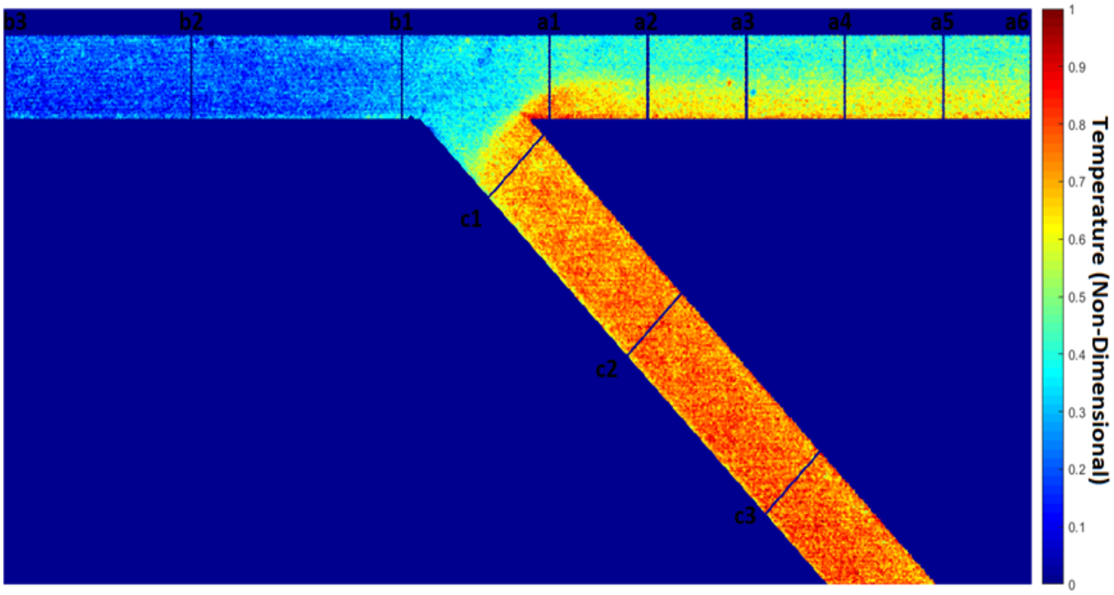

Figure B.3: 135° microchannel for $Q_{cold} = 50\mu L/min$

B.2 Influence of volumetric flow rate on transition zone length and location

B.2.1 30° configuration

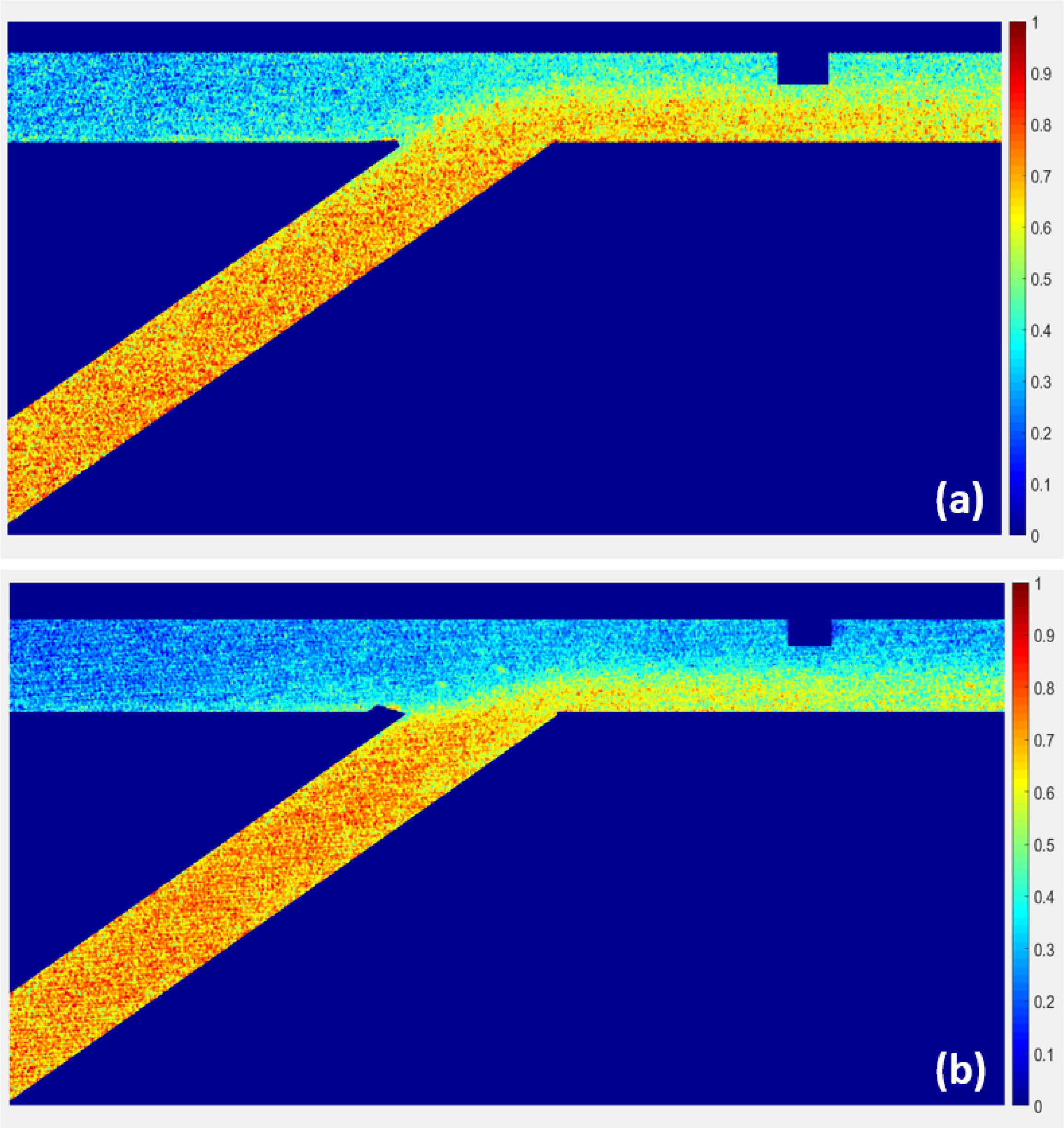

Figure B.4: 30° microchannel for (a) $Q_{cold} = 25\mu L/min$ (b) $Q_{cold} = 75\mu L/min$

B.2.2 60° configuration

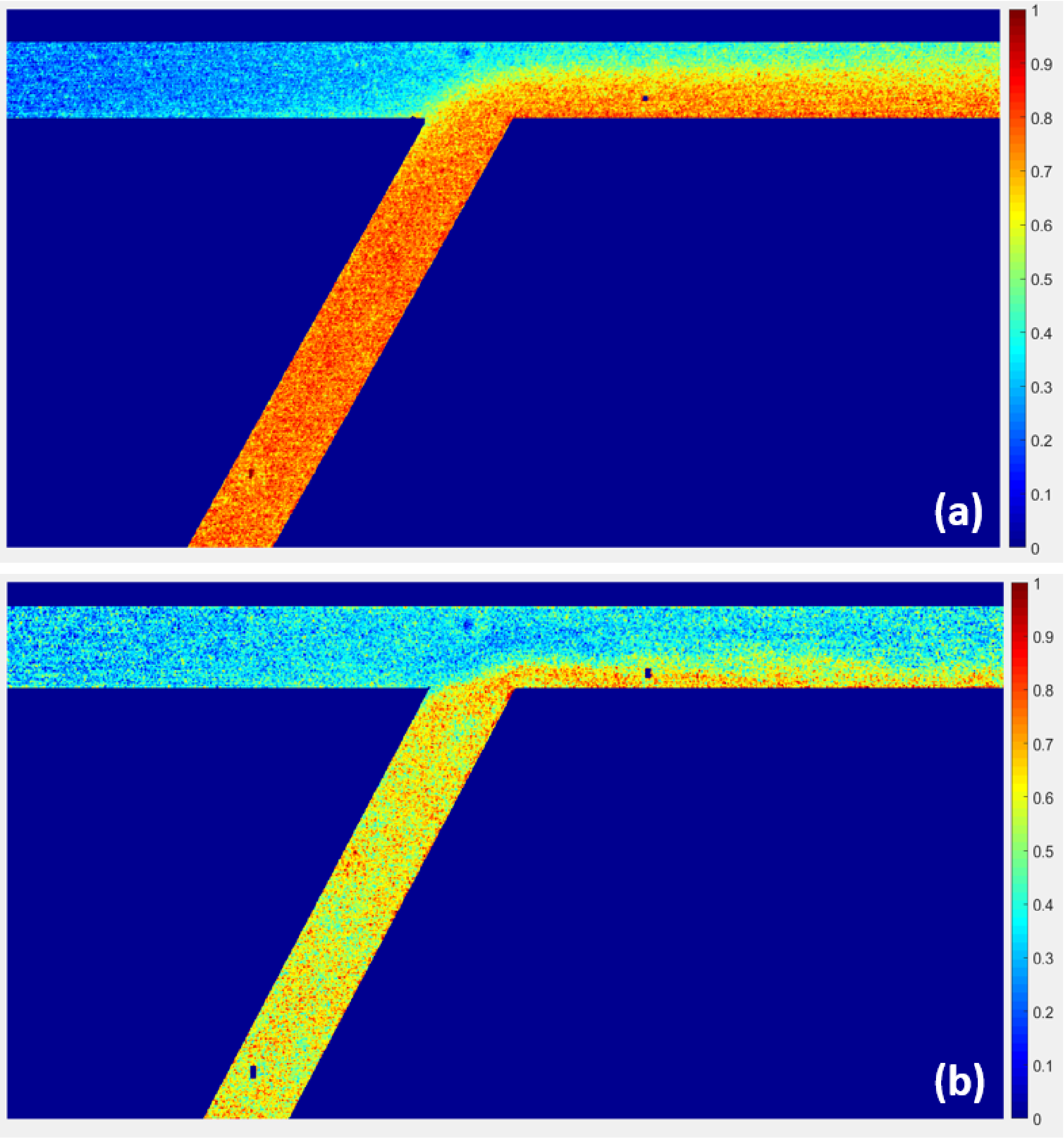

Figure B.5: 60° microchannel for (a) $Q_{cold} = 25\mu L/min$ (b) $Q_{cold} = 75\mu L/min$

B.2.3 90° configuration

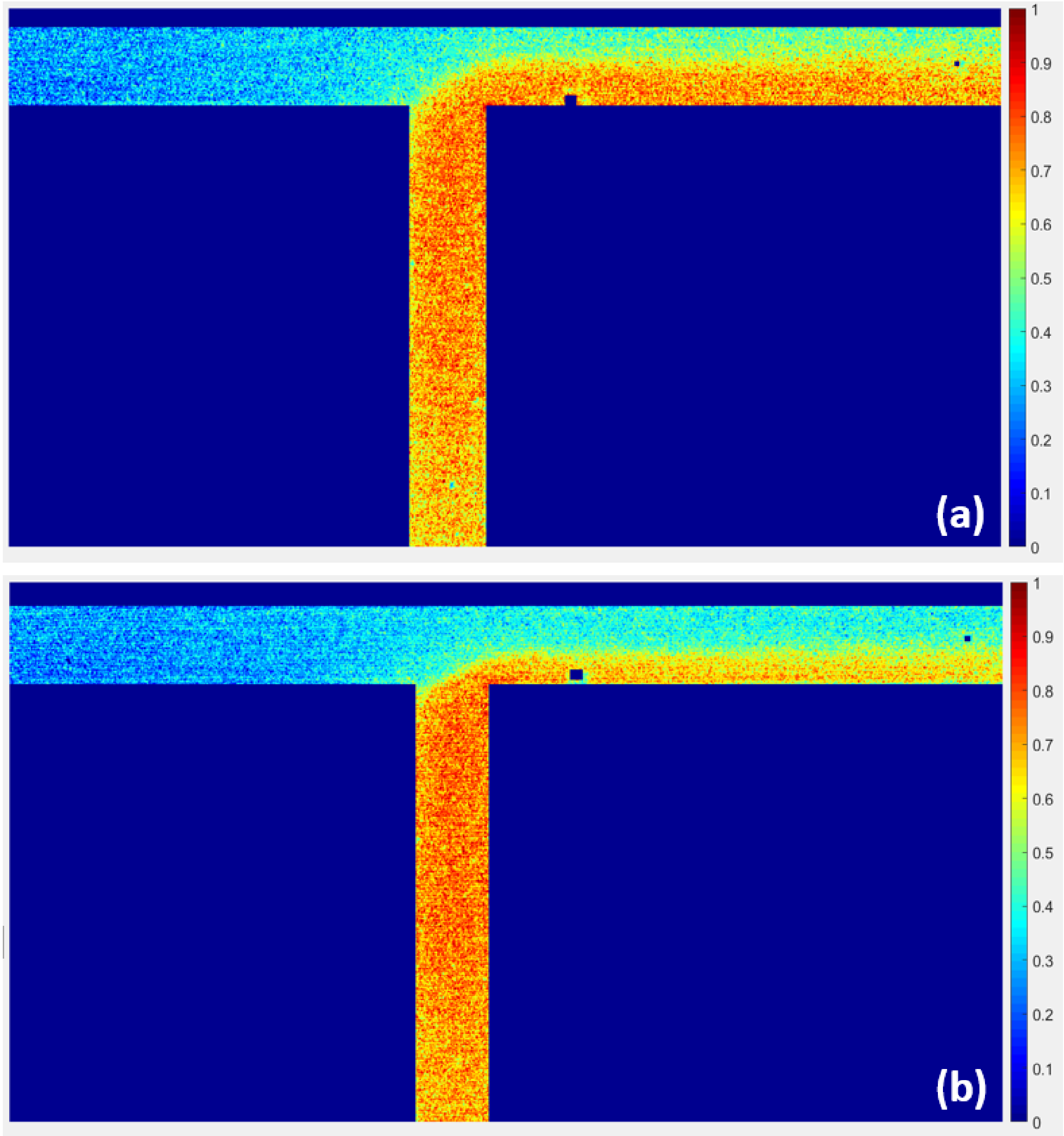

Figure B.6: 90° microchannel for (a) $Q_{cold} = 25\mu L/min$ (b) $Q_{cold} = 75\mu L/min$

B.2.4 135° configuration

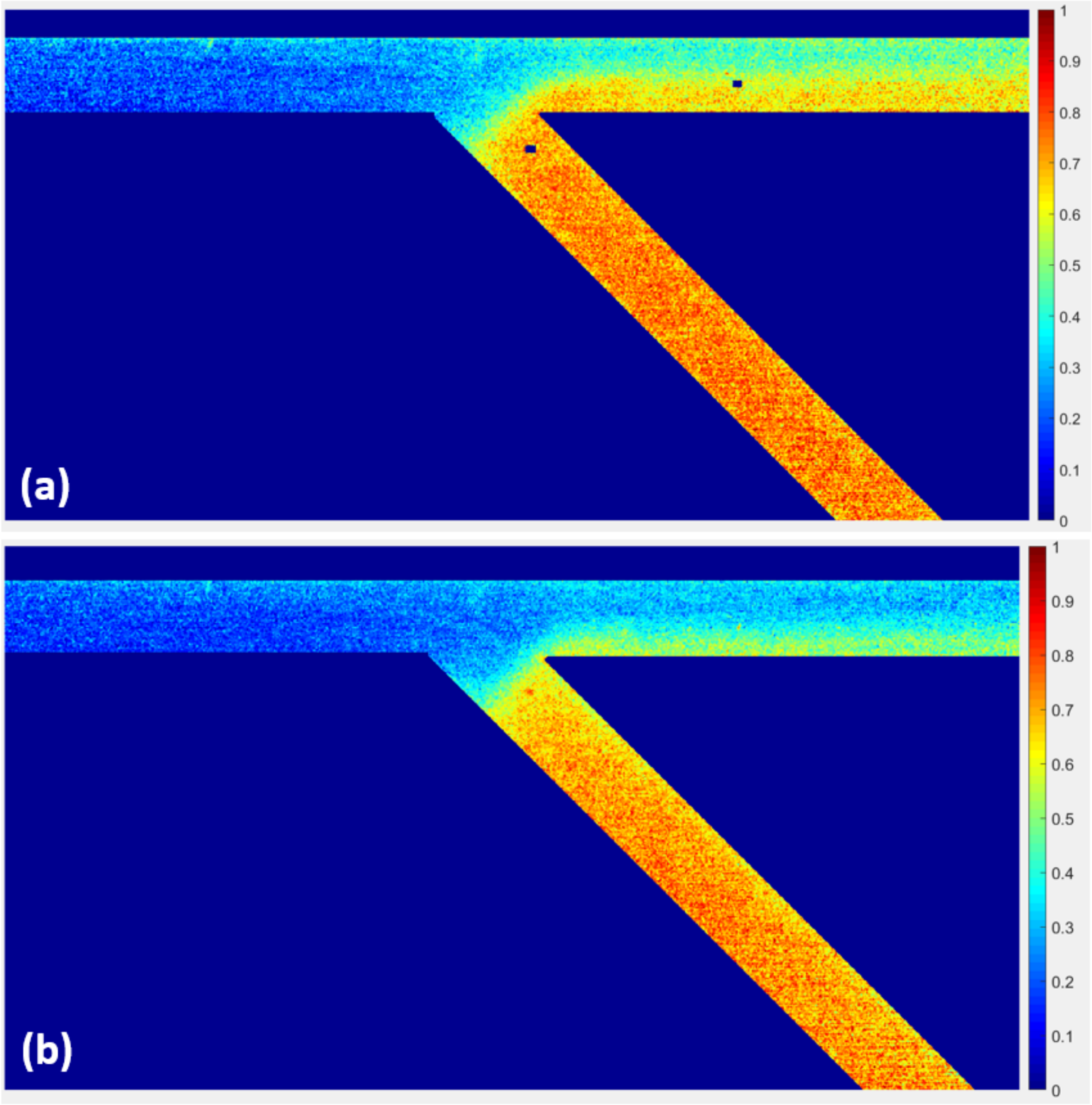

Figure B.7: 135° microchannel for (a) $Q_{cold} = 25\mu L/min$ (b) $Q_{cold} = 75\mu L/min$